UNIVERSITY OF SOUTHAMPTON

FACULTY OF PHYSICAL SCIENCES AND ENGINEERING

Optoelectronics Research Centre

Light Emission from Electron-Beam Driven Metasurfaces

by

Brendan P. Clarke

Thesis for the degree of Doctor of Philosophy

November 2018

UNIVERSITY OF SOUTHAMPTON

ABSTRACT

FACULTY OF PHYSICAL AND APPLIED SCIENCE

Optoelectronics Research Centre

Doctor of Philosophy

LIGHT EMISSION FROM ELECTRON-BEAM DRIVEN METASURFACES

by Brendan Paul Clarke

Over the last decade, free electron beams have been extensively used for characterization of nanostructures, particularly the study of plasmonic excitations using cathodo-luminescence and energy loss spectroscopy. A number of novel light sources based on electron-beam driven nano-antennas, -undulators and -gratings have also been demonstrated.

In this thesis I report on new approaches for controlling emission of light generated by electron beams interacting with nanostructured metasurfaces. In particular, I have developed the first holographic free-electron-driven light source in which emission induced by electrons injected into planar holographic pattern is controlled by the patterns design. On the platform of a conventional scanning electron microscope, using plasmonic, semiconductor and dielectric surface-relief holographic metasurface, for the first time I have experimentally demonstrated:

- Holographic patterns designed to generate highly-collimated radiation at a given wavelength in a prescribed direction. For example, a surface relief hologram only a few tens of square microns in size milled into a plasmonic gold film and driven by 30 keV electrons emits a light beam at 800 nm with divergence of only 2.5° with an efficiency $\sim 10^{-7}$ photons/electron. Continuous output beam steering over $\pm$ 10° in polar and azimuthal directions via nanoscale positional tuning of electron injection point has also been demonstrated.

- Holographic patterns designed to create a source of radiation with purposely structured complex wavefronts. I have demonstrated plasmonic patterns that upon electron excitation emit light beams with prescribed topological charge, up to 30.

- A direction-division multiplexed holographic free-electron-driven light source. The source comprises a microscopic array of plasmonic surface-relief holographic domains, each tailored to direct electron-induced light emission at a selected wavelength into a collimated beam in a prescribed direction. Emission direction is switched by μm-scale repositioning of the electron injection point among domains. I show that cross-talk between adjacent and overlapping domains can be as low as -3 dB at a only 2 μm injection point separation, thereby allowing for small arrays (typically $\sim$40 μm across) and rapid switching of the emission direction.

I also conducted computational studies of free-electron driven Smith-Purcell emission from composite gratings containing multiple slits per period, showing that the relative efficiency of resonant modes can be attenuated or enhanced with the addition and removal of narrow slits.

In summary, the nanoscale electron-driven light sources developed in this work offer an unprecedented level of control over the spectral characteristics, divergence, directionality and topological charge of emitted light. They may find application in lab-on-a-chip and sensor technologies, field-emission and surface-conduction electron-emission display technologies, optical signal multiplexing, and charged-particle-beam position metrology.

Contents

Abstract iii

Table of Contents iv

List of Figures vii

Declaration ix

Acknowledgements xi

1 Introduction 1
- 1.1 Motivation . . . 1
- 1.2 Cathodoluminescence and Electron Impact Excitations . . . 2
- 1.3 EIRE Analysis Techniques . . . 5
- 1.4 EIRE Light-Directing Structures . . . 10
  - 1.4.1 Electron Impact Structures . . . 10
- 1.5 Controlling Light with Metasurfaces . . . 16
- 1.6 Experimental Apparatus . . . 21
  - 1.6.1 Scanning Electron Microscope Platform . . . 21
  - 1.6.2 Angle-Resolved Cathodoluminescence Setup . . . 22
  - 1.6.3 Polar Transform . . . 24
  - 1.6.4 SEM External Scanning Controller . . . 26
- 1.7 Thesis Overview . . . 27

2 Holographic Free Electron Light Source 29
- 2.1 Introduction . . . 29
- 2.2 Structure Design and Fabrication . . . 31
- 2.3 Experimental Results . . . 36
- 2.4 Conclusion . . . 43

3 Direction-Division Multiplexed Holographic Free-Electron-Driven Light Sources 45
- 3.1 Introduction . . . 45
- 3.2 On-Demand Directional Control of EIRE . . . 47
  - 3.2.1 Beam-Steering Devices . . . 48
  - 3.2.2 Directionally-Switchable Free-Electron Light Source: First Prototypes . . . 52
  - 3.2.3 Cross-Talk Analysis . . . 57
  - 3.2.4 Continuous Beam-Steering With Single Holographic Source . . . 61

3.2.5 Switchable Multi-Element Light Source . . . 63
3.3 Conclusion . . . 65

4 All-Dielectric Free-Electron-Driven Holographic Light Sources 67
4.1 Introduction . . . 67
4.2 Holographic Control of EIRE From Semiconductors and Dielectrics . . . 68
4.2.1 Semiconductor and Dielectric Structured Light Sources . . . 70
4.2.2 Design and Fabrication . . . 73
4.2.3 Semiconductor and Dielectric Holographic Source Characterization 77
4.3 Conclusion . . . 79

5 Smith-Purcell Radiation from Compound Blazed Gratings 81
5.1 Introduction . . . 81
5.2 Electron Near-Field Emission Coupling . . . 82
5.2.1 Electron Relativity and Emissions . . . 82
5.2.2 The Smith-Purcell Effect and Enhancement . . . 84
5.3 Compound Smith-Purcell Enhancement Gratings . . . 88
5.3.1 Structure and Modelling . . . 90
5.3.2 Results . . . 91
5.4 Conclusion . . . 95

6 Conclusions 97
6.1 Summary . . . 97
6.2 Outlook . . . 98

A Publications 101

Bibliography 103

List of Figures

1.1 Representation of TR in polarisable substrate. . . . 2
1.2 Schematic of SPP excitation by electron injection. . . . 3
1.3 Propagation distance of SPP in Au determined by electron beam excitation. 4
1.4 Hyperspectral imaging of plasmonic grating. . . . 6
1.5 Three arrangements of EELS within a TEM system. . . . 7
1.6 EELS map of nano-decahedron. . . . 8
1.7 Schematic overview of CL polarimetry. . . . 9
1.8 Leaky SPP geometry resulting in supercontinuum emissions. . . . 11
1.9 Spatial control of polar CL pattern. . . . 12
1.10 Electron beam driven antenna designs. . . . 14
1.11 Example of confined output light from collective-mode EIRE metameterial. 15
1.12 Examples of nanostructure array metasurfaces. . . . 17
1.13 Examples of nanostructured metasurfaces designed for specific wavelengths. 18
1.14 Examples of metasurface holograms. . . . 20
1.15 Scanning Electron Microscope Setup 21
1.16 Optical cathodoluminescent imaging setup. . . . 23
1.17 Illustration of mapping between sample space in cylindrical coordinates to CCD. . . . 24
1.18 Polar, azimuthal, and solid angle of each pixel on CCD detector used. . . 25
1.19 External scan control setup for SEM. . . . 26

2.1 Proportion of SPP excitation for bulk Au under 30kV electron beam. . . . 31
2.2 Holographic free-electron light source design. . . . 32
2.3 Normal electric field component on Au surface simulated for design hologram wavelengths. . . . 33
2.4 Intensity of focused spot around optimal sample depth 34
2.5 Composite SEM image of samples used for optimizing milling depth . . . 34
2.6 De-lamination of hologram samples initially fabricated on SiN membrane. 35
2.7 Angle-resolved spectroscopy of the electron-induced light emission 37
2.8 Angular dispersion performance of gold surface holographic light sources. 38
2.9 Beam divergence performance of gold surface holographic light sources. . 39
2.10 Generation of optical vortex beams. . . . 41
2.11 Results of higher topological-charge design holographic samples. . . . 42

3.1 Artistic impression of multiplexed array of free-electron holographic light sources 47
3.2 Overview of DMD spatial light modulator structure. . . . 49

3.3 Implementations of nanomechanical metamaterials for random-access spatial light modulation. . . . 50
3.4 Examples of metamaterial-embedded liquid crystal spatial light modulators. 51
3.5 First prototype of directionally-selective holographic pixel. . . . 53
3.6 Second prototype of directionally-selective holographic pixel. . . . 55
3.7 Prototype of bi-directional samples to quantify holographic element crosstalk. 56
3.8 Relative magnitude of parasitic emission from a secondary holographic source for othogonal azimuthal oriented elements. . . . 59
3.9 Relative magnitude of parasitic emission from a secondary holographic source for opposite azimuthal oriented elements. . . . 60
3.10 Steering the output beam of a single holographic source. . . . 62
3.11 Azimuthally multiplexed hologram emitter pixel and characteristics. . . . 64

4.1 Schematic representations of surface excitation modes in CL. . . . 69
4.2 Examples of dielectric and chalcogenide metasurface applications. . . . 72
4.3 Properties of materials used for TR-controlling holographically designed emitters. . . . 74
4.4 Holographic milling patterns for dielectric and semiconductor materials compared to reference Au design. . . . 75
4.5 SEM images of hologram samples for all materials and design wavelengths. 76
4.6 Schematic representation and result of Au surface for comparison with dielectrics. . . . 77
4.7 Angular distribution of electron-beam-induced light emission from dielectric and chalcogenide holographic surface-relief structures. . . . 78
4.8 Total light emitted by hologram sample vs. relative brightness of spot for each fabrication material and design wavelength. . . . 80

5.1 Schematic representations of Cherenkov radiation. . . . 83
5.2 Smith-Purcell emission arrangement and geometric parameters governing emission from the grating. . . . 85
5.3 Angle of maximum emission and scaled brightness for equations 5.8 and 5.7. . . . 86
5.4 Applications of SP-type grating structures. . . . 88
5.5 Compound optical grating higher-order reflection response. . . . 89
5.6 Compound grating Smith Purcell light sources. . . . 91
5.7 Compound Smith-Purcell grating efficiency. . . . 92
5.8 SP emission from compound gratings. . . . 94
5.9 Compound gratings effective fill factor compared with single grating. . . . 95

DECLARATION OF AUTHORSHIP

I, Brendan Paul Clarke, declare that the thesis entitled "Light Emission from Electron-Beam Driven Metasurfaces" and the work presented in the thesis are both my own, and have been generated by me as the result of my own original research. I confirm that:

- this work was done wholly or mainly while in candidature for a research degree at this University;
- where any part of this thesis has previously been submitted for a degree or any other qualification at this University or any other institution, this has been clearly stated;
- where I have consulted the published work of others, this is always clearly attributed;
- where I have quoted from the work of others, the source is always given. With the exception of such quotations, this thesis is entirely my own work;
- I have acknowledged all main sources of help;
- where the thesis is based on work done by myself jointly with others, I have made clear exactly what was done by others and what I have contributed myself;
- parts of this work have been published as the journal papers and conference contributions listed in Appendix A Publications.

Signed: _____

Date: _____

Acknowledgements

The work presented here in this report would be impossible without the constant help and support of my supervisors, collaborators, and friends at fellow group members of the Optoelectronics Research Centre. In particular I would like to thank:

- Nikolay Zheludev and Kevin MacDonald, my supervisors, for their invaluable guidance, insight, and patience throughout my research.
- My fellow team members, without whom this work would not have been possible. In particular, Jinkyu So for my training and initial introduction into electron beam science and modelling, and FIB fabrication.
- The staff and members of the ORC and Nanophotonics group, in particular Neil Sessions for training in the use of the ORC cleanroom facilities.
- My partner Lenka, whose encouragement and support has never waned, regardless of the circumstances.

Chapter 1

Introduction

1.1 Motivation

This work aims to demonstrate that metasurface structures are uniquely advantageous in shaping light output derived from highly localised free-electron excitations, opening new possibilities for the applications of nanoscale devices.

Metamaterials, structures composed of sub-wavelength unit cells called meta-molecules that control the overall electromagnetic properties via geometrically-defined resonances, have demonstrated broad applicability in realizing novel optical phenomena such as negative refractive index [1]; slow light [2, 3]; superfocusing [4]; and reflection, transmission, and absorption properties not achievable with natural media. In addition these structures have proven amenable to being structurally reconfigured with various forces at the nanoscale, expanding the possibility of single devices with a range of adaptable inputs and outputs. Metamaterial optical modulators have been demonstrated which rely on a range of forces including electrostatic, thermal, and photonic inputs [5].

Conventional metamaterials are designed to operate under free space light - typically a plane wave front - to manipulate the transmission, reflection, and absorption properties of the material or indeed, to modify the wavefront characteristics of emitted light. However, these structures may also be designed to couple to localised excitations such as a quantum dot, nitrogen-vacancy centre of a crystal lattice, or direct injection from a scanning near-field optical microscopy (SNOM) tip. An electron beam, whether from an electron microscope or compact emitting device, also provides an agile source for injection of such localised excitation into a structured nanoscale landscape for the purpose of designing light output. Here, we use a scanning electron microscope (SEM) as a test platform in experimentally confirming the applicability of such metasurface light sources.

This chapter constitutes an overview of techniques relevant to the electron-beam interrogation of metasurface structures, a short overview of the state-of-the-art in electron-beam driven nanostructures, and a description of the experimental apparatus employed in the subsequent chapters.

1.2 Cathodoluminescence and Electron Impact Excitations

There are a number of discernable physical processes that occur when an electron crosses an interface between two materials with different electrostatic properties, the radiative results of which are collectively referred to as the cathodoluminescent (CL) emissions. Any injection of a free electron from vacuum into a material will result in some amount of transition radiation (TR), based on the dielectric constant of the material in question as the electron initially loses energy at the interface. In addition, where the velocity of the electron exceeds the local phase velocity of light in the material, the particle will continue to lose energy and emit Cherenkov radiation as it propagates. While optical radiation from both depend on a charged particle travelling at relativistic velocities, TR is distinct in that it only occurs at the material boundary.

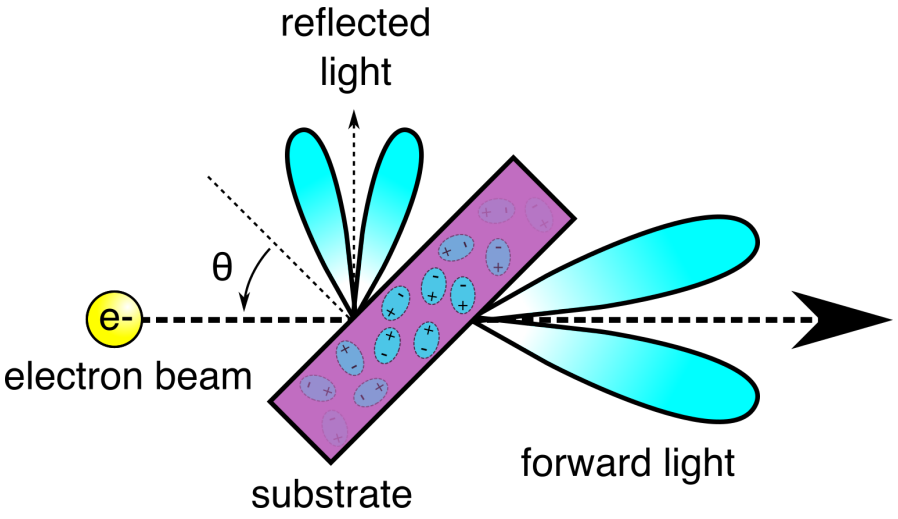

FIGURE 1.1: Representation of transition radiation (TR) in a polarisable substrate. When optical TR occurs, the majority is emitted at an acute angle to the particle propagation, with a smaller portion reflected by the material.

In early studies of free electron-optical interaction, TR was extensively studied after being first theorized in 1946 by Ginzburg and Frank [6]. The effect, in short, occurs when a charged particle such as an electron, impacts a surface or moves across an interface between materials of different electric permittivity. The electron induces an opposing charge in the material as it approaches, and the two charges create an effective dipole. The dipole annihilation creates a release of energy in both farfield and evanescent waves and a proportional loss in velocity in the electon.

In general, transition radiation is largely emitted at an acute angle to the direction of particle propagation, with the peak emission angle dependent on the Lorentz factor of the particle. However, optical TR is also emitted in the reverse direction as it is reflected by the interface surface. Thus, a common method of accurately measuring beam velocity is by reflection of TR from an angled metal foil placed in the beam path, as shown in figure 1.1.

In addition to these coherent radiative processes, which can be described entirely by a set of Maxwell's equations for the interface, the moving charge will excite travelling surface plasmon polaritons (SPPs) on the surface of plasmonic metals, an evanescent but also coherent form of emission. These oscillations in the density of free electron carriers, coupled to transverse magnetic field as shown in the orientation of the field components in figure 1.2, propagate along the interface between a conductor and a dielectric medium or vacuum and are highly localized, responding strongly to subwavelength features below the scale of an optical wavelength.

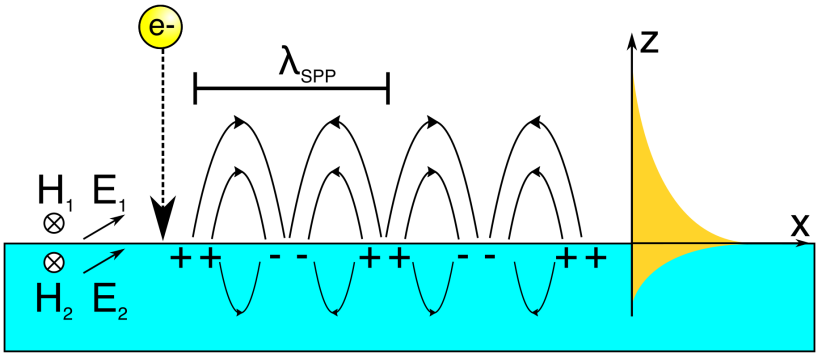

FIGURE 1.2: Schematic of SPP excitation by electron injection. The oscillation of free carriers leads to the field component orientations shown, with magnetic field always the exclusively transverse component. The resulting evanescent field magnitude decays away from the interface exponentially.

SPPs are traditionally excited optically, with a grating or prism providing the additional momentum required to match wave vector of free-space radiation at the metal interface. However, these techniques, or others involving surface or waveguide discontinuities, are inflexible and do not easily allow for easy repositioning or miniaturization of the SPP source. It has been shown that with the effective dipole annihiliation of an electron beam impacting a plasmonic metal, the component of the electron scattering vector parallel to the surface forms a surface plasmon polaritron with λ_{SPP} given by the plasmonic properties of the material. This is frequently used as an effective and flexible source of SPPs. The propagation distance is also easily measured by focusing the electron beam close to an out-coupling grating as shown in figure 1.3 [7–9].

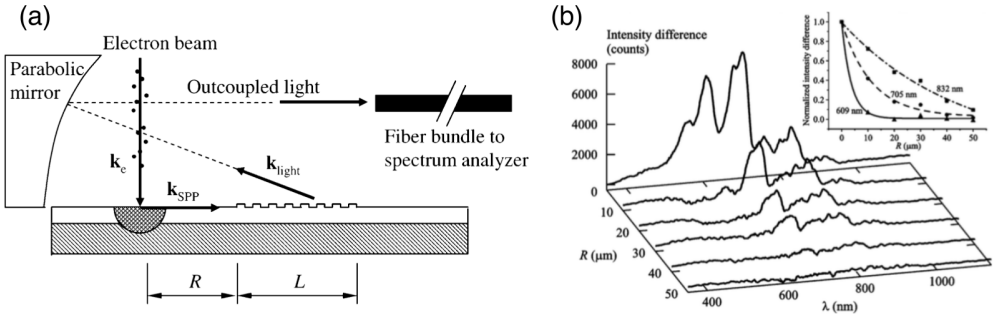

FIGURE 1.3: (a) Schematic of the experimental setup for excitation of surface plasmon polaritons (SPPs) with wave vector k_{SPP} by direct injection of a beam of free electrons of wave vector k_e, and their decoupling as light by a grating. (b) Decay of the SPPs as function of distance R between the grating edge and electron injection point. Inset shows normalized intensities of the decoupled SPP signal at different peak wavelengths as function of R. From [7].

While this comprises the coherent excitations that occur in an electron injection process, in many materials, such as semiconductors and dielectrics, a significant proportion of the CL emission is derived from incoherent processes arising from inelastic scattering of the electron within the material. The bulk of this work however concerns coherent processes only, therefore a treatment of incoherent emission is given where necessary. Collectively, all propagating electromagnetic waves from a material under electron-beam injection is termed electron-induced radiative emission (EIRE), the study of which is largely concerned with characterizing the materials and structures that can be probed with electron beams. In this work, I will apply the tools of EIRE sample characterization to controlling the light released from driving nanostructured sources with an electron beam.

1.3 EIRE Analysis Techniques

A number of techniques have emerged to use the excitations outlined in the previous section as a means of analysing the structural and compositional features of materials and devices. Cathodoluminescence, the general study of light emitted from electron-impacted structures, has been supplemented with hyperspectral imaging of a 2D region of a surface. By identifying gradients in the spectral components of such a scan, features such as changes in composition or structural resonance can be identified. Complimentary to this, the velocity differential of electrons entering and exiting the structure can be studied to reveal resonances and band transitions in a material. More recently, angle-resolved cathodoluminescence has emerged as a tool through which the complete wavefront of light emissions - wavelength, direction, and phase profile - from a point on a sample may be characterized.

As a conventional image would contain a composite of red, green, and blue channels defined over a 2D region, a hyperspectral image (HSI) records an entire spectrum - an arbitrarily large vector of amplitudes for a range of wavelengths - for each coordinate. The concept is well-known in fields such as environmental research [10] and medical imaging [11]. In the case of electron-beam interrogated materials, the HSI technique generates a three-dimensional data cube with two spatial axes in the sample plane and a spectral axis. The data in this set can then be used to interpret, for example, single-wavelength spatial intensity distributions, which can subsequently be used to interpret geometric features or, such features being given, decay length of SPPs generated by electron injection as shown in the wavelength cross-sections in figure 1.4.

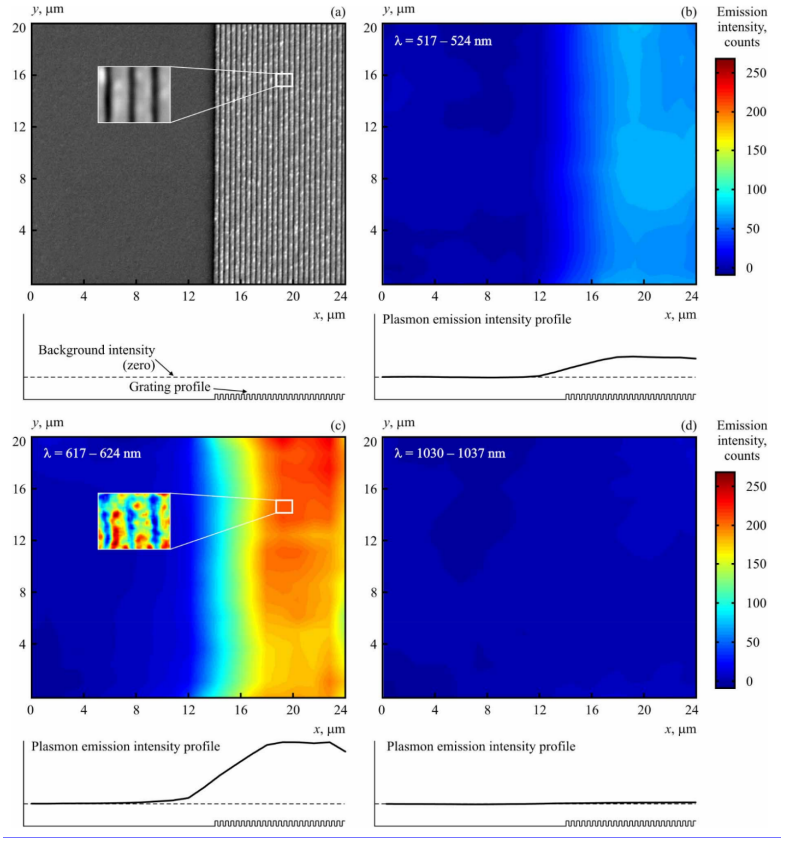

FIGURE 1.4: Hyperspectral imaging of the 400 nm gold grating sample. (a) Secondary electron image of hyperspectral area for which cross sections of wavelength range are shown in (b, c and d). (b) 517-524 nm, where the grating is weakly resonant and plasmon decoupling efficiency is relatively poor; (c) 617-625 nm, where the grating is resonant; (d) 1030-1037 nm, where emission is negligible. Insets, (a) and (c) show SEM and cathodoluminescent detail, respectively. From [12].

Electron energy loss spectroscopy (EELS) employs an electron beam with a very narrow range of kinetic energy as a probe for the purposes of determining the various energy level transitions in a sample. By analysing the resulting kinetic energies of scattered electrons, typically by observing changes in deflection of the resulting beam as it travels through a magnetic prism [13], the precise inelastic losses possible in the material are revealed. In combination with other analytic methods, these losses can be interpreted as phonon and plasmon exitations, band transitions, ionization occurances, and Cherenkov radiation arising from the properties of the material.

Because the resolution of the probe does not depend on optical limitations, features smaller than 1 nm can be distinguished with this method [14], and where a monochromatic electron source is used, an energy resolution of 0.1 eV can be achieved [15].

The method is generally compatible with other methods of electron-beam analysis and is therefore frequently combined with transmission electron microscopy systems (TEM), energy-dispersive x-ray spectroscopy (EDX), scanning-transmission electron microscopy

(STEM), or other measurement systems as shown in figure 1.5 [16]. As such, EELS has become a common tool used for analysing the properties, including local density of states (LDOS) of individual [17–19] and chained [20–22] nanoparticles and metamaterials [23, 24], an example of which is shown in figure 1.6.

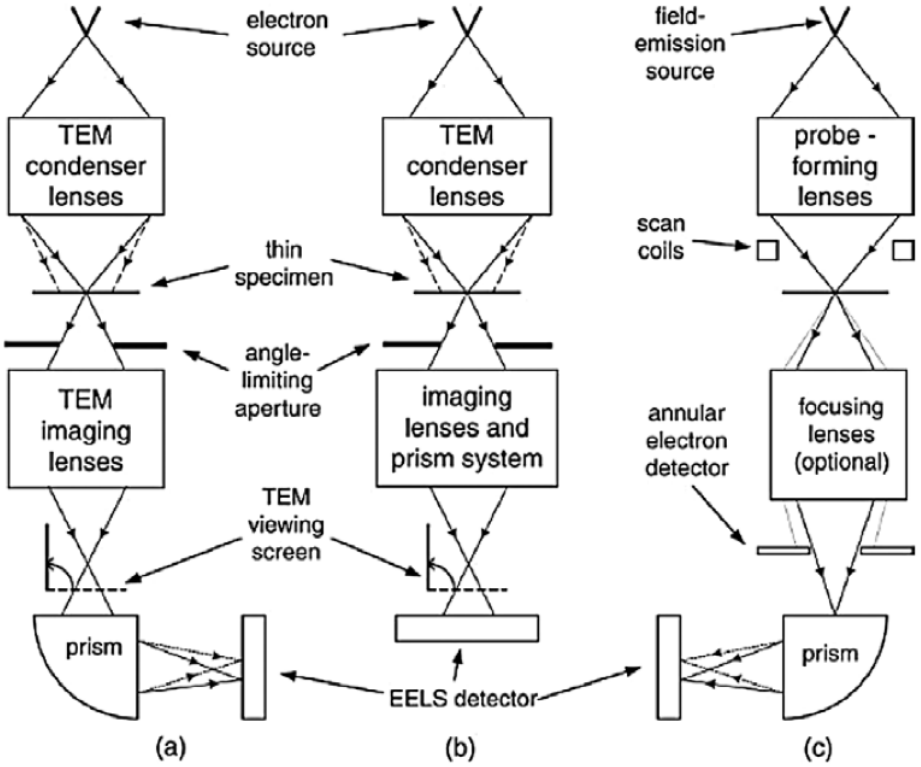

FIGURE 1.5: Three arrangements for measuring EELS within a TEM system: (a) magnetic prism and detector attached to existing TEM system, (b) TEM system with prism incorporated into beam column, and (c) prism and detector added on to existing scanning-transmission (STEM) system. From [13].

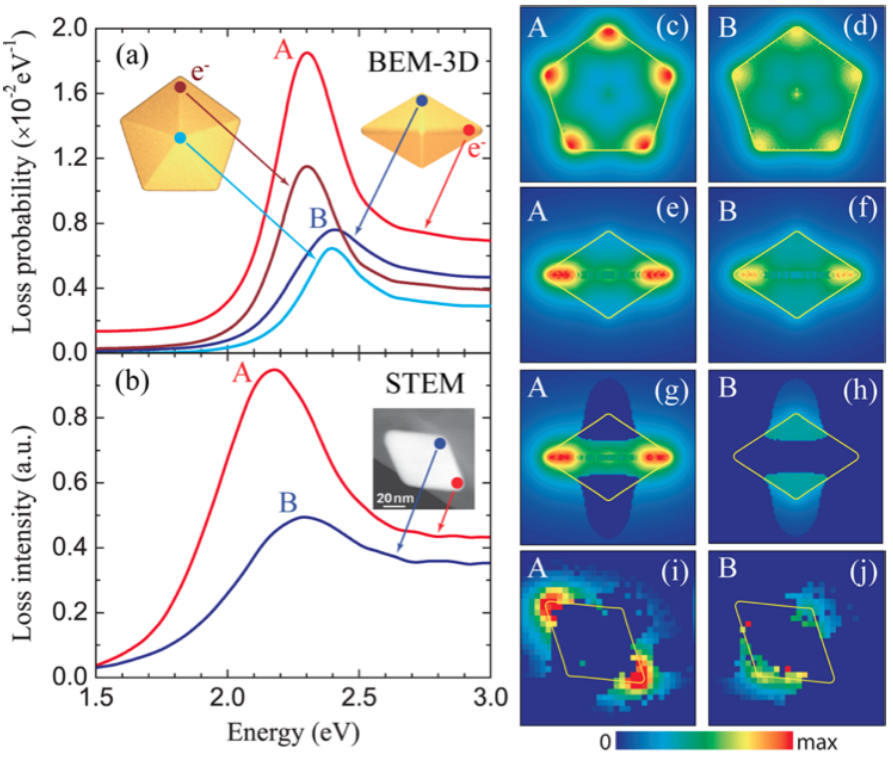

FIGURE 1.6: Electron energy-loss spectroscopy analysis of an individual gold decahedron. (a) Calculated EELS spectra for electron beam of energy 100 keV (positions given in insets) showing excitation of azimuthal (A) and polar (B) plasmon modes. (b) Experimental STEM-EELS spectra for 2 corresponding electron beam positions and their azimuthal and polar modes. (c-h) Calculated EELS probability maps of the azimuthal (left column) and polar (right column) modes as a function of electron probe position. (i, j) Corresponding experimental EELS intensity maps with each pixel associated with a different position of the electron beam. The decahedron side length is 58 nm in all cases. From [17].

While the CL methods described above focus on the spectral content and spatial distribution of emissions from a sample, the vectorial nature of light can inform a greater level of information about the emitting structure. By analysing the angular profile of light emissions for example, the local orientation of emission centres in single [25, 26] or multiple [27, 28] nanoscale structures can be determined. The light is usually collected via a reflector arrangement described in section 1.6. Recently, angle-resolved CL analysis has been demonstrated combined with polarimetry, allowing the full Stokes parameters to be accessed, illustrated in figure 1.7. This allows, for example, local anisotropies in the sample to be determined [29].

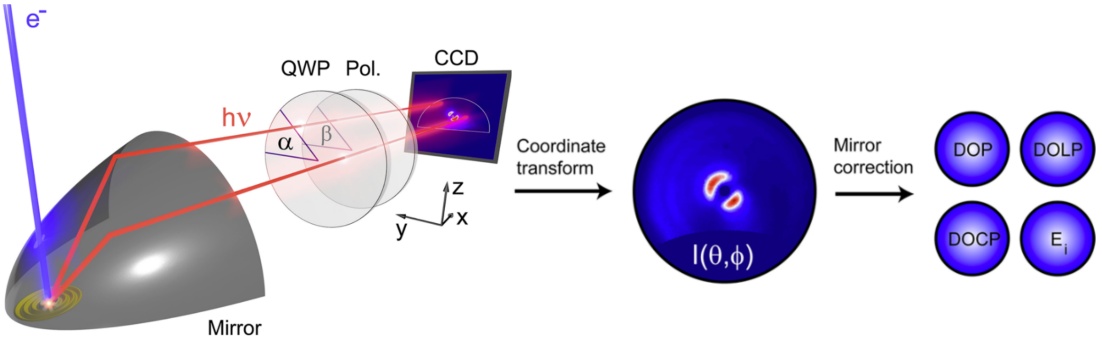

FIGURE 1.7: Schematic overview of cathodoluminescence polarimetry setup. Light emission is collected by a parabolic mirror and directed toward a polarimeter composed of a quarter wave plate and linear polarizer set at angles α and β, respectively. Six measurements with different settings of the polarimeter are required to retrieve the full angle-resolved polarization state of the collected light. Using the retrieved Stokes parameters it is possible to determine any figure of merit for polarization including the total, linear, and circular degrees of polarization, as well as the electric field components. From [29].

These combined methods allow a wealth of information to be derived from a sample about the position, orientation, and relative strength of many types of electromagnetic resonances. The utility of electron beams coupled to optical modes of nanostructures continues to provide novel applications such as high resolution 3D tomogaphy [30], identification of nanoparticle-bonded functional groups [17], and the generation of electron vortex beams with metasurface structures [31].

1.4 EIRE Light-Directing Structures

1.4.1 Electron Impact Structures

The utility of a ballistic electron source as a highly localised, broadband excitation of SPPs has led to a wealth of research in materials and structures best suited to controlling light from this injection. Given an electron of sufficient velocity, the properties of the light emitted depend primarily on the material and structure, thus several types of materials and structures have proven useful as electron-beam-driven light sources: thin-film and layered structures; arrangements of nanoparticles that behave as emitting antennas, and metamaterials, continuous arrays of surface geometries in which each repeating element acts collectively to control the output.

In layered structures for example it has been shown that the probability of SPP excitation can be increased by using dielectric thin films, with a yield up to 1 per 100 electrons [32]. In addition to enhancing plasmon response, other functions of electron beam driven SPPs have been developed, such as dielectric-supported thin plasmonic metal films and metal-dielectric multilayer systems which show 'leaky' degenerate plasmons that lose energy as they travel, and can create efficient, electron-driven super-continuum sources as shown in figure 1.8 [32].

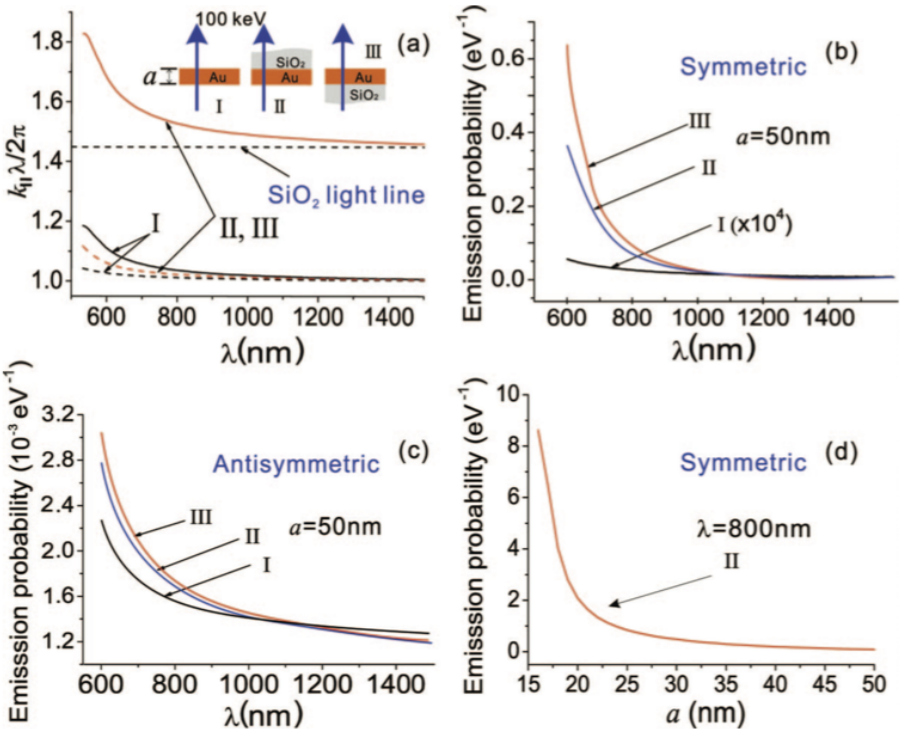

FIGURE 1.8: Supercontinuum plasmon generation in supported gold films of thickness $a = 50$nm. (a) Dispersion relation of plasmons in symmetric (induced charge) and antisymmetric plasmon modes represented by dashed and solid curves respectively. (b, c) Probability of coupling to symmetric (b) and antisymmetric (c) modes in these structures. (d) Probability of exciting symmetric plasmon modes corresponding to free space wavelength ($\lambda = 800$nm) in structure II as a function of metal thickness. From [32].

In addition, certain novel layered materials have been shown to have enhanced response to electron-beam excitation. Plasmon generation in graphene offers higher degree of plasmonic spatial confinement and multiple highly-confined propagating plasmons have been generated from only a single grazing-incident electron [33]. In doped graphene layers, this leads to increased interaction with nearby optical emitters such as quantum dots [34].

A traditional antenna, at its most basic, consists of a resonant metallic element and likewise, arrangements of metallic nanoparticles can be used as a receiving antenna for charged particles such as relativistic electrons. Such small-scale devices have received considerable attention as transmitters and receivers of light [35]. Single nanoparticles have, for example, demonstrated some control over directivity from light emitted when asymmetrically driven by electron-beam injection [25, 36]. However, for single nanoparticles, scattering efficiency is typically attenuated significantly with off-axis excitation, and the emission intensity profile remains directionally broad, as seen in figure 1.9. Appropriate antenna design somewhat mitigates this attenuation for singular structures.

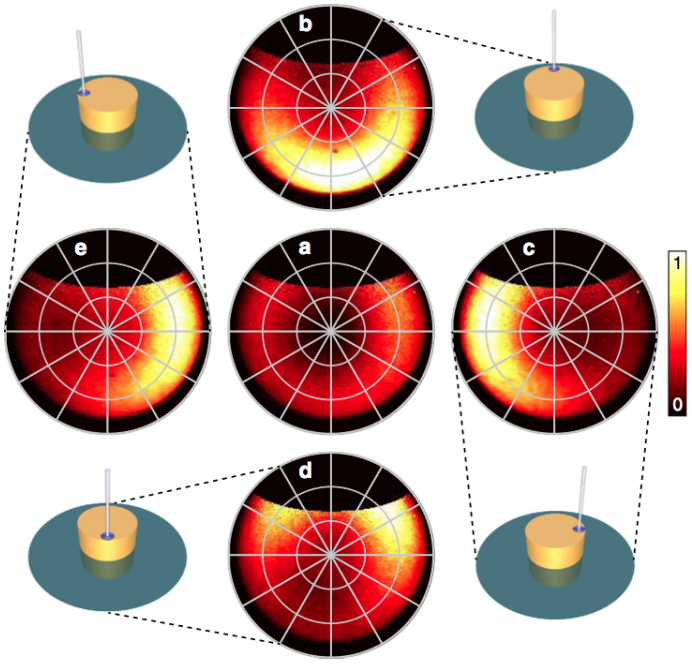

FIGURE 1.9: Normalized polar CL emission patterns collected from a 180 nm diameter nanodisk at 600 nm wavelength for excitation at the centre (a) and near the edge for four orthogonal azimuthal angles: 0° (b), 90° (c), 180° (d) and 270° (e). From [26].

A typical nano-antenna arrangement designed to emit a specific wavelength when driven by an electron beam is shown in figure 1.10(a). It has been shown that the emissions at the designed resonant wavelength from this dual-particle arrangement are stronger than from a single particle alone, when the electron beam is directed into the gap between them [37]. As with conventional antennas, the geometry can be manipulated in a number of ways to alter the output, such as providing some concentration of output angular distribution with the Yagi-Uda design as shown in figure 1.10(e-k) [26].

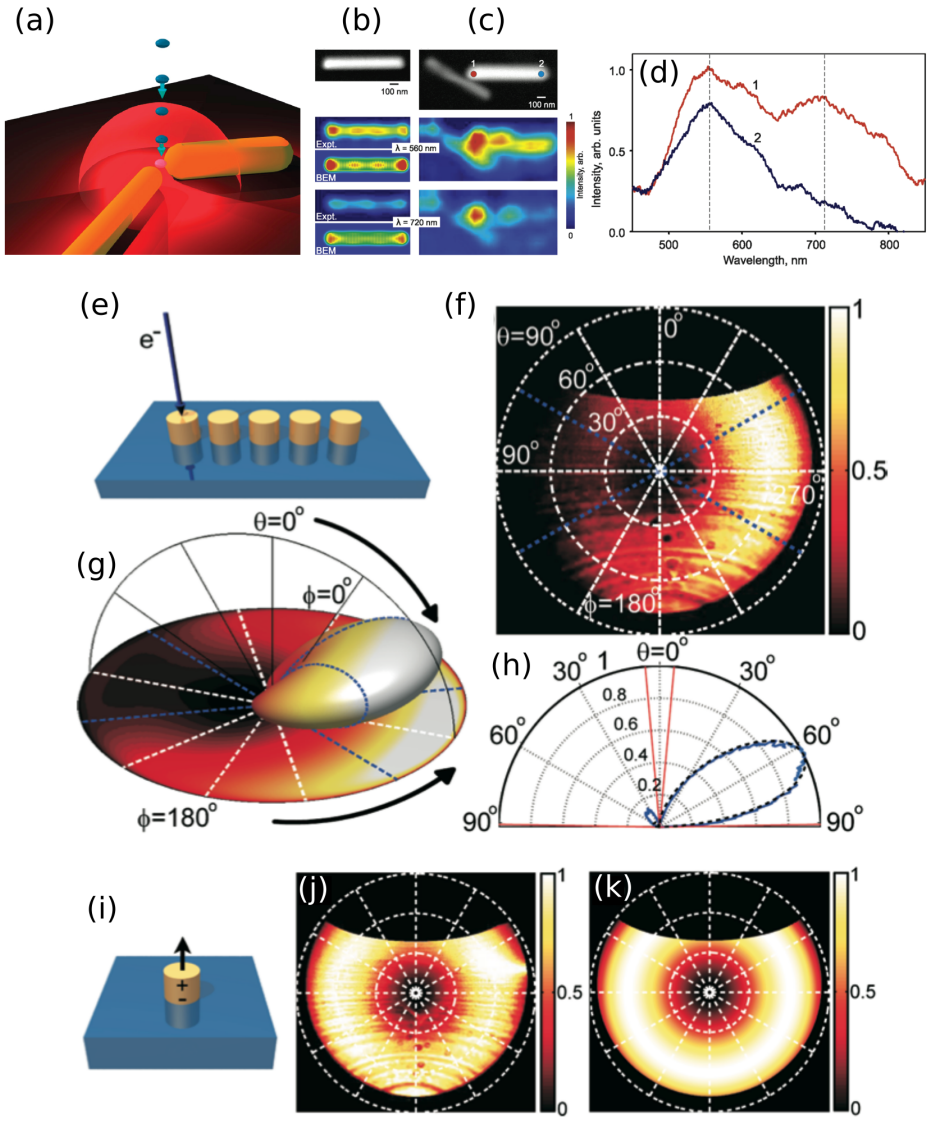

FIGURE 1.10: Electron beam driven antenna designs. (a) Schematic of transmitting nanoscale optical antenna driven by an electron beam at the junction between coupled gold nanorods. (b, c) SEM images and corresponding electron-beam-induced radiation emission (EIRE) excitation efficiency maps at 560 and 720 nm for (b) an isolated gold nanorod, alongside corresponding numerically simulated EIRE maps (bottom), and (c) a pair of coupled gold nanorods. (d) EIRE spectra for electron beam injection points 1 and 2 highlighted on the secondary electron image in (c). (e) Schematic of Yagi-Uda antenna design. (f) Polar CL emission pattern for (e) with a 40 nm band-pass filter centered at 500 nm. (g) 3D representation and (h) cross-cut of radiation pattern for (e). (j) Polar CL emission pattern and (k) calculated emission pattern for a single nanoparticle (i) integrated over all wavelengths from 400 to 1000 nm. (a-d) from [37]. (e-k) from [26].

Metamaterials, traditionally used to interact with free-space radiation, have been shown to enhance both the emission area and intensity of electron impact-stimulated light by acting as collective antennas, propagating the plasmonic effect much further than would a flat, metal film and can also confine emissions directionally. Many metamaterials rely on the resonance of a split-ring resonator element to produce a designed magnetic response. In such a metamaterial, the output field properties depend not only on the independent properties of the resonator, but also on the collective response of the material as a whole, with each element interacting with its neighbors. The same principle applies with electron-beam driven metamaterials: it has been shown that a large array of split-ring resonator metamolecules can be designed to directionally confine its emission through a collective-mode interaction [38]. As shown in figure 1.11, the output beam is confined both spatially and spectrally, increasingly so as more split-ring meta-molecules are driven by the electron beam, demonstrating the collective nature of the beam shaping properties of metamaterials when used as electron-beam driven devices.

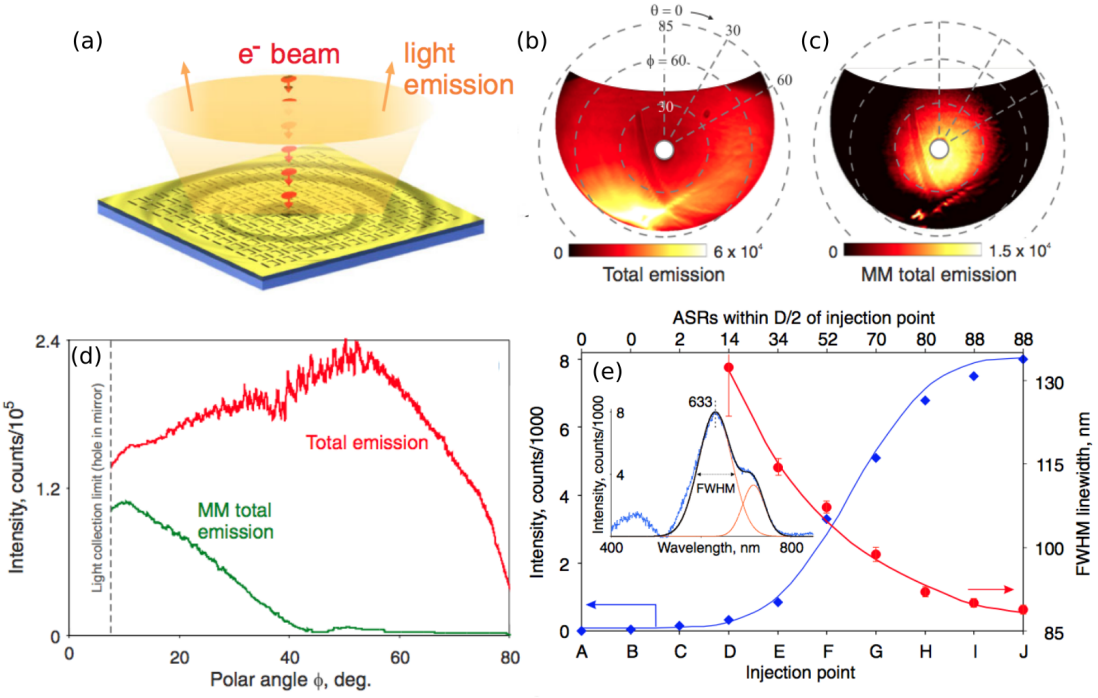

FIGURE 1.11: Electron-beam-driven metamaterial light source. (a) Conceptual image of collective-mode EIRE metamaterial. (b) Metamaterial emission intensity profile including background TR. (c) Emission intensity profile from metamaterial, subtracting TR profile from flat gold. (d) Emission intensity as a function of polar angle (integrated over azimuth angle) for the two cases shown in (b) and (c). (e) Intensity and half-maximum width of the 633nm emission line as functions of the electron beam injection coordinate and the number of metamolecules within the $1 = e/2^2$ source radius of the injection point. From [38].

1.5 Controlling Light with Metasurfaces

Conventional optical elements rely on the bulk properties of a material such as refractive index or absorption to shape the propagation of light. A more recent class of flat, manufactured optical elements termed 'metasurfaces,' aims to accomplish the same functions in two spatial dimensions with an array of subwavelength patterns. Generally, the pattern is designed such that each scattering element imparts a distinct phase shift that, through constructive interference of the emitted light, creates the intended optical function.

While a great deal of research has been put into examining how metasurfaces react to light, fewer applications have, as yet, been demonstrated for EIRE studies. An examination of some of these light-modifying effects, however, can illuminate some potential uses for metasurface-electron interactions.

Metasurfaces, in general, operate by using the resonant properties of geometrically-tuned scatterers to cause abrupt changes in the wavelength, polarisation, or phase-profile of light. Though the response of such surfaces is spectrally narrow, the structural parameters can usually be tuned to include a range of frequencies. This can include rotational polarisation changes usually accomplished with bulk chiral media [39].

While most metasurfaces have been implemented in metallic structures, this frequently limits their operation to reflection-mode outputs to keep the diffraction efficiency high. Recent work has demonstrated that silicon, and potentially other dielectrics, can be used to create efficient transmission-mode metasurfaces [40]. Transmission-mode rotational polarising elements have also been implemented in dielectric materials [41]. Hence, the properties of these 2D structures are ideal for integrating into photonic devices on a range of materials platforms.

The traditional Snell's Laws of refraction and reflection rely on an optical component in which the phase changes of light passing through it occur over long distances compared to the wavelength of light. Subwavelength metasurfaces allow these phase shifts to happen abruptly, and with a precisely set phase shift at a given wavelength, nearly any output direction can be defined for refraction or reflection. Some applications of this generalised Snell's Law are shown in figure 1.12.

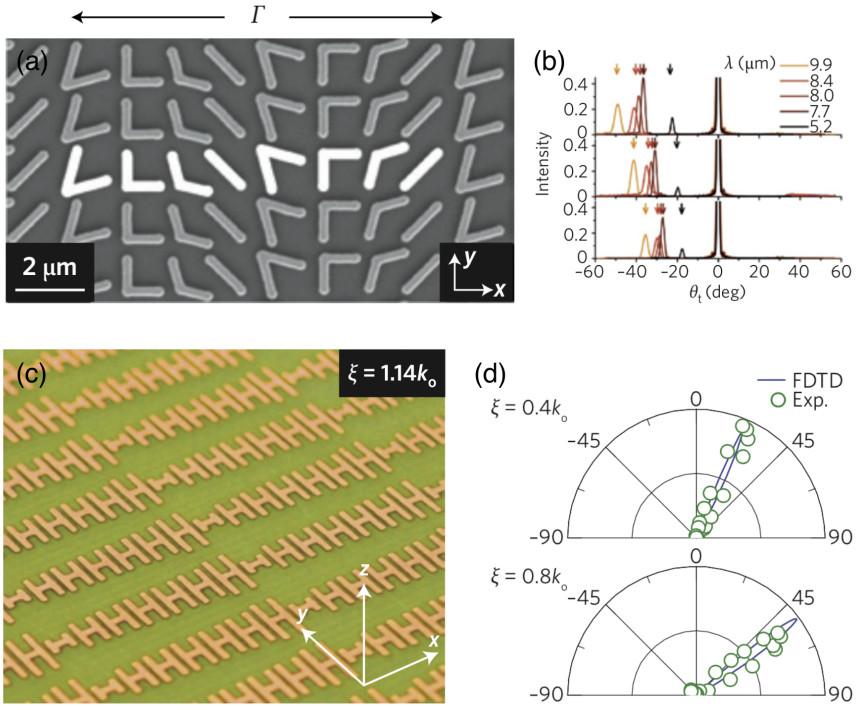

FIGURE 1.12: Examples of metasurfaces composed of phase-shifting antenna arrays. (a) SEM image of a metasurface consisting of an array of V-shaped gold optical antennas, forming a constant gradient of phase change along the interface. The unit cell (highlighted) has length $\Gamma = 11$ μm. (b) Experimental far-field intensity profiles showing the ordinary and anomalous refraction generated by metasurface in (a). The upper, middle and lower panels correspond to $\Gamma = 13$, 15 and 17 μm, respectively. (c) Photograph of a microwave array consisting of H-antennas separated from a metallic back plane by a dielectric spacer. The array introduces an interfacial phase gradient $\xi = 1.14k_0$ where k_0 is the wavevector of the incident beam corresponding to a 2 cm wavelength. (d) Measured and simulated far-field intensity profiles for a microwave array (c) corresponding to $\xi = 0.4k_0$ and $0.8k_0$. (a, b) from [42]. (c, d) from [43].

In any real metasurface however, there will be a range of wavelengths for which the structure has little effect, leading to normally reflected and refracted light. Additionally, most nano antenna geometries impart different phase shifts to different wavelengths across their resonance [44]. Therefore, a designer meta-surface can have any reflected or refracted phase profile for a given wavelength, but designing a broadband metasurface will prove more difficult. However, even with this limitation many applications are achievable. Figure 1.13 shows narrow-band flat optical devices such as a quarter-wave plate [45], optical vortex generator [44], and metasurface plane wave hologram [46].

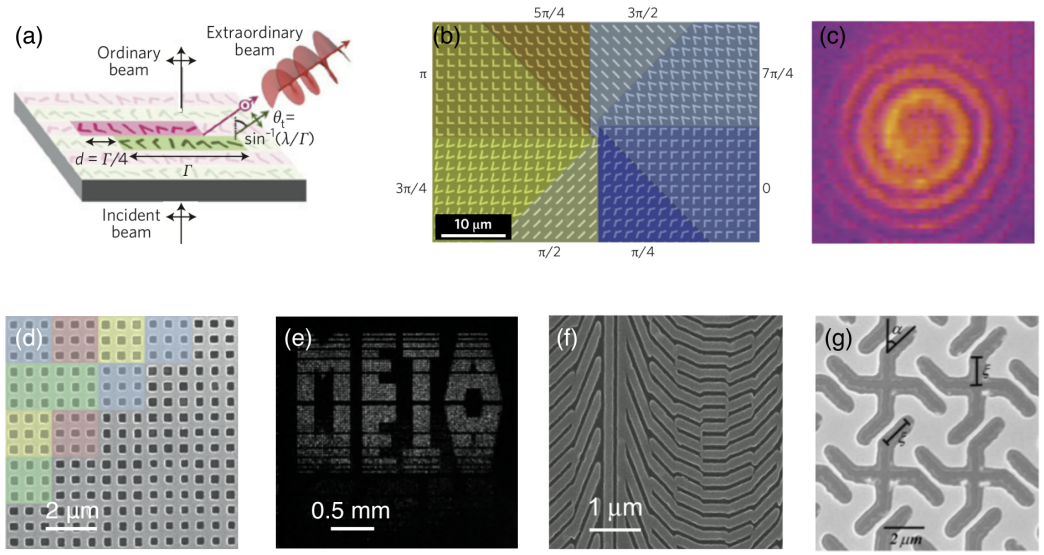

FIGURE 1.13: Examples of nanostructured metasurfaces designed for specific wavelengths. (a) Schematic showing a broadband, background-free metasurface quarter-wave plate. (b) SEM image of the central region of a mid-infrared metasurface phase plate that is able to generate optical vortex beams. (c) Spiral interferogram created by the interference between a vortex beam created by the plate in panel (b) and a co-propagating Gaussian beam. The size of the interferogram is about 30 mm × 30 mm. (d) SEM image of part of a metasurface hologram made of aperture antennas. Different colours represent pixels with distinctive transmission coefficients. Size of image, 9 μm × 9 μm. (e) Transmitted light intensity of the metasurface in panel (d) recorded in the far-field with incident wavelength 905 nm. (f) A dielectric gradient metasurface in polycrystalline silicon on quartz substrate able to alter the circular polarization of a 550nm wavelength incident beam to the opposite circular polarization. (g) SEM image of planar chiral structure capable of altering the azimuthal polarization rotation of incident light by up to ± 15°. (a) from [45]. (b, c) from [44]. (d, e) from [46]. (f) from [40]. (g) from [39].

Certain metasurfaces can also be classified as a type of two dimensional hologram when designed from interference of known input and output wave fronts. Such an interference method will describe the phase shifts necessary for each metasurface element. Indeed, such a metasurface need not be driven by free-space light provided that the near-field of the excitation source is known, as in the case of a plasmonic excitation.

Surface waves have already proven to be extremely useful for holographic techniques. For example, mm-scale metallic structures have been used to alter the direction of Terahertz waves [47]. Here, the structure is large enough that the excitation can be confined to the centre of the structure. The use of careful impedence-matching in the surface unit cell enables control of the output polarisation. Holographic metasurfaces with multispot outputs, and operating on circularly polarised light have also been demonstrated as shown in figure 1.14.

Some holographic metasurface have already been shown interacting with a type of localised receptor - a narrow-aperture plasmonic waveguide - as shown in figure 1.14(a). Here, as the excitation captured by the holographic surface is funneled to the end of the waveguide, the field pattern of the design free-space radiation lends a radial pattern to the hologram. As will be shown, the even more highly confined nature of an electron beam will allow these techniques to be applied to a nanoscale, optical-wavelength holographic metasurface structure.

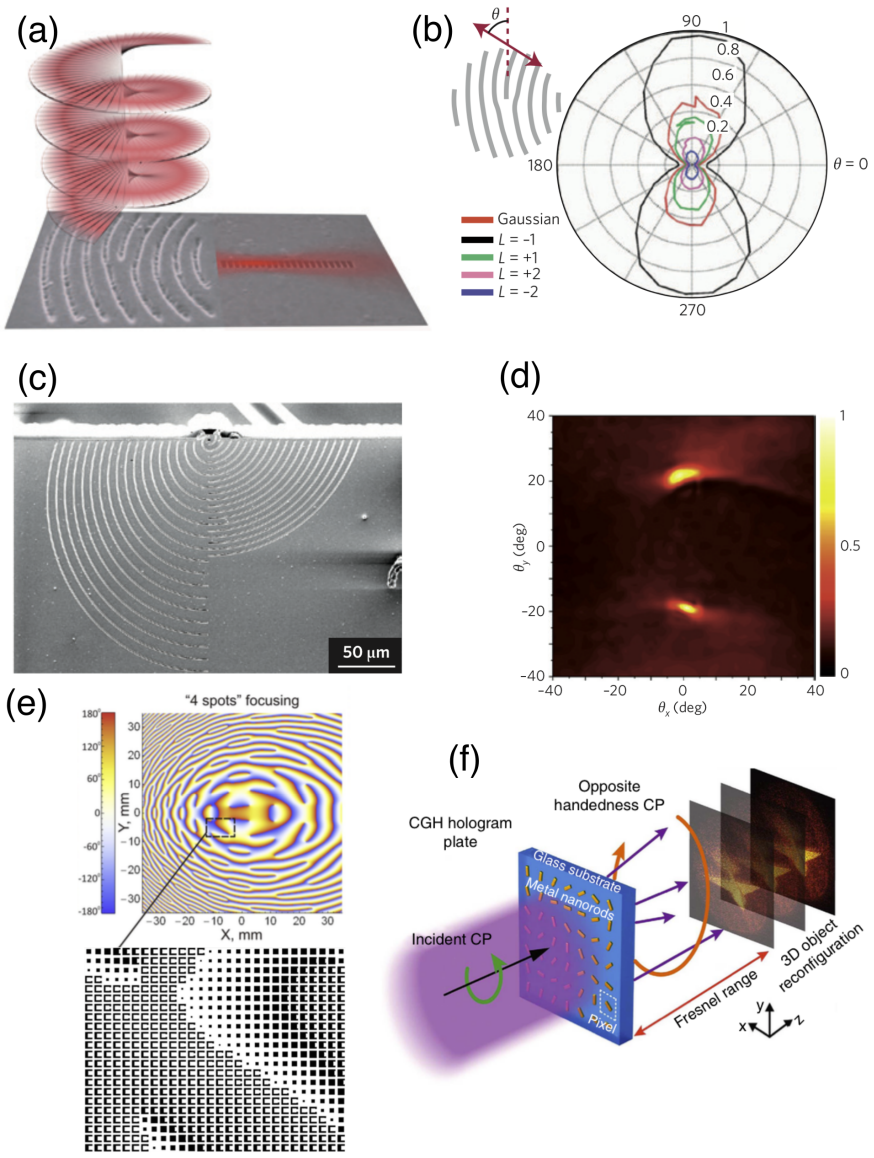

FIGURE 1.14: (a) A holographic coupler consisting of curved, fork-shaped grooves converts an incident vortex beam with topological charge L = 1 into a focused surface wave. (b) Detected photocurrent as a function of the incident polarisation for incident beams with different orbital angular momentum, with inset showing the orientation of polarisation with respect to the structure grooves. (c) SEM image of a plasmonic lens producing two beams from two sets of elliptical grooves, each creating one beam by scattering surface waves generated from an aperture located at the end of a laser waveguide. (d) Measured far-field intensity of the device shown in (c). (e) Metasurface patterns and detail for Terahertz multipoint-focusing hologram. Metallized areas in detail are shown by black. (f) Hologram structure and detail of three-dimensional plasmonic optical hologram metasurface composed of nanorods, each of which has the role of a pixel of diffractive element, which can generate the required continuous local phase profile with normal incidence of one orientation of circularly polarized light. (a,b) from [48], (c, d) from [49], (e) from [50], and (f) from [51].

1.6 Experimental Apparatus

1.6.1 Scanning Electron Microscope Platform

A scanning electron microscope (SEM) provides a flexible, high-resolution platform for performing cathodoluminesence spectroscopy. The system used for these studies is a CamScan CS3000 range microscope fitted with a LaB_6 electron source with 15 ± 2 μm microflat tip. For high-resolution applications a LaB_6 tip provides a significantly more uniform emission surface temperature compared to that of a heated tungsten wire. This leads to an improvement in the energy distribution across the profile of the projected electron beam spot (ΔE) of about 40 eV. The chamber is capable of high-vacuum ($< 10^{-5}$ mB) operation and 5-axis eucentric stage. Figure 1.15 shows the configuration of the instrument used.

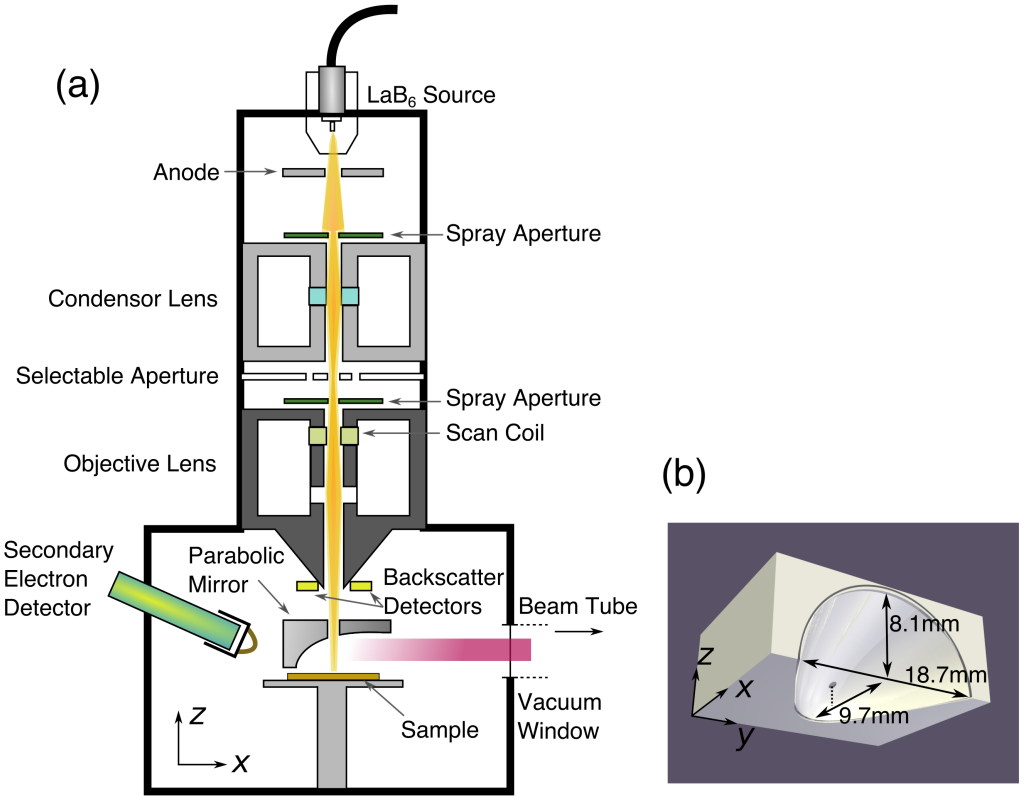

FIGURE 1.15: (a) Schematic of scanning electron microsope column and chamber (Camscan CS3000 system). (b) schematic of mirror block used for angle-resolved cathodoluminescence.

1.6.2 Angle-Resolved Cathodoluminescence Setup

Attached to the SEM system is a dual-spectroscopy CL system comprising two Horiba iHR320 spectrometers arranged as shown in figure 1.16. One of these, attached to a multichannel liquid nitrogen-cooled charge-coupled device (CCD), is configured with gratings of 100 and 600 grooves/mm for CL measurements in the visible to near-infrared (NIR) range. The system is equipped with a parabolic mirror upgrade, shown in figure 1.15(b), with a hole at the focus of the minor axis allowing an electron beam to reach the sample. The mirror is suspended on a gurney so that it can be inserted above the sample as required, and can be translated in the xy-plane via micrometric adjustments. Combined with the z-translation of the SEM stage, this allows a CL sample to be positioned precisely at the focal point of the parabolic mirror, producing a 5×16 mm hemispherical beam representing the polar pattern of emissions.

While such a collection setup makes for efficient analysis of the CL spectrum, an angle-resolved analysis requires some additions. The system was originally aligned with a zinc sulfide calibration sample, allowing the collimated beam to be seen with the naked eye. A Horiba multichannel liquid N_2 cooled CCD camera and blanking shutter were used for image collection, and a plano-convex lens of focal distance 7.5 cm used to focus the collimated beam onto the CCD. Preceding this is a slot for inserting bandpass filters into the beam path, allowing angle-resolved images of a spread of wavelengths to be recorded.

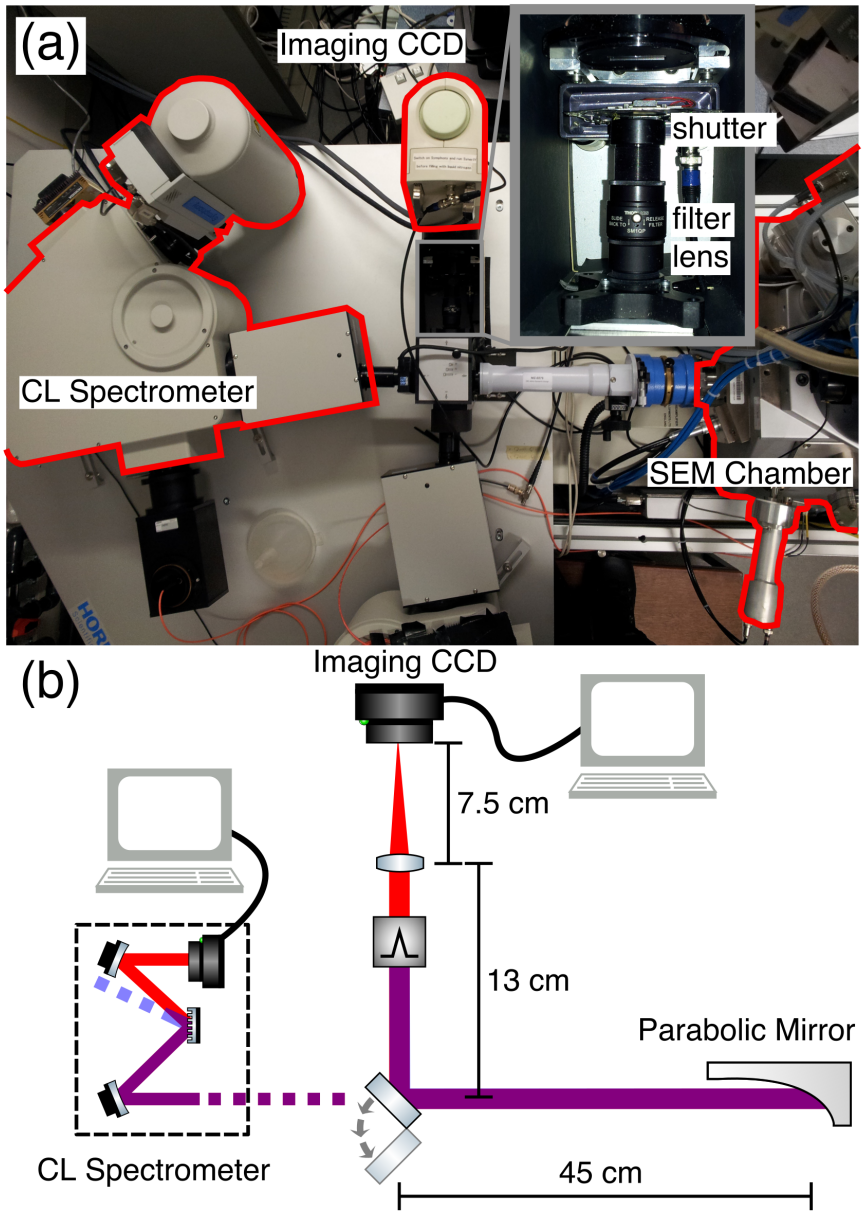

FIGURE 1.16: Optical cathodoluminescent imaging setup. (a) Photograph of instrumental setup shown in schematic (b). Two CCD setups, for CL spectrum and angle-resolved collection are incorporated with the SEM platform.

1.6.3 Polar Transform

The mirror setup shown in figure 1.15 results in a collimated beam, subsequently focused onto the rectangular CCD array. The resulting beam image does not on its own provide an angle-intensity map of light emitted from the sample, but given the dimensions of the collection mirror, this can be calculated via a coordinate transform from pixel position to angular pair (ϕ, θ).

As shown in figure 1.17, given its dimensions, every section of the parabolic mirror in the zy-plane has a known x distance from the focus, upon which the electron beam is incident. For every pixel of the CCD detector image, the x, y, and z position of the corresponding reflection point on the mirror relative to the mirror focus can therefore be determined. The polar and azimuthal angles θ and ϕ respectively are then in standard cylindrical coordinates:

$$\theta = arctan(\sqrt{y^2 + x^2}/z), \phi = arctan(x/-y); \tag{1.1}$$

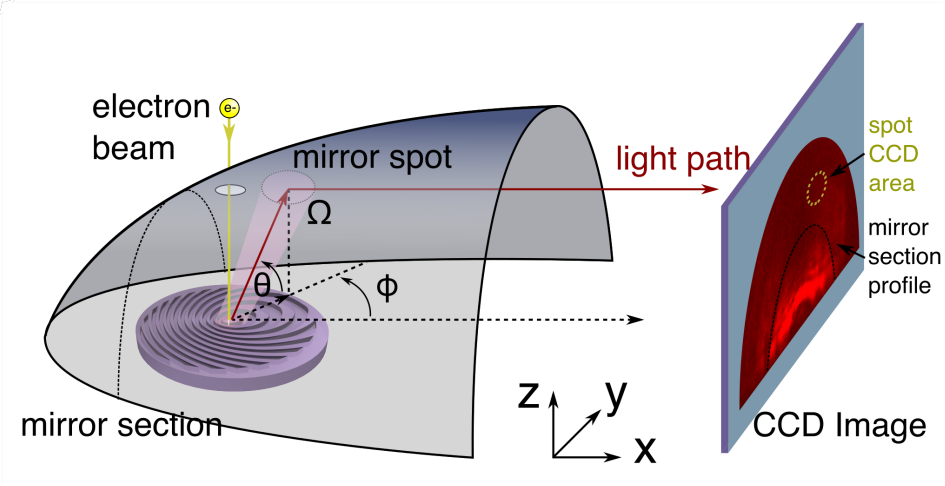

FIGURE 1.17: Illustration of mapping between sample space in cylindrical coordinates to CCD. For each pixel there is a corresponding mirror position (x, y, z). For each yz-plane section, there is a solid angle Ω occupied by the pixel as shown in figure 1.18(c).

However, since not all zy-plane sections along the paraboloid are of equal size, the pixels on each corresponding arc of the CCD represent a different area of the mirror. Accordingly, pixels on smaller arcs will be relatively brighter as they account for a larger solid angle of emission from the sample. To obtain a reliable map of sample emissions, CCD pixels must therefore be normalized according to the relative solid angle (Ω) encompassed by the mirror spot of each. For a pixel corresponding to a mirror spot on a yz-plane section at position x_{sect} with y and z dimensions from y_0 to y_1 and z_0 to z_1 the solid angle is then:

$$\Omega = 4x_{sect} * \int_{y_0}^{y_1} \int_{z_0}^{z_1} (y^2 + z^2 + x_{sect}^2)^{-3/2} dz dy \tag{1.2}$$

From the mirror dimensions and the above equations, the angle of each pixel and the solid angle encompassed by it can be calculated. These maps, shown in figure 1.18 are applied to each sample image obtained to determine the intensity output at each angle.

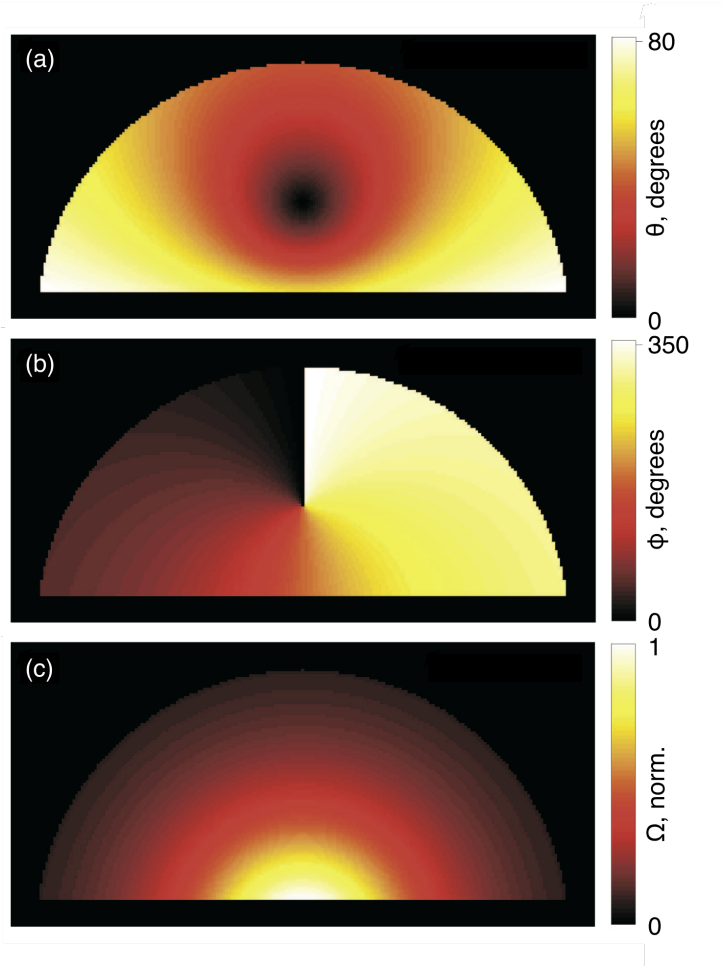

FIGURE 1.18: (a) Polar (θ), (b) azimuthal (ϕ), and (c) solid angle (Ω) of each pixel in CCD used to record data, corresponding to mirror dimensions shown in 1.15.

1.6.4 SEM External Scanning Controller

The experiments conducted in Chapter 3 require the precise switching of the electron injection point between pre-defined points on the sample, in coordination with the CCD controller. This interfacing is accomplished with a National Instruments BNC-2111 interface and associated PC running a custom virtual instrument (VI). The connections are shown in figure 1.19. The CCD shutter voltage is read into the interface, which, when triggered by a shutter open signal, times the electron beam position for a variable number of points.

To calibrate the external scan voltages necessary to accurately position the beam at the required sample positions, the secondary electron detector (SED) voltage was read into the interface as the scan voltages were swept across the sample, generating an image which could be correlated with known sample dimensions. The USB connection of the interface introduced a small amount of lag between the shutter and scan voltages. This was measured by pairing the interface with an oscilloscope-function generator to simulate the shutter signal and was recorded as being approximately 5 ms.

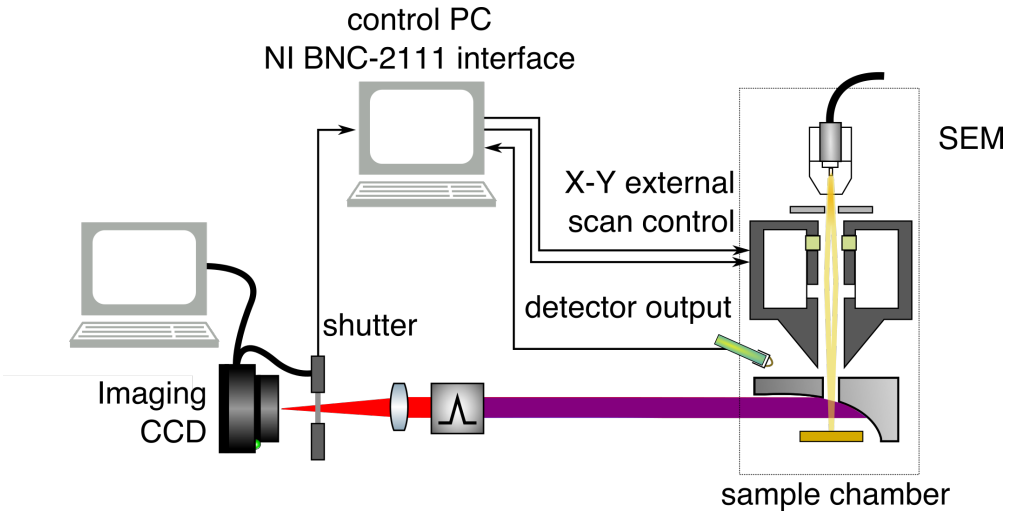

FIGURE 1.19: External scan control setup for SEM. Shutter voltage is used as a trigger for scanning the electron beam among multiple sample points in repeatable fashion.

1.7 Thesis Overview

This thesis reports on novel approaches for controlling the emission of light generated by electron-beam driven nanoscale metasurfaces. These applications are demonstrated on the SEM platform described in section 1.6 by way of plasmonic, semiconductor, and dielectric surface-relief structures, showing unprecedented control of divergence, directionality, and topological charge of light.

Chapter 2 focuses on the conception, fabrication, and first experimental demonstration of a free-electron driven holographic metasurface light source, capable of controlling full wavefront parameters. This is shown with the actualisation of an optical vortex generating device.

Chapter 3 focuses on the first experimental demonstration of a direction-division multiplexed holographic free-electron-driven light source with selective output based on electron injection position. This use of a metasurface structure allows for small arrays of emitters with potentially rapid switching of output.

Chapter 4 demonstrates the applicability of the holographically-designed metasurface to emissions from non-plasmonic materials, thereby showing control of the transition radiation component of EIRE light.

Chapter 5 demonstrates the applicability of nanoscale sub-periodic structuring to controlling Smith Purcell radiation from a grating driven by a free-electron beam.

Finally, the work covered in this thesis is summarised in Chapter 6, together with an outlook of the potential routes of further investigation for the experimental discoveries reported here.

Chapter 2

Holographic Free Electron Light Source

2.1 Introduction

Progress in metamaterial and metasurface research has led to the theoretical prediction of facinating new phenomena in slow light [52], transformation optics [53, 54], flat optical elements [55, 56], and optical cloaking [57]. Based on structuring of materials at sub-wavelength scale, metamaterials provide a diverse toolkit of optical elements to control and manipulate the amplitude, polarization, photon energy, and momentum of light in free-space systems.

In addition, recent advances in nanofabrication technologies such as high-resolution FIB milling and improved understanding of near-field light/matter/free-electron interactions are now enabling the extension of such control to the nanoscale and have made the production of small, functional devices much simpler. This has enabled the development of nanoscale-resolution techniques for such applications as studying nanoparticle structural transformations [58, 59], characterizing luminescent materials [60, 61], and time-resolved spectroscopy [25, 62]. The coupling of light into well-defined free-space modes of photon energy, momentum, and polarization has been made possible with the help of photonic crystals [63], surface waves [64–66], nanoantennas [27, 35, 67], and photonic metamaterials [28, 68].

As applicable as these devices have been to the study and manipulation of incident light, they are equally so to the experimental realisation of charged-particle driven devices, where theoretical models may struggle to fully explain all the interactions. For example, the study of light emitted from a substance upon the impact of an electron beam, termed

cathodoluminescence (CL) from the original use of a cathode ray on glass, has progressed substantially from its roots in the mid-19$^{\text{th}}$ century. The characteristics of CL light come from both the structure and material composition of objects and are frequently useful in a wide array of fields such as geology, metallurgy, and semiconductor technology. In addition, modern electron beam systems provide a great degree of flexibility in using CL to generate novel light sources.

The combination of advances in the technology of nanofabrication and computational modelling of the physics of charged particle interactions with materials and photons has allowed for a deep understanding of light generation via free-electron proximity and impact interactions with nanostructures such as mapping plasmon propagation [7, 69], the optical states of photonic crystals [70], and modes of nanoparticles [20, 21]. Electron beam excitations have been used to control emitted light in nanoscale systems such as plasmonic nanoantennas [26, 36, 37], cylindrical metal-dielectric undulators [71], and collective oscillating metamolecule ensembles [38]. However, these electron-driven structures have typically been constrained to controlling the direction and polarization of emitted light.

This chapter sets forth the principles and applications of using electron-beam induced excitations in conjunction with a holographically-designed structured surface to shape light output with control over all wavefront parameters including direction of emission, wavelength, and phase profile. Holography was originally conceived as a technique for increasing the resolution of scanning electron microscopes [72], but has come to be widely recognised as the ultimate method of achieving three-dimensional optical reconstruction of objects. I have now applied these holographic concepts to controlling the wavefront of emission from charged particle injection. I demonstrate this control using medium-energy free-electron beam to generate highly-directional visible to near-infrared light, at selected wavelengths in prescribed azimuthal and polar directions, with brightness two orders of magnitude higher than from an unstructured surface, and vortex beams with topological charge up to ten. Such emitters, with micron-scale dimensions and the freedom to fully control radiation parameters, offer novel applications in nano-spectroscopy, nano-chemistry and sensing, up to relativistic electron energies.

2.2 Structure Design and Fabrication

As described in section 1.5, the tools available for shaping the output of light from a point excitation in a plasmonic material with nanoscale structures are diverse. In particular, the use of holographic techniques in computationally generating such a structure has shown promising results. In this section, we describe the design, fabrication, and testing of a flexible means of precisely controlling the wavefront of light emanating from a singular nanoscale emitter by locating it in a nanostructured environment designed according to holographic principles.

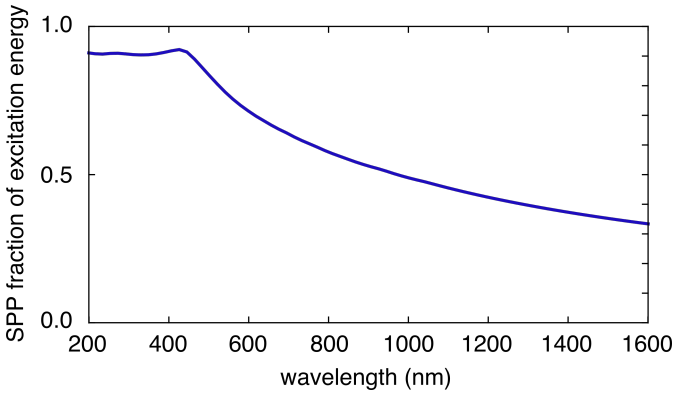

FIGURE 2.1: SPP fraction of excited SPP and TR radiation over a range of wavelengths for the current design case: an unstructured Au surface being driven by 30 keV electron beam [73].

As outlined in section 1.2, a charged particle crossing the boundary between two different media generates transition radiation (TR) [6], with a spectral distribution and intensity related to the relative permittivities of the media and the electron energy. On metal surfaces such impacts also generate surface plasmon polaritons (SPPs) propagating radially from the impact point. Indeed, for certain metals at certain frequencies and electron energies the efficiency of coupling to SPPs may be greater than to TR. Figure 2.1 shows the amount of excitation energy from a 30 keV electron beam that results in SPPs as a fraction of plasmonic and transition radiation combined. SPPs can only contribute to free-space (far-field) light emission in the presence of a decoupling structure such as a grating; TR is otherwise the dominant optical output component [73, 74]. The TR from an electron normally incident on a metal surface has a cylindrically symmetric toroidal emission pattern (illustrated schematically in figure 2.2(a) very similar to that of a dipole aligned with the surface-normal (at a distance from the surface $h << \lambda$, where λ is the light wavelength). Indeed, for numerical modelling purposes, an electron impact excitation on a metal, including SPP generation, can be accurately represented as such [73–76].

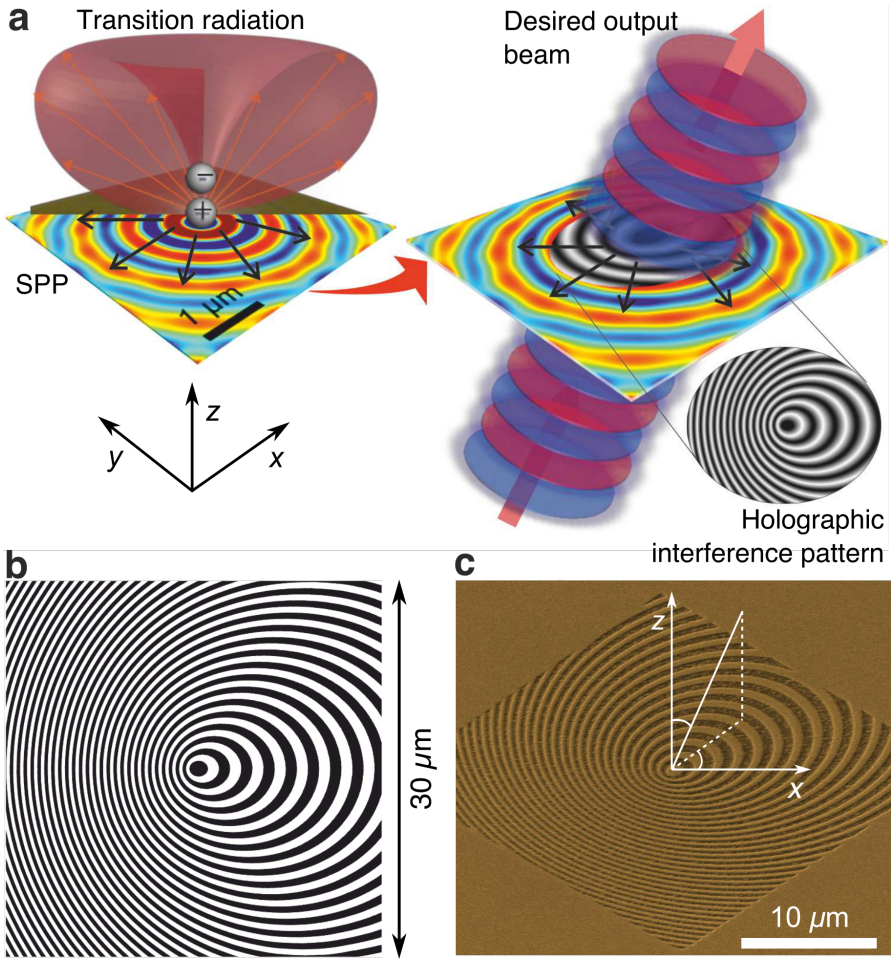

FIGURE 2.2: Holographic free-electron light source design. (a) The electromagnetic excitation resulting from normally incident free-electron impact on a metal surface is computationally replicated by an electric dipole located in close proximity to the surface. The holographic mask required to couple this excitation to a desired output beam is obtained via the interference of the dipole-generated near-field and the required output field, as schematically illustrated for a collimated plane wave at an oblique angle to the surface-normal. (b) Binary version of the as-generated greyscale interference pattern required to produce, from the impact of 30 keV electrons on a gold surface, an output beam at a wavelength of 800 nm directed at 30° to the surface-normal. (c) False color scanning electron microscope image of the pattern from panel (b) fabricated on an optically thick (140 nm) gold film.

To tailor output to the optimal range of our CCD detector hardware and avoid strong peaks in the cathodoluminescent spectrum of Au, we selected an emission design wavelength $\lambda = 800$ nm for the present study, which in experiment utilizes 30 keV electrons normally incident on gold surfaces. In a computational algorithm developed in collaboration with visiting student Guanhai Li from the Shanghai Institute of Technical Physics, the corresponding numerically simulated distribution of electromagnetic field in the gold/vacuum interface plane (shown in figure 2.3 for 600, 700, 800, and 900 nm wavelengths) is employed as the reference field (in holographic parlance) to generate an interference pattern with an object light field corresponding to the desired output

wavefront, which by inversion defines the 2D surface structure required to regenerate the object (output) beam from an electron-impact excitation.

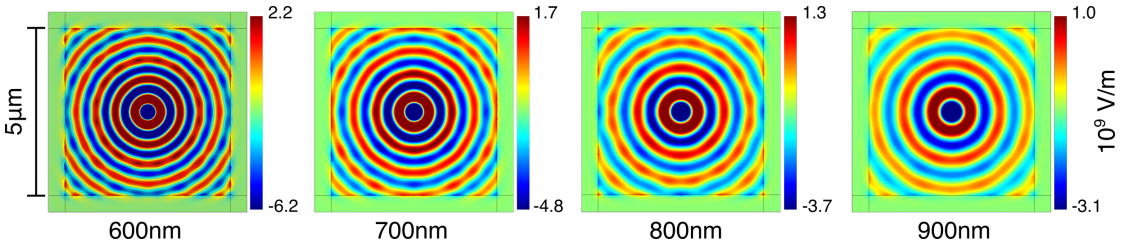

FIGURE 2.3: Normal electric field component on Au surface for a reflected dipole, simulated for hologram design wavelengths.

For example, a plane-wave object beam propagating at a polar angle of 30° to the surface normal produces the pattern of offset concentric oval rings shown inset to figure 2.2(a). The interference pattern obtained is converted to a binary mask [77, 78] (figure 2.2(b)) for ease of fabrication by focused ion beam milling on an optically thick (140 nm) polycrystalline gold film (figure 2.2(c)) deposited by resistive evaporation. It should be noted that the computed holographic (interference) patterns are two-dimensional, i.e. they provide no information on the required height/depth of surface-relief features for optimal coupling efficiency, which will generally depend on the relative efficiencies of SPP and TR generation [73], emission wavelength and polar angle [79].

The optimum depth of a plasmonic grating structure is known to be a complex function of wavelength, material, and aspect ratio. However, literature has shown that in the case of plasmonic Au, SPP coupling efficiency is relatively flat for rectangular gratings of depths from 30 to 100 nm [79, 80]. For the present case the etch depth of 60 nm was chosen to be within this range and the invariance of out-coupling efficiency for 800 nm emission at angle $\theta = 30°$ verified computationally (in simulations, by collaborator G. Li, of a binary gold surface-relief hologram driven by a dipole source at $h = 50$ nm, constrained to a 10 by 10 μm xy-domain) as well as experimentally, as shown in figure 2.4.

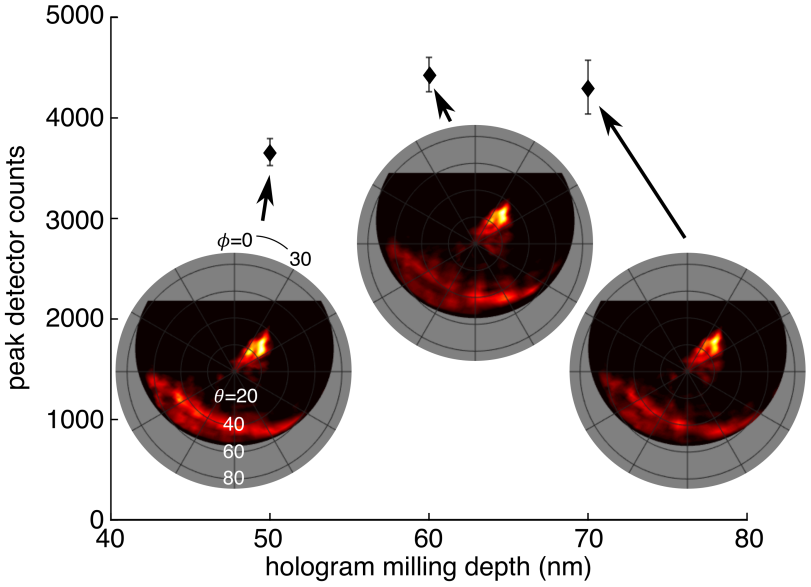

FIGURE 2.4: Polar emission patterns of initial samples used to optimize intensity. Samples around the numerically optimised depth were fabricated to confirm structure depth of greatest emission efficiency.

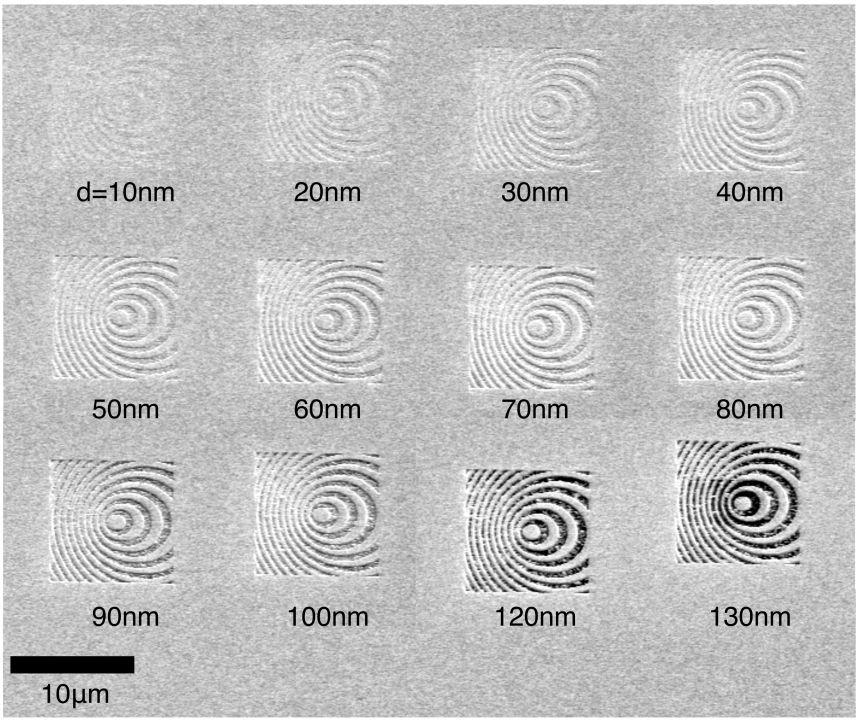

FIGURE 2.5: Composite SEM of samples used to optimize milling depth. Evidence of through-milling begins to appear above 80 nm milling depth.

Initial test samples with edge lengths of 10 and 15 μm were fabricated in 140 nm thick polycrystalline gold film, deposited on a Silicon Nitride substrate using thermal evaporation. These were tested in the apparatus described in section 1.6. Though the samples did emit somewhat, upon examining the structures, we observed that significant delamination had occured as shown in figure 2.6, likely due to heating with the electron beam.

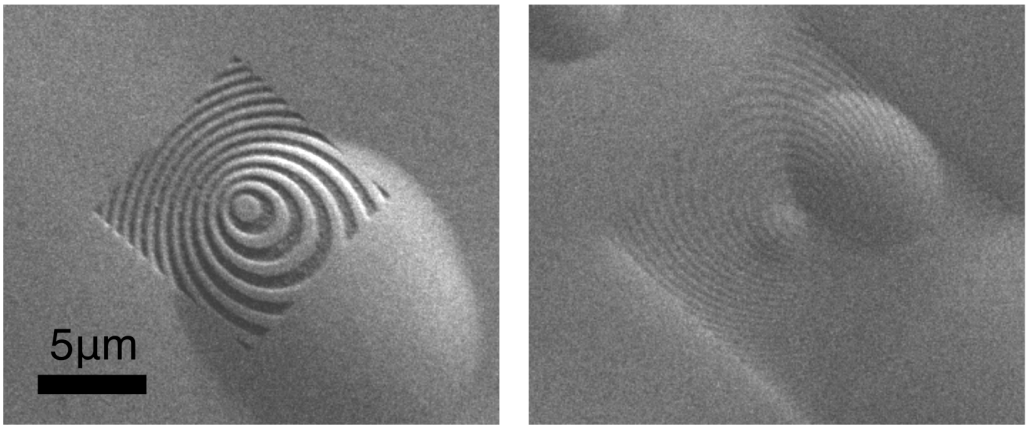

FIGURE 2.6: SEM image of initial holographic metasurface samples fabricated on Silicon Nitride showing delamination of gold film due to heating.

A second array of samples, with edge length 10 μm was fabricated in 140 nm thick polycrystalline gold on double-polished quartz substrate. This provided both superior adhesion and flatness for testing the samples. Initially, an array of several samples at depth increments of 10 nm were fabricated, as shown in figure 2.5. As seen in the image, small parts of the structure are milled to the quartz layer beginning at a depth of about 90 nm.

The samples near the depth calculated to have the highest efficiency were aligned and tested in the angle-resolved setup described in section 1.6.2, and the results shown in figure 2.4. Following verification of the optimal hologram depth, an array of larger sample sizes were fabricated, ranging from 10 to 50 μm in edge length, at design wavelengths of 600, 700, 800, and 900 nm as described in figure 2.9.

2.3 Experimental Results

Figures 2.7(b) and 2.7(c) present the 800 ± 20 nm light emission distributions for electron injection, at a beam current of 12 nA and acceleration voltage of 30 keV, respectively on the unstructured gold surface and at the center of the holographic nanostructure shown in figure 2.2(c). (The asymmetry seen in the broadly divergent transition radiation pattern from the unstructured surface - figure 2.7(b) - is an instrumental artefact related to mirror alignment imperfection and does not depend on sample rotation or polycrystalline domain orientation.) In stark contrast to the flat gold surface, the holographic nanostructure produces strongly directional emission at $\theta = 30°$, as per design (figure 2.7(c)) with a peak emission intensity in the selected direction that is increased by around two orders of magnitude.

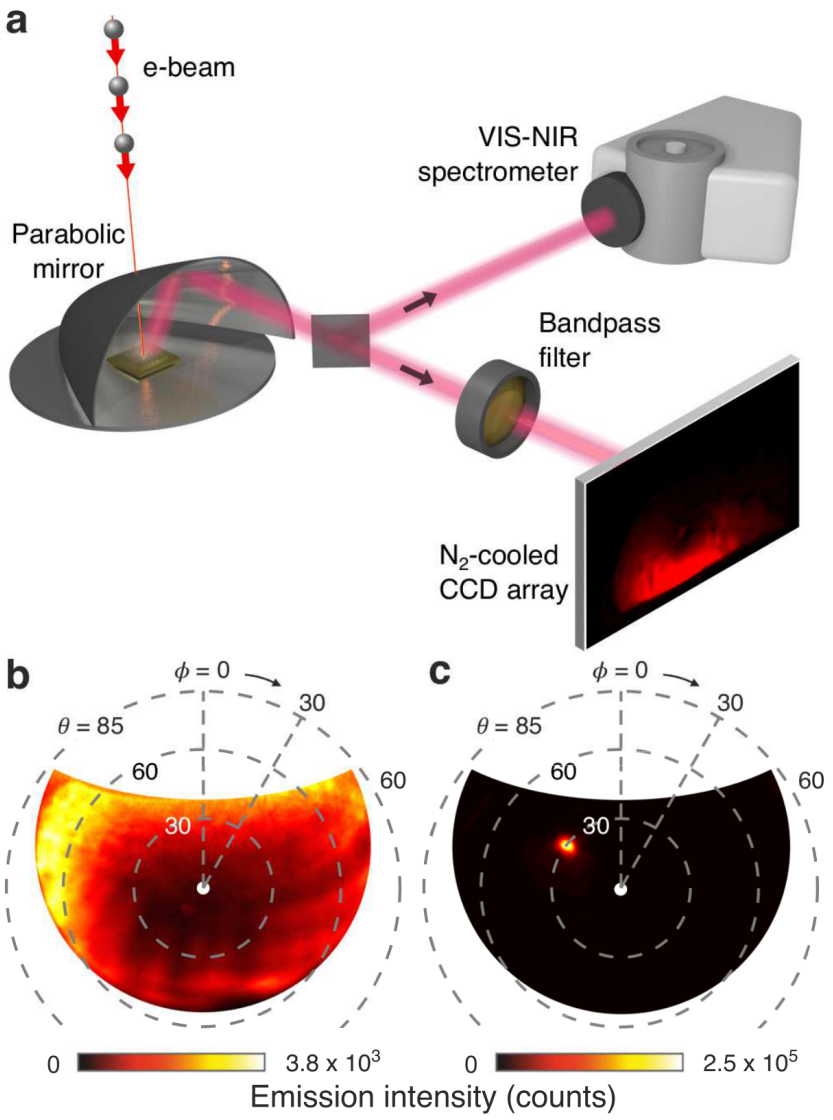

FIGURE 2.7: Angle-resolved spectroscopy of the electron-induced light emission (a) Schematic of the scanning electron microscope-based system for angle-resolved electron-induced light emission spectroscopy. Electrons impinge on samples through a small hole in a parabolic mirror, which collects and collimates emitted light, the beam being subsequently directed to either a spectrometer or imaging CCD [for simplicity, lenses/mirrors/apertures in these paths are not shown]. (b, c) Angular distribution of 800 ± 20 nm light emission induced by electron-beam impact (b) on an unstructured gold surface and (c) at the center of a 30 μm $\times$ 30 μm holographic mask in gold, designed to produce a plane wave 800 nm output beam at $\theta = 30°$ [the azimuthal angle ϕ being arbitrarily set by in-plane sample rotation beneath the incident electron beam; signals are integrated over a 20 s sampling period

The holographic nanostructure is essentially a diffractive element, which implies that it should exhibit a dispersive response for light emission at wavelengths other than the design wavelength. This is illustrated in figure 2.8(b), where emission intensity integrated over all azimuthal angles is plotted as a function of polar angle for emission wavelengths, 600, 700, 800, and 900 ± 20 nm. Shorter/longer wavelengths are directed at smaller/larger polar angles respectively, with peak emission intensity falling on either side of the structural design wavelength as the phase mismatch among waves scattered at different locations on the structure grows.

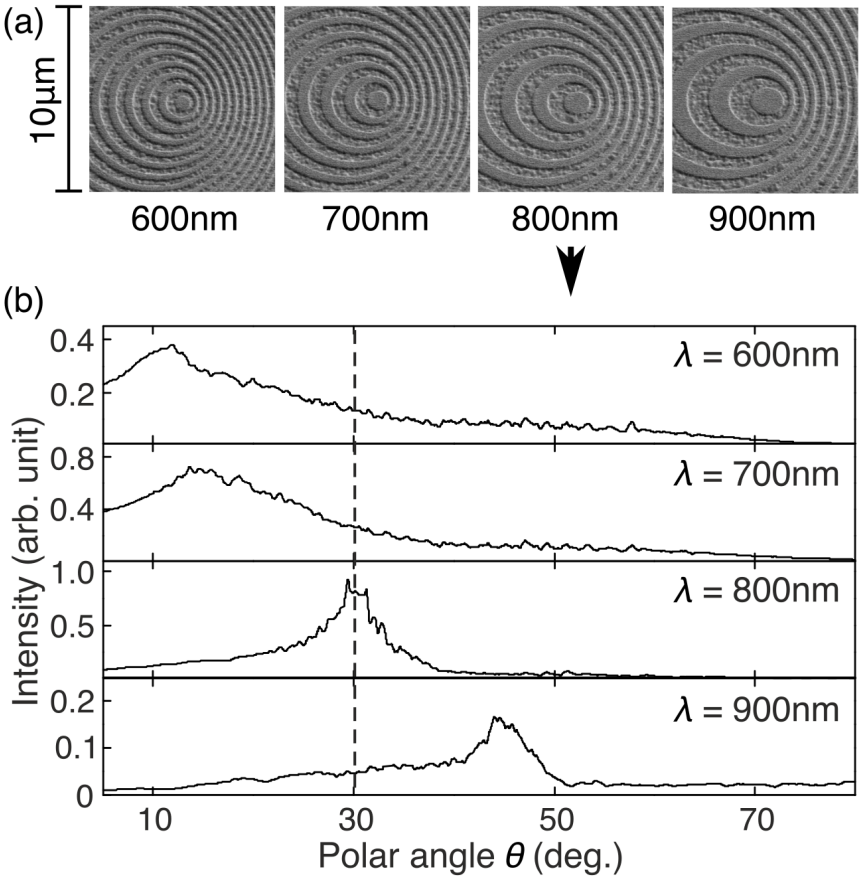

FIGURE 2.8: Angular dispersion performance of gold surface holographic light sources. (a) SEM images of four holographically designed samples to emit 600, 700, 800, and 900 nm light at a polar angle of 30° to surface normal. The 800 nm sample shown is used to generate plot (b), emission intensity as a function of polar angle θ (integrated over all azimuthal angles) in 40 nm wavelength bands centered at 600, 700, 800 and 900 nm, for a 30 μm × 30 μm pattern engineered for 800 nm emission at $\theta = 30°$ [electron beam current = 6.1-6.3 nA; integration time = 30 s].

One would also expect the performance of holographic nanostructures to depend on their size, i.e. on the number of constituent scattering elements, and this is clearly seen to be the case: Figure 2.9(a) shows peak 800 nm emission intensity and spot size as functions of in-plane pattern size for a set of hologram dimensions from 10 μm by 10 μm to 50 μm by 50 μm. Emission intensity increases and spot size (c.f. beam divergence) decreases as the pattern size increases at a rate consistent with the ~25 μm exponential propagation length of SPPs on an unstructured polycrystalline gold surfaces at the design wavelength [7, 81].

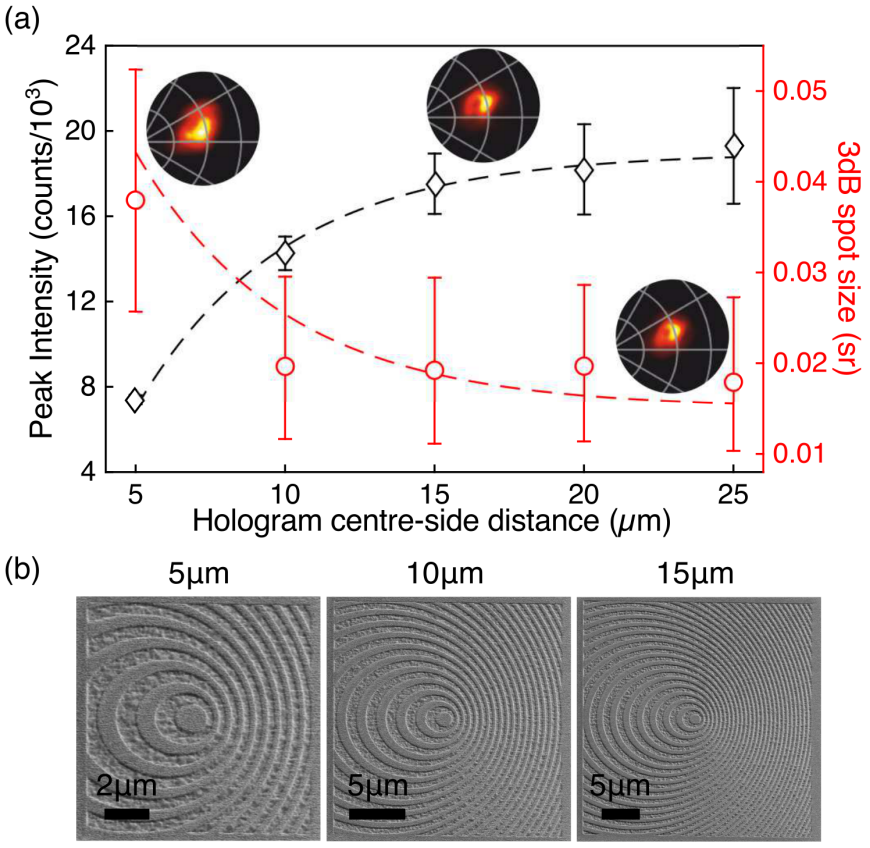

FIGURE 2.9: Beam divergence performance of gold surface holographic light sources. (a) Peak intensity and 3 dB full-width half-maximum spot size of 800 ± 20 nm light emission [evaluated at the brightest pixel and as solid angle around said pixel respectively] as functions of the in-plane dimensions of the holographic structure in microns [beam current = 5.0-5.2 nA; integration time = 30 s; dashed trend lines are exponential curves with a growth/decay constant of 20 μm; Sections of angular emission intensity distributions are shown inset for holograms with center-edge distances of 5, 15 and 25 μm [polar and azimuthal grids are in 15° and 30° steps respectively]. (b) SEM images of samples used to measure spot sizes from holograms of 5, 10, and 15 μm centre-to-side distances in (a).

The holographic design approach can readily be applied to generate more complex wavefronts than the plane-wave considered thus far. To illustrate this, we fabricated holographic nanostructures encoded with optical vortex beams [82]. Such beams have a phase that varies in a corkscrew-like manner along the direction of propagation, described by azimuthal phase dependence $e^{il\phi}$, where ϕ is the azimuthal angle with respect to the beam axis and l is an integer known as the topological charge (TC) ($l = 0$ representing a plane wavefront). They are non-diffracting, have a characteristic ring-shaped intensity profile and carry orbital angular momentum that can be transferred to illuminated objects, making them particularly interesting for optical trap and tweezers applications [83, 84]. Holographic structures were designed to generate optical vortex beams of varying topological charge, again at a polar angle $\theta = 30°$ and a wavelength of 800 nm, for an electron energy of 30 keV. These comprise patterns of interlocking spiral arms, with the number of arms corresponding to the topological charge, as illustrated in figure 2.10a for $l = 3$, 6 and 9. Figure 2.10b shows the far-field distribution of the light emitted from holographic nanostructures of $l = 3$, 6 and 9 respectively. The observed ring-shaped intensity profile, with a central intensity null arising as a consequence of the phase singularity on the beam axis, is a defining characteristic of vortex beams. The expected increase in ring radius with topological charge, as $\sim [l + 1]^{1/2}$ (analytically derived in Ref. [85]), is very clearly seen in figure 2.10(c). Correspondingly, optical vortex intensity drops off sharply for large TC. Figure 2.11 shows the optical output for all fabricated samples from TC 1 to 30. Here, the raw CCD images of TC 10, 20, and 30 are shown for comparison as the pixel resampling necessary to convert from CCD image to polar transform results in some loss of detail. Even for TC = 30, evidence of optical vortex emission is still seen in the lower right portion of CCD image 2.11(q).

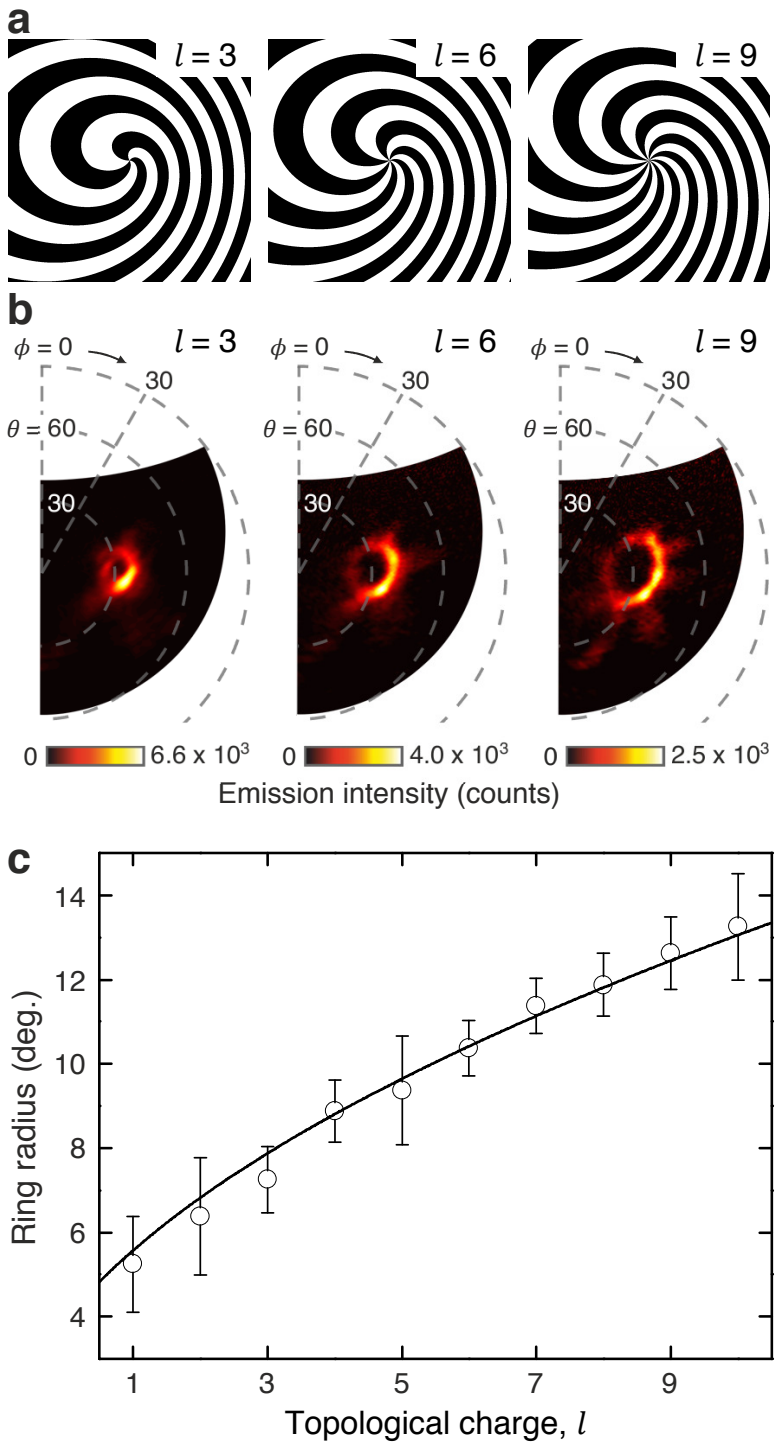

FIGURE 2.10: Generation of optical vortex beams. (a) Central portions of binary holographic masks for gold surface electron-beam induced generation of optical vortex beams with topological charge $l = 3$, 6 and 9 and (b) corresponding angle-resolved emission intensity distribution maps [electron beam current = 5.5-6.1 nA; integration time = 30 s]. (c) Radius of the ring-shaped vortex beam intensity profile as a function of topological charge l, with a fitting of the form $A(l+1)^{1/2}$. The factor A is employed here as a fitting parameter, taking a value 3.937° [analytically it should depend on wavelength and propagation distance from the vortex beam source[44].

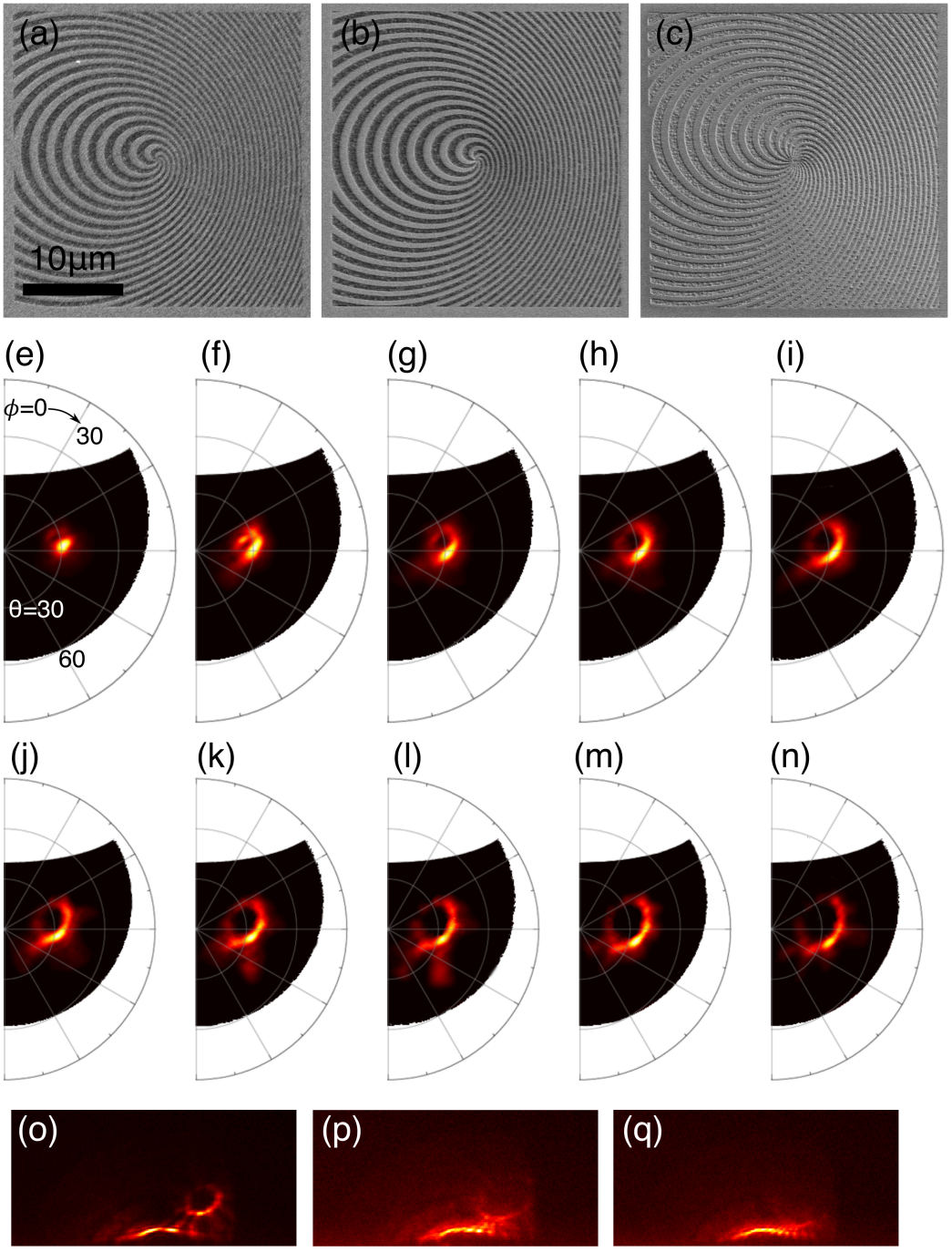

FIGURE 2.11: Results of higher topological charge design holographic samples. (a-c) SEM images of hologram samples designed for topological charge of 5(a), 6(b), and 20(c). (e-n) Polar distribution of light from hologram samples of topological charge from 1 to 10, respectively. (o-q) CCD images of hologram samples of topological charge 10, 20, and 30 respectively.

2.4 Conclusion

In summary, we have shown experimentally that holographically nanostructured surfaces can be employed to control the wavefront of light emission from nanoscale sources. The concept is demonstrated in application to the transition radiation and surface plasmon polaritons generated by electron beam impact on a metal (gold) surface, with holographic patterns engineered to produce directed, low-divergence, directional plane wave and optical vortex beams. Brightness (evaluated in photons per unit solid angle per electron) at the design wavelength is enhanced by as much as two orders of magnitude in the present case, and stronger enhancement may be achieved at shorter wavelengths where electron-induced excitation of SPPs is more efficient.

The control of energy transfer and conversion, in particular the generation of light, in nanoscale systems is a technological challenge of great and growing importance. With micron-scale dimensions and the freedom to fully control radiation parameters, holographic free-electron light sources offer novel applications in such areas as nano-spectroscopy, nano-chemistry and sensing. With an appropriate reference field model, the approach can be adapted to a variety of nanoscale point source emitters, for example quantum dots and fluorescent molecules, to other substrate media, and to higher electron energy domains. The use of continuously-variable-depth, as opposed to binary, holographic nanostructures and phase-gradient metasurface patterns [44] may add additional degrees of freedom to the control of emission spectrum/wavefront and device efficiency without the complications of multilayer device architectures.

Chapter 3

Direction-Division Multiplexed Holographic Free-Electron-Driven Light Sources

3.1 Introduction

Here we report on a free-electron-driven light source with controllable direction of emission. It comprises a microscopic array of surface-relief holographic plasmonic segments, tailored to direct the electron-driven light emission at a selected wavelength into a collimated beam in a prescribed direction. The directional-division multiplexed light source is tested by driving it with the 30 keV electron beam of a scanning electron microscope, while emission, at a wavelength of 800 nm, can be switched among different polar and/or azimuthal output angles by micron-scale repositioning of the electron injection point. This light single-layer, binary pattern surface relief source can be rapidly switched and may be applied to field emission and surface-conduction electron-emission display technologies, optical multiplexing and to charged particle beam position metrology.

At the nanoscale, as indeed at all dimensional scales, numerous applications call for manipulation of (or ideally, active control over) the wavelength, direction, divergence, and polarization of light emission/propagation. An enormous variety of photonic crystal, plasmonic and metamaterial/surface structures, including dynamically reconfigurable structures [5], seek to answer the various aspects of this call. With a large number of two-dimensional patterns and periodic repeating structures emerging that can be used to direct, generate, and modulate light for numerous applications in both free-space and waveguide systems.

While 2D plasmonic structures are useful for coupling free space light to the nanoscale, they are also readily adapted to directing emission from sub-wavelength excitations. In the particular context of EIRE, emission wavelength is typically a function of electron energy [6, 86], and an assortment of plasmonic nanoantennas [26, 37], cylindrical metal-dielectric nano-undulators [71], and collectively oscillating plasmonic metasurface resonator ensembles [38] have been engaged to couple medium-energy free-electron excitations to well-defined free-space light modes. Cathodoluminescent light generation also allows the structure and material to be studied - conventionally in the study of bulk material crystal structure and composition - but also in, for example, the first direct study of plasmon propagation distance [7], detecting quantum light states [73, 87], and the study of phase transitions [58].

Further to my demonstration in Chapter 2 that gold holographic surface-relief plasmonic nanostructures can provide control over the (VIS/NIR) wavelength and wavefront of light emission resulting from the point-injection of medium-energy (30 keV) electrons into the surface [88], I will demonstrate a new concept of a metamaterial-based free-electron-driven light source with controllable direction of emission. I take advantage here of the compact nature and solid-state operation of sources of this kind, and the fact that an electron beam may be switched rapidly (in arbitrary, programmable sequence) among target points, to realize a metamaterial pattern array of surface-relief holographic plasmonic segments, illustrated in figure 3.1, each of which is tailored to steer transition radiation of the electrons impinging into the segment into a collimated beam of light in the prescribed direction.

To quantify the device, I demonstrate low crosstalk between adjacent (or even overlapping) holographic sources. I demonstrate the concept of on-demand light switching with a 6-way directional-division multiplexed light source driven by a 30 keV electron beam of a scanning electron microscope. I further show that the output beams of individual sources can be continuously steered within a certain angular range via fine positional adjustments of the electron beam injection point.

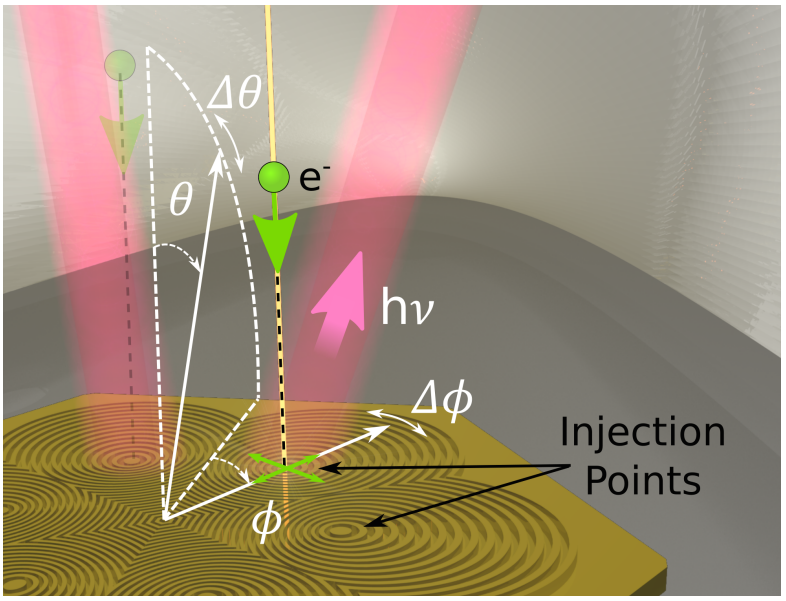

FIGURE 3.1: Artistic impression of multiplexed array of free-electron holographic light sources, each engineered to emit light of a chosen wavelength and wavefront profile in particular polar (θ) and azimuthal (ϕ) directions. The direction of light emission from the ensemble is thereby actively controlled by selectively targeting individual sources with a scanning electron beam pump, and fine-tuned ($\pm$ $\Delta\theta$, $\Delta\phi$ as much as 15°) for each source via nanometer-scale variations in the electron injection position around the target point.

3.2 On-Demand Directional Control of EIRE

Spatially reconfigurable light sources can be generated with a wide range of technologies, and have many applications in science and technology fields. Spatial light modulators are commonly used in commercial, industrial, and research applications to control the profile of light using either optical or electronic driving mechanisms. In addition, recent developments in exploiting the balance of forces at the nanoscale offer the opportunity to develop a new generation of spatially reconfigurable light sources using metamaterials [5] that can also be driven by either optical or electronic means. These reconfigurable nanomechanical metamaterials offer compact, silicon-fabrication-technology-compatible, switchable, and nonlinear function capable of surpassing that of natural media by orders of magnitude.

Numerous applications, such as image display or projection, automated range-finding and tracking, machine reading, laser-based manufacturing, and spectroscopic screening (e.g. remote trace-chemical detection) require modulation or continuous tuning of light beam propagation, or indeed emission, direction, intensity profile and divergence. These are currently served by systems ranging from macroscopic electro-mechanical gimbal and

galvanometer mirror or prism scanners to microscopically-pixelated spatial light modulators based on liquid-crystals and digital micro-mirrors. With improved understanding of near-field light/matter interactions, applications and opportunities now extend to the nanoscale, where optical wavefronts may be manipulated by structural design at the sub-wavelength scale. In particular regard to the control of light emission, it has been shown for example, that plasmonic grating structures can modify the output characteristics of semiconductor lasers, waveguides, subwavlength apertures, thermal and quantum emitters; and that nano-antennas, nano-undulators, and metasurface resonator ensembles can couple medium-energy free-electron excitations to well-defined free-space light modes.

3.2.1 Beam-Steering Devices

Typical commercial spatial light modulators are used for projector displays and usually employ mechanically actuated micromirror arrays or liquid crystals - either ferroelectric or nematic (controlled birefringence effect). The bulk of modern display projectors use micromirror arrays to process light digitally, a technology first developed in 1987 by Texas Instruments [89]. The structure and use of a typical digital micromirror device (DMD) is illustrated in figure 3.2. Each electronically actuated mirror in the array is typically on the scale of tens of μm, the array can be fabricated in several CMOS-compatible lithography steps [90], and can be designed with broadband response (typically from 400 nm to 2.7 μm. However, the mechanical actuation involved limits the switching speed of the array to about 20 μs, making the design unsuitable for some high-speed applications. In addition, the change in direction applied to light by the bi-stable mirror is typically in the range of about 10°. Apart from commercial displays, DMDs are commonly used for lithography, including stereo lithography of complex 3-dimensional structures [91], telecoms switching, holographic data storage, and pulse shaping [92]. For longer wavelength, the mirror arrays can also be used as time-variable diffractive gratings with spectroscopic applications [93]. Similar arrangements of arrays mechanically-actuated optical elements include magneto-optic spatial light modulators (SLM), in which layers of magnetic material are bonded at certain point. This bonding, combined with the magnetic forces, creates periodic gaps between the material layers which can be electromagnetically manipulated [94].

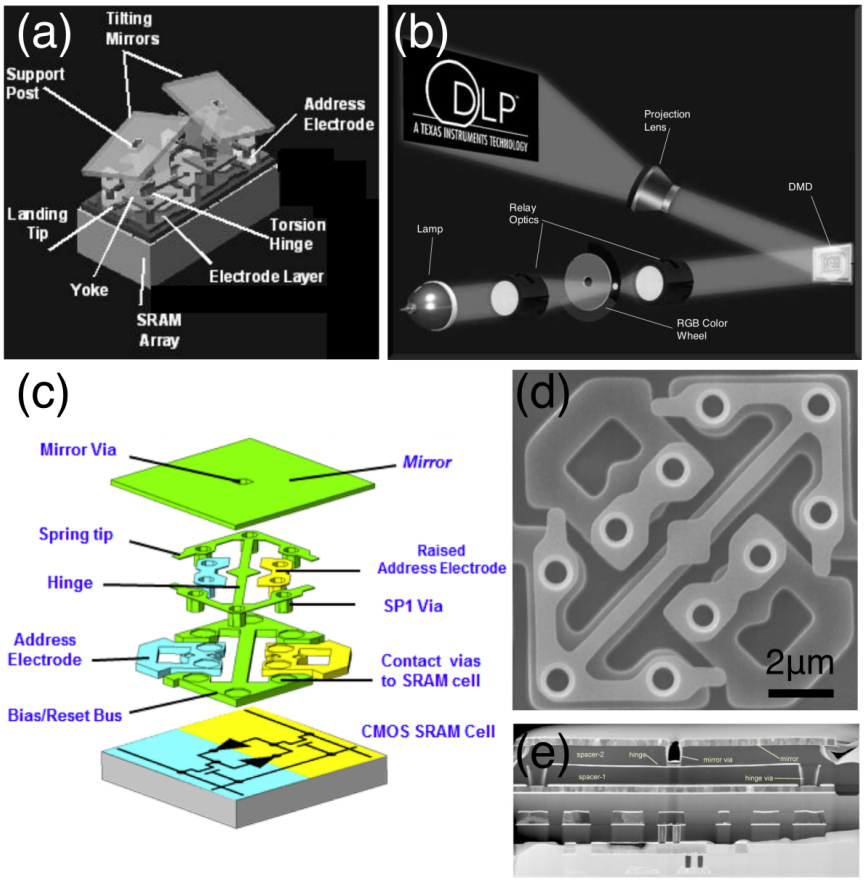

FIGURE 3.2: DMD spatial light modulator structure. (a) Schematic of two DMD mirror-pixels in opposite switched positions. (b) A reflection-type spatial light modulator setup using an on-chip DMD. (c) Exploded view of DMD architecture with three metal layers on top of the controlling static memory (SRAM) controlling cell. (d) Top (mirror removed) and (e) section SEM images of micromirror mechanism after all fabrication steps. (a, b) from [89], (c-e) from [90].

One drawback of DMD-type SLMs is that they are electronically-controlled, making them unsuitable for all-optical signal processing networks about which much recent research has been performed, and are diffraction limited. Recently, a number of nanoscale micromechanical metamaterials have been developed which can be actuated electronically or optically and can rely on a wide range of physical actions including Coulomb, Lorentz, and Ampere forces [5]. These optical switches operating beyond the diffraction limit, some of which are illustrated in figure 3.3, are constrained more by their electromagnetic properties at smaller dimensions, than by their mechanical properties, allowing for faster potential switching speeds. The possibility for a high-speed, optically actuated spatial modulator allows for development of all-optical signal processing networks, potentially realised at nanometre scale.

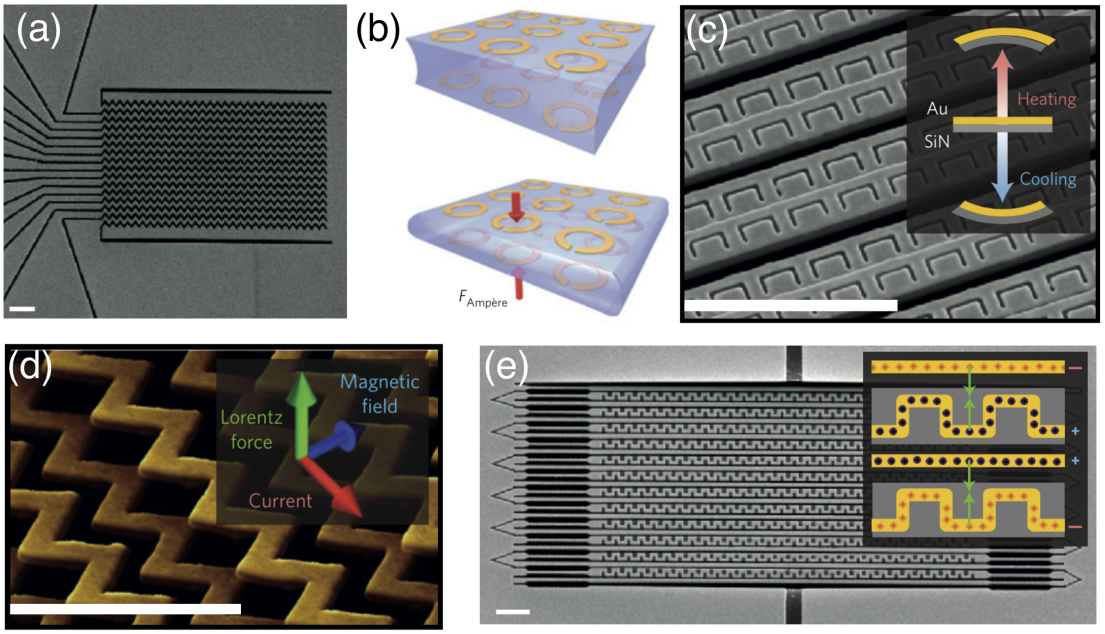

FIGURE 3.3: Implementations of nanomechanical metamaterials for random-access spatial light modulation. (a) Electronically-driven metadevice randomly reconfigurable in one dimension from [95]. (b) Schematic of a magnetoelastic metamaterial device of variable thickness from [96]. (c) Reconfigurable metamaterial driven by thermal expansion from [97]. (d) Magneto-optic spatial light modulator actuated by Lorentz force from [98]. (e) An electro-optic modulator driven by electrostatic forces from [99].

Prior to the widespread use of DMD devices in commercial projectors, many display applications relied on liquid-crystal designs. Today, most modern technological developments rely on using either ferromagnatic or nematic (birefringence-based) liquid crystals for specialty applications such as compressive sensing [100], optical processing [101–103], pulse shaping [104], and wavefront correction [105]. One advantage of liquid crystal matrices for light modulation is that they can readily be combined with enhancement structures such as metamaterials [100, 102, 103] as shown in figure 3.4.

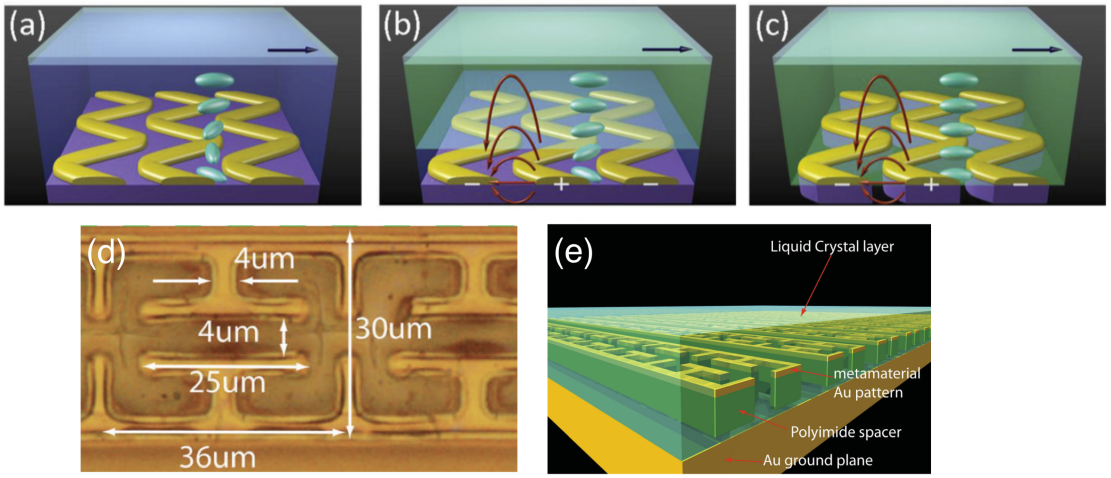

FIGURE 3.4: Examples of metamaterial-embedded liquid crystal spatial light modulators. (a-c) Schematic impression of a hybrid liquid-crystal cell of a spatial light modulator with nanostructured metasurface. (a) OFF state of the cell with twisted ordering in the bulk of the liquid crystal. (b) ON state of the cell: LC ordering has been aligned to planar (green) by electric potential across the nanowires except for a very thin layer at the bottom (blue) with residual twist due to strong surface anchoring. (c) ON state of the cell with suspended metasurface: switching from twisted to planar state is complete both in the bulk and in the plane of the metasurface. (d) Microscope image of unit cells of metamaterial and (e) schematic representation of terahertz spatial light modulator composed of metamaterial absorber layer coated with electronically-controlled liquid crystals. (a-c) from [103], (d, e) from [100].

Despite the wide array of applications for which these light-manipulating devices, all of them are dependent on some kind of movement - the translation or rotation of a physical component of the structure. Despite the fact that this imposes some inherent restrictions on the response speed of the devices, the alternative, solid-state spatial light modulators, have been rare and difficult to implement. One solid-state implementation used arrays of quantum wells [106], driven by an electrical-wire grid interface to create absorption change in a reflection-type device. While novel, the implementation did not achieve a greater contrast ratio or faster switching time (on the order of 50-100 μs) than comparable designs using liquid crystal or DMD technologies.

In this chapter, I will descibe a system of using the previously illustrated holographic free-electron driven light sources as an electron-beam driven light modulation source. The device, having no mechanically-driven components, is limited in its switching to the electron-beam directing mechanism used, the fundamental driving mechanism of plasmonic propagation on a metallic interface occurring on a picosecond time scale.

3.2.2 Directionally-Switchable Free-Electron Light Source: First Prototypes

When collecting the light from a multipoint source with a parabolic mirror, the device operates under an additional constraint that all emission must originate close to the focal point of the mirror. In implementing a directionally-selective pixel design, this constraint does not necessarily apply since the light collection optics can be altered to suit the application. However, given the experimental platform outlined in Chapter 1, designing a proof-of-concept device required some tailoring of design parameters to suit the collection optics.

Initial tests of positioning individual holographic elements revealed that an output beam from a holographic source of 15 μm radius could be distinguished provided the central excitation point was within an area of approximately 10 μm radius from the focal point of the collection mirror. Thus first designs of an electron driven, directionally selective device focused on spacing the electron-beam injection points within this area. In addition to this size constraint, any functional directionally-selective device must show clear discrimination between the direction of the outputs, and consistency in the brightness of each.

As a first test, a 20 by 20 μm sample was fabricated, composed of a 4 by 4 array of 5 μm square holographic metasurfaces with a milling depth of 60 nm into a layer of 160 nm polycrystalline Au derived from the original holographic electron beam driven metasurface design described Chapter 2, with varying polar emission angle defined by

row R as $\theta = (10 + R * 10)°$and azimuthal emission angle defined by column C as $\phi = (120 - C * 30)°$. The binary design and resulting SEM image of the pattern is shown in 3.5(a-b). Figure 3.5(c) shows the expected area of emission with the sample rotated 30° azimuthally to avoid areas of large inefficiency in the mirror. Figure 3.5(d) shows the resulting polar emission patterns for 800 nm light corresponding to the electron beam focused at the centre of each holographic element, with the centre of the total design at the mirror focus.

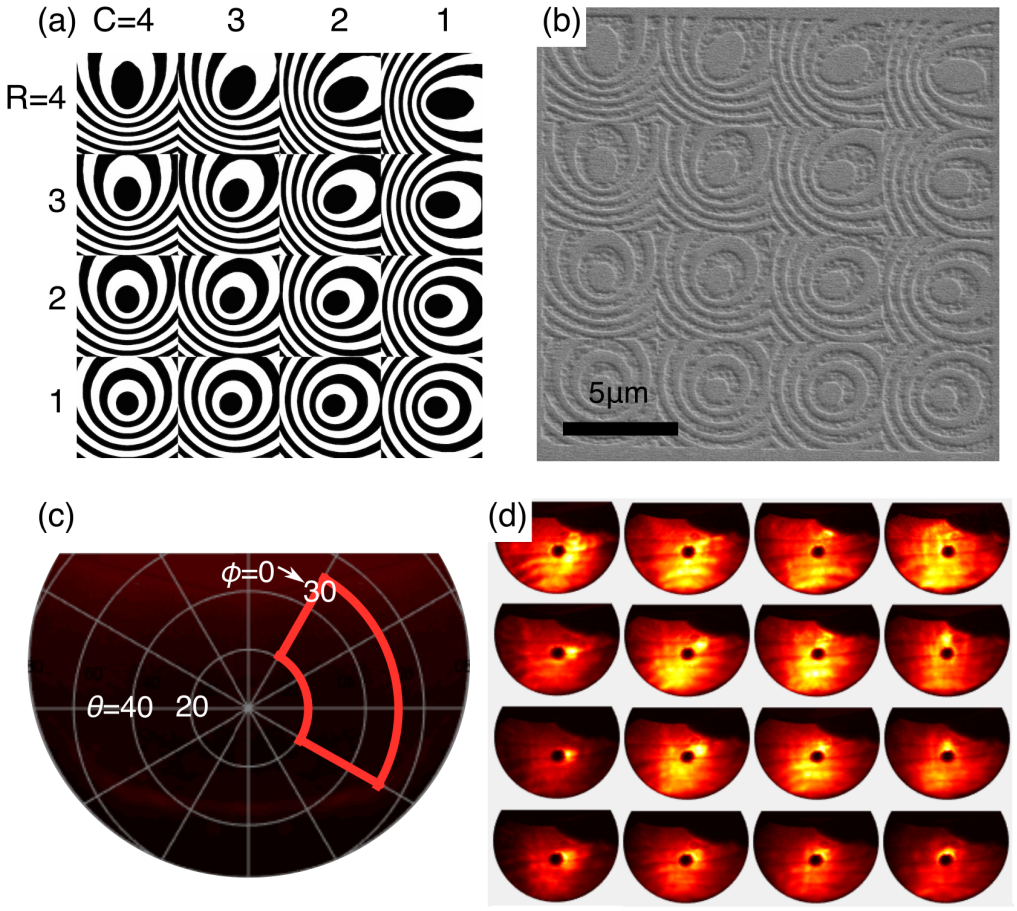

FIGURE 3.5: First prototype of directionally-selective holographic pixel. A 2D rectangular array of 5 μm holographic emitters, with direction of emission (for 800 nm wavelength) distributed evenly across 90 azimuth degrees and 30 polar degrees, as show in (c). (b) shows the SEM image of the sample in polycrystalline Au as fabricated from the holographic binary (a). (d) shows the resulting polar pattern from a 30 keV electron beam centred on each individual emitter.

Even at a distance of ∼15 μm from the mirror focus, image distortion of the polar patterns (shown by change in shape of the semicircle and drift of the mirror hole away from centre) is minimal. However, the individual holographic elements are too small and close together to be able to clearly discriminate between output directions and significant overlap between the output spots occurs. It can be seen from the fact that the central holographic elements generate polar patterns with much higher background illumination surrounding the spot, that crosstalk between adjacent emitters, likely caused by propagating SPP, occurs significantly when the electron beam is incident on these points. Therefore, the emission from the individual elements is not consistent.

In an effort to decrease the beam divergence from a given emitter element, a second 2D, rectangular array, shown in figure 3.6, was fabricated. This spread the design emission angles over a wider polar area, shown in 3.6(c), and increased the size of each holographic sub-pixel to a circular element of 40 μm diameter in an attempt to increase the brightness of each, keeping the same spacing as limited by the mirror optics. Figure 3.6(a) shows this spacing arrangement of the 25 elements, with the diameter of each element reduced to 10 μm to show detail. However, since the individual metasurface elements overlap to a large extent, a high degree of crosstalk is present in the polar emission of this device also, as seen in the summation image shown in 3.6(d).

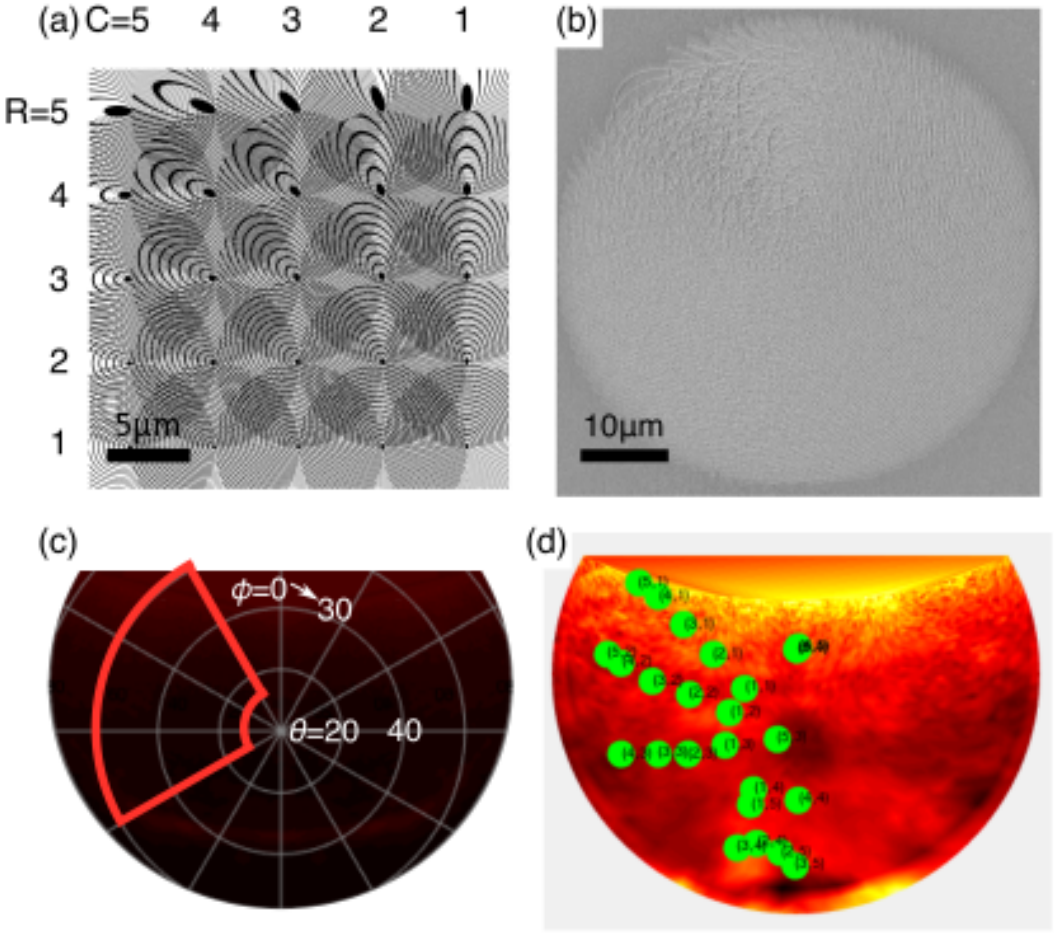

FIGURE 3.6: Second prototype of directionally-selective holographic pixel. A 2D rectangular 5 × 5 array of overlapping 40 μm diameter circular holographic emitters, with direction of emission (for 800 nm wavelength) distributed evenly across 90 azimuth degrees and 40 polar degrees, as show in (c) such that each emitter has equal spacing in the polar transform. (b) shows the SEM image of the sample in polycrystalline Au as fabricated. (a) shows the binary for the same angular distribution and emitter separation, with each individual emitter's diameter reduced to 10 μm to show detail. (d) shows the sum of the resulting polar patterns from a 30 keV electron beam centred on each individual emitter.

Given that each of these designs did not show consistency in the brightness of the output in all the prescribed directions, I present a functional design in section 3.2.5 that uses a radial rather than rectangular array, thus appearing symmetric for each electron beam position. Additionally, to quantify the spacing that could be realistically achieved between adjacent injection points in such a design, I present a test of isolated two-element samples in section 3.2.3. An initial test of two-element samples is shown in figure 3.7. For this proof-of-concept test, I select orthogonal and opposing orientations to test for any difference in light output that varying the angle between overlapping elements might result in. I fabricated a series of these samples with spacings of 0 to 10 μm in 2 μm intervals from the centre of the fabrication area to the excitation point of each hologram design.

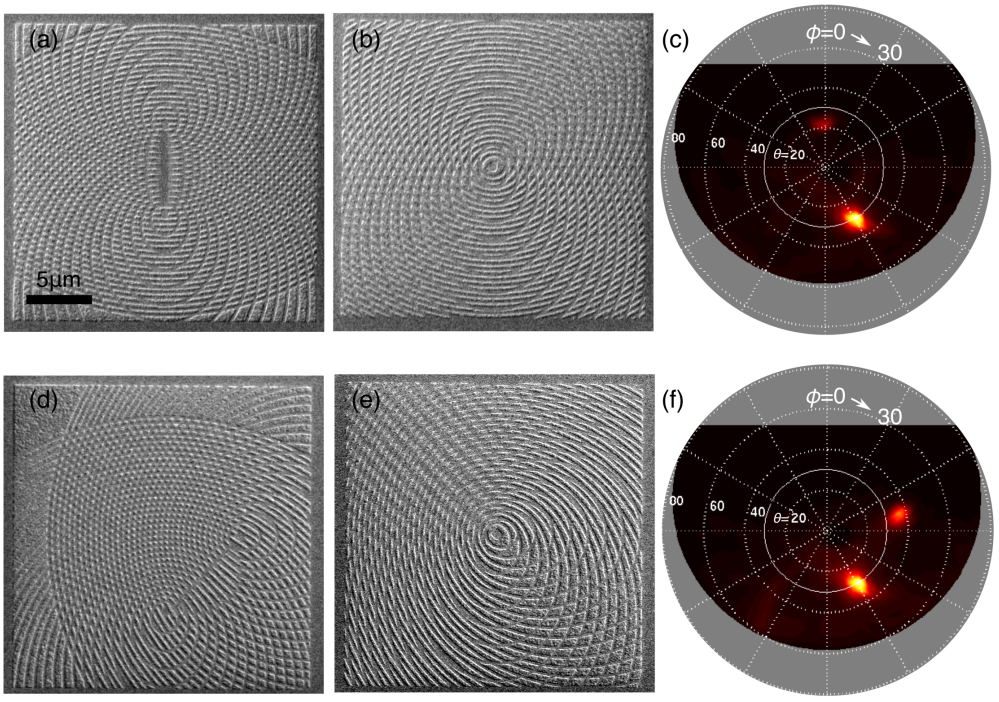

FIGURE 3.7: Prototype of bi-directional samples to quantify holographic element crosstalk. (a, b) SEM images of samples fabricated to characterise cross-talk between elements on opposing azumuthal orientation. Shown here with holographic element spacing of (a) 4 μm and (b) 0 μm from each central excitation point to centre of fabrication area. (c) Polar emission pattern generated from sample shown in (b). (d, e) SEM images of samples fabricated to characterise orthogonally-oriented azimuthal emission cross-talk with spacings of (d) 4 μm and (e) 0μm from each central excitation point to centre of fabrication area. (f) Polar emission pattern generated from sample shown in (e).

Results from this series of dual-emitter samples with overlapping excitation points are shown in figures 3.7(c) and 3.7(f). When testing overlapping samples with no separation between injection points (figure 3.7(b, e)), two emission spots in the correct orientations are observed in the polar plots. However, even at the minimum fabricated spacing between electron injection points (4 μm and 2.8 μm in the opposing and orthogonal configurations, respectively, as shown in figure 3.7 (a) and (d)), a second spot could not be observed. Thus, section 3.2.3 presents a sample series fabricated with a reduced spacing step to quantify cross-talk. In addition, in an effort to maximize the fabrication area available with a square design, each emitter design included less effective area as the spacing between the two emitters increased. Therefore, while this initial design showed proof-of concept for an easily-distinguishable two-element emitter a future design with which inter-element cross-talk could be quantified must include closer spacings and a greater uniformity of holographic elements as the spacings changed.

3.2.3 Cross-Talk Analysis

Having seen the issue of emission cross-talk between closely spaced elements from the previous attempts, the necessity of quantifying the behaviour of two metasurface emitters in isolation at various spacings became apparent. This led to an optimal spacing for minimum cross-talk and acceptable distortion from the offset of the collection mirror focal point. I also observed that small, nm-scale deviations in the position of the electron beam on the central, raised diffractive element of the pattern, resulted in small deviations in the angular output of the generated light beam. This, combined with the switching ability of closely-spaced adjacent holographic sources, allows for the creation of a nanoscale, electron-beam driven light source with continuous, not simply discreet, angular output determined by beam position.

I first created holographic metasurface samples for analysing the crosstalk between pairs of overlapping sources oriented to emit in orthogonal and opposing (figures 3.8 and 3.9 respectively) azimuthal directions. In each case a series of samples was prepared with electron injection target point separations d ranging from zero to 30 μm. Individual emitters were designed (after [88]), for a wavelength $\lambda = 800$ nm, to generate a low-divergence, plane wave output beam at a polar angle $\theta = 30°$. Each comprises 15 offset concentric oval rings around the electron injection target point, as shown in the binary designs (figures 3.8 and 3.9(a)) and the experimental sample images inset to the respective figures. Samples were manufactured by focused ion beam milling in binary surface relief (etch depth 60 nm) on an optically thick (140 nm) polycrystalline gold film. Spatial distributions of electron-induced light emission from these sources were probed in a scanning electron microscope (SEM; operating in fixed-spot mode at an electron

energy of 30 keV and beam current of 11.4 nA; with a focal spot beam diameter 50 nm) configured with a confocal parabolic mirror to project emitted light onto a (800 ± 40 nm bandpass filtered) nitrogen-cooled imaging CCD array. From the Cartesian CCD plane, angle-resolved (spherical) maps of emission intensity are then obtained via a coordinate transformation accounting for the curvature of the mirror surface.

Regardless of their mutual orientation, when the two sources share a common injection point ($d = 0$) light is emitted equally (instrumental uncertainties aside) into both output beams, as one would expect. With the electron beam then fixed on one of the two injection points in each source pair, parasitic emission from the secondary source decreases sharply as d increases being attenuated for both mutual orientations by a factor $1/e$ at separations $d < 2$ μm and by an order of magnitude for separations $d \geq 6$ μm. This is in spite of the fact that the exponential surface plasmon propagation decay length for a (planar, unstructured polycrystalline) gold/vacuum interface at 800 nm is $\sim$25 μm [12, 81], because regardless to the strength of the reference field its wavevector distribution is almost entirely unsuitable for holographic reconstruction of the intended output beam from a positionally offset secondary mask. In other words, while the electron-induced field still interacts with the scattering elements of an offset mask, the conditions of constructive/destructive far-field interference that produce a well-defined, directional output beam are broken.

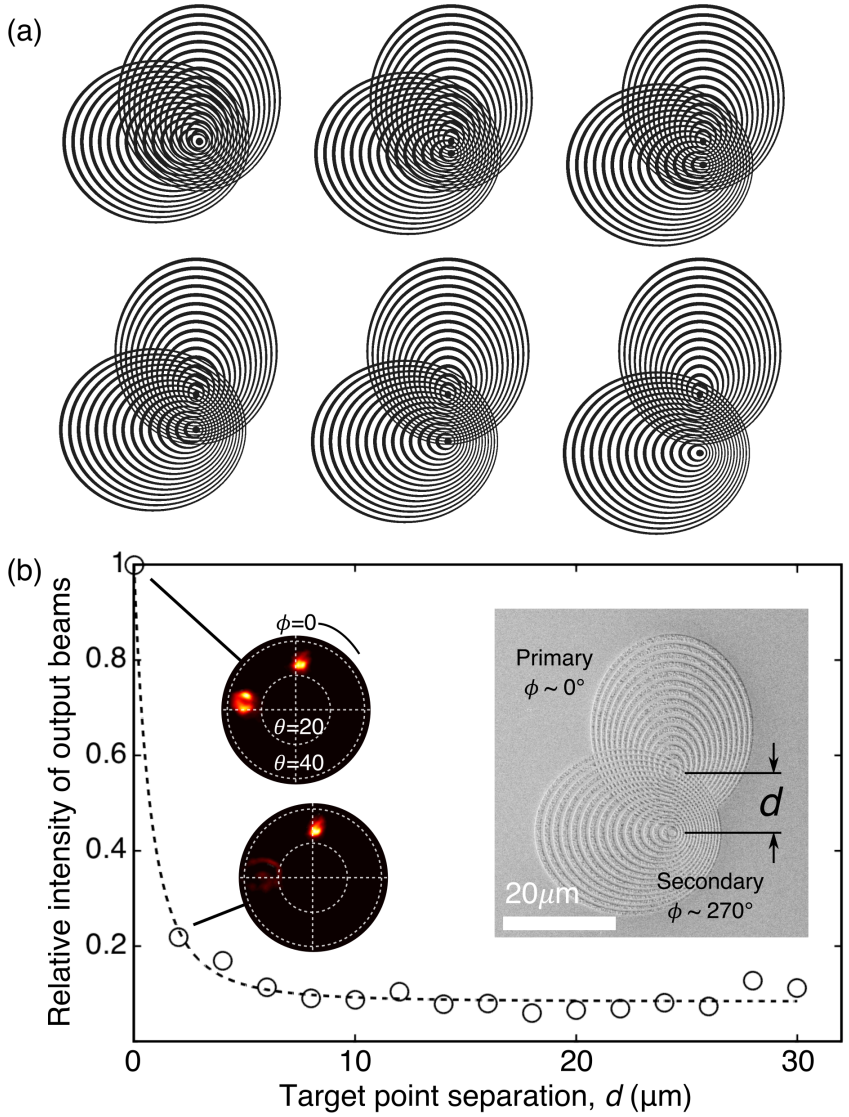

FIGURE 3.8: Relative magnitude of parasitic emission from a secondary source as a function of the separation d between its intended excitation point and the targeted electron beam injection point of the primary source for pairs of holographic sources configured to emit collimated beams at the same 800 nm wavelength and $\theta = 30°$ polar angle and orthogonal azimuthal angles. In each case the separation d is varied in 2 μm steps over a series of otherwise identical samples on the same gold film; (a) Shows sample designs for first 6 separation steps (d = 0 to 10 μm). (b) Intensity measured as the ratio of average photon counts for those pixels greater than half the maximum pixel count (average -3 dB pixel), collected by the mirror within $\phi = \pm 30°$ of the two design emission directions, normalized by the ratio of the average -3 dB pixels at $d = 0$ μm separation. Inset shows scanning electron microscope image of example sample and angular distributions of 800 $\pm$ 20 nm light emission for d = 0 and 2 μm.

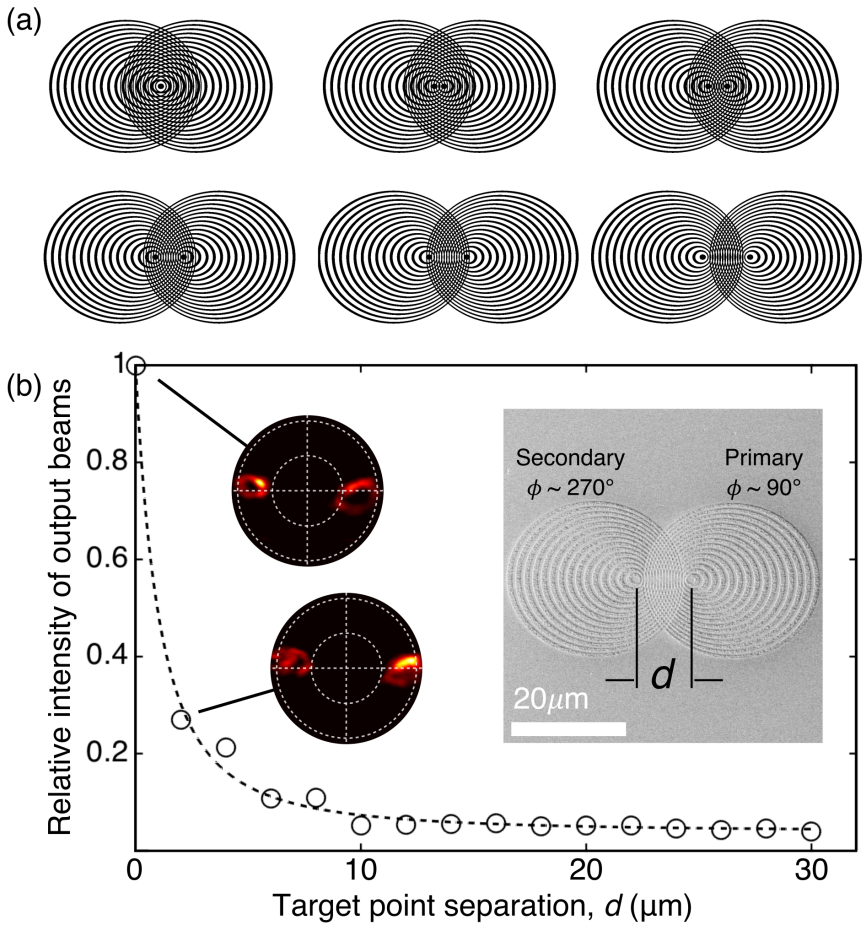

FIGURE 3.9: Relative magnitude of parasitic emission from a secondary source as a function of the separation d between its intended excitation point and the targeted electron beam injection point of the primary source for pairs of holographic sources configured to emit collimated beams at the same 800 nm wavelength and $\theta = 30°$ polar angle and opposing azimuthal angles. (a) Shows sample designs for first 6 separation steps ($d = 0$ to 10 μm). (b) Intensity measured as described in figure 3.8. Inset shows scanning electron microscope image of example sample and angular distributions of 800 $\pm$ 20 nm light emission for $d = 0$ and 2 μm.

3.2.4 Continuous Beam-Steering With Single Holographic Source

While the crosstalk between closely spaced holographic emitters is limited by this constructive interference condition breaking, this condition is not broken instantaneously: in keeping with the behaviour observed for electron-induced light emission from single plasmonic nanodisks [36], whereby the azimuthal distribution of emission can be tuned by adjusting the position of electron injection on the top surface, here small displacements of the electron injection point within the ellipsoidal central domain of a single holographic source can be employed to steer the output beam, as illustrated in figure 3.10.

To demonstrate this, I fabricated individual sources of the type used for cross-talk analysis, allowing the beam to be swept within the central region of the metasurface without a secondary output. For a single holographic source of the design shown in figure 3.9, polar and azimuthal output angles can be tuned by up to $+7$ / $-2°$ and $\pm$ 15° respectively, by displacing the electron injection point in directions parallel and perpendicular respectively to the in-plane mirror symmetry axis of the holographic mask. (To a first approximation, θ is not expected to depend on x displacement of the electron beam, nor ϕ on y displacement. The deviations from zero in these data are indicative of instrumental and sample alignment inaccuracies, notably imperfect tip/tilt orientation of the parabolic mirror as discussed in Ref. [88], and imperfect rotational alignment of the samples symmetry axis, i.e. the $\phi = 0$ direction, with that of the mirror.) As may be expected, emission intensity is reduced as the electron beam deviates from the intended injection point (see insets to figure 3.10(a) and (b)), though interestingly only by $\sim$13% when the beam is displaced parallel to the symmetry axis of the holographic structure, even at the edges of the central disk; the intensity drop-off is much sharper for orthogonal symmetry breaking pump beam displacements, with a loss of $\sim$75% of intensity at the edges of the disc.

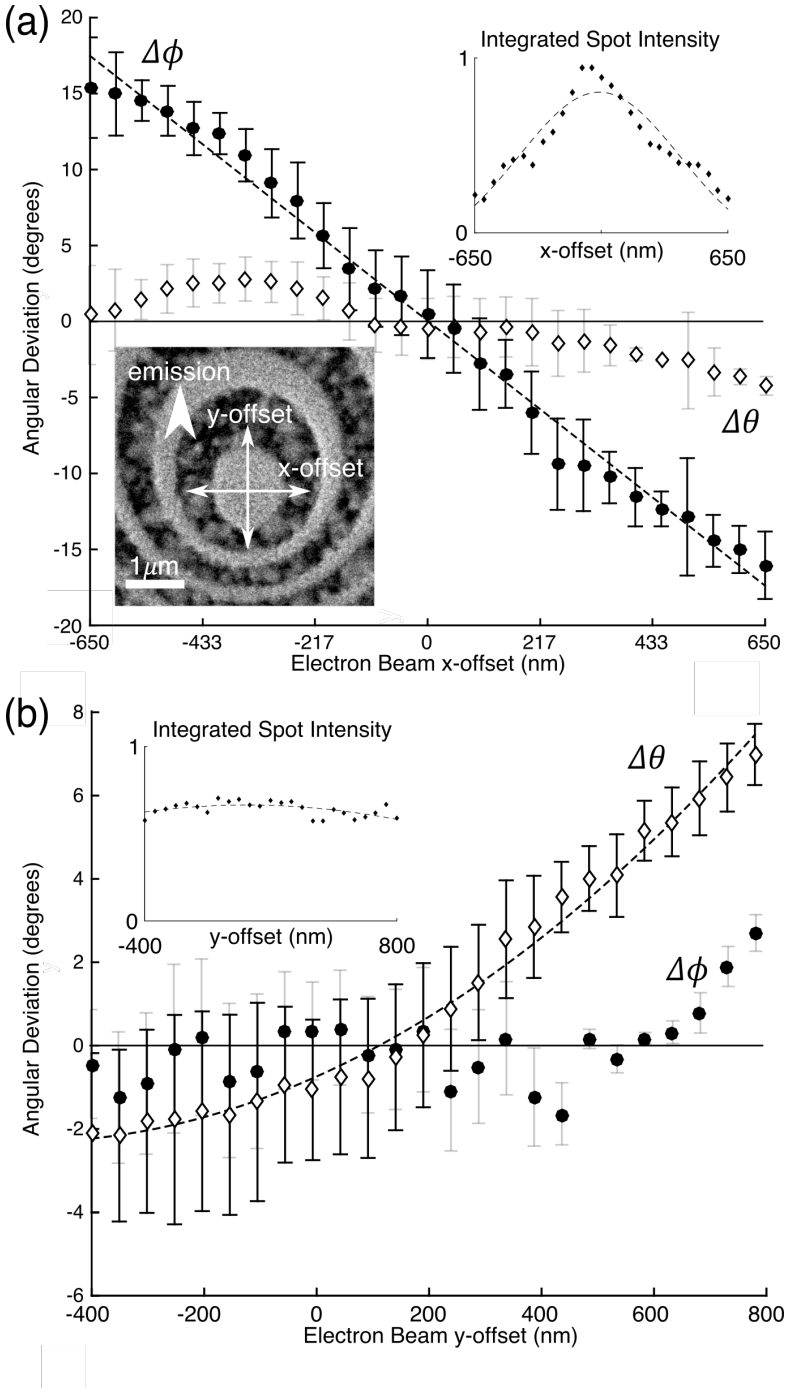

FIGURE 3.10: Steering the output beam of a single holographic source. Changes, $\Delta\theta$ and $\Delta\phi$ respectively, in polar and azimuthal light emission angles as functions of electron injection point displacements within the central disc of a single holographic source (a) perpendicular and (b) parallel to its mirror symmetry axis [in the x and y directions as defined in the scanning electron microscope image inset to panel (a)]. Injection point displacements are measured relative to the target point intended by holographic design [not the geometric centre of the disc]; changes in output angle are measured relative to the direction of the corresponding output beam. The insets show normalized emission intensity integrated over the -3 dB spot area as a function of x/y offset.

3.2.5 Switchable Multi-Element Light Source

By virtue of their inherent reliance upon highly-localized excitation (i.e. inherently low crosstalk), several independent (even identical) holographic sources can be integrated over a relatively small surface area, such that a scanning electron beam may selectively address individual emitters in any sequence (with individually tailored pump parameters of beam current, electron energy and dwell time) to rapidly modulate the optical output signal over a half-spherical field of view. While in the previous section, overlapping holographic emitters were shown to provide good discrimination with output beams, an overlapping design becomes less appropriate with an increasing number of multiple emitters. As shown in figure 3.6, the fabrication process requires an increasing level of detail over a large area for many overlapping sources. Thus, truncated holographic sources were used in a hexagonal arrangement to test a multiple emitting, switchable device. In addition, a balance must be struck between the density of integration and the detrimental effect of truncating individual sources (in the present case to wedge-shaped domains comprising less than half of the area of a corresponding circular holographic source) on emission brightness and sharpness (c.f. beam divergence) of the output beams.

Figure 3.11 shows a hexagonal array of six identical sources (designed for $\lambda = 800$ nm emission at $\theta = 30°$) azimuthally oriented at 60° intervals, with a separation between nearest-neighbour electron injection target points of 16 μm. Here, clear discrimination among outputs is retained, with emission intensity in the mid-point azimuthal direction between two equally pumped neighbouring sources being at least 50% lower than in the designed beam directions, as shown by the inset to 3.11(b) at 50% dwell time. In this demonstration, for the purposes of producing a still image, the electron beam is switched (within ~5 ms) from the injection point of one source to that of the other halfway through the 20 s integration time of the CCD. Depending on application though, one may switch back and forth between two sources (or among many sources), to maintain desired levels of relative time-averaged brightness, at a frequency limited only by the electron beam control and positioning system. (Though it should be noted that as switching frequency increases, i.e. as the electron beam spends a greater proportion of time between target injection points, total brightness will decrease and, unless the beam is blanked at each switching interval, noise will increase.)

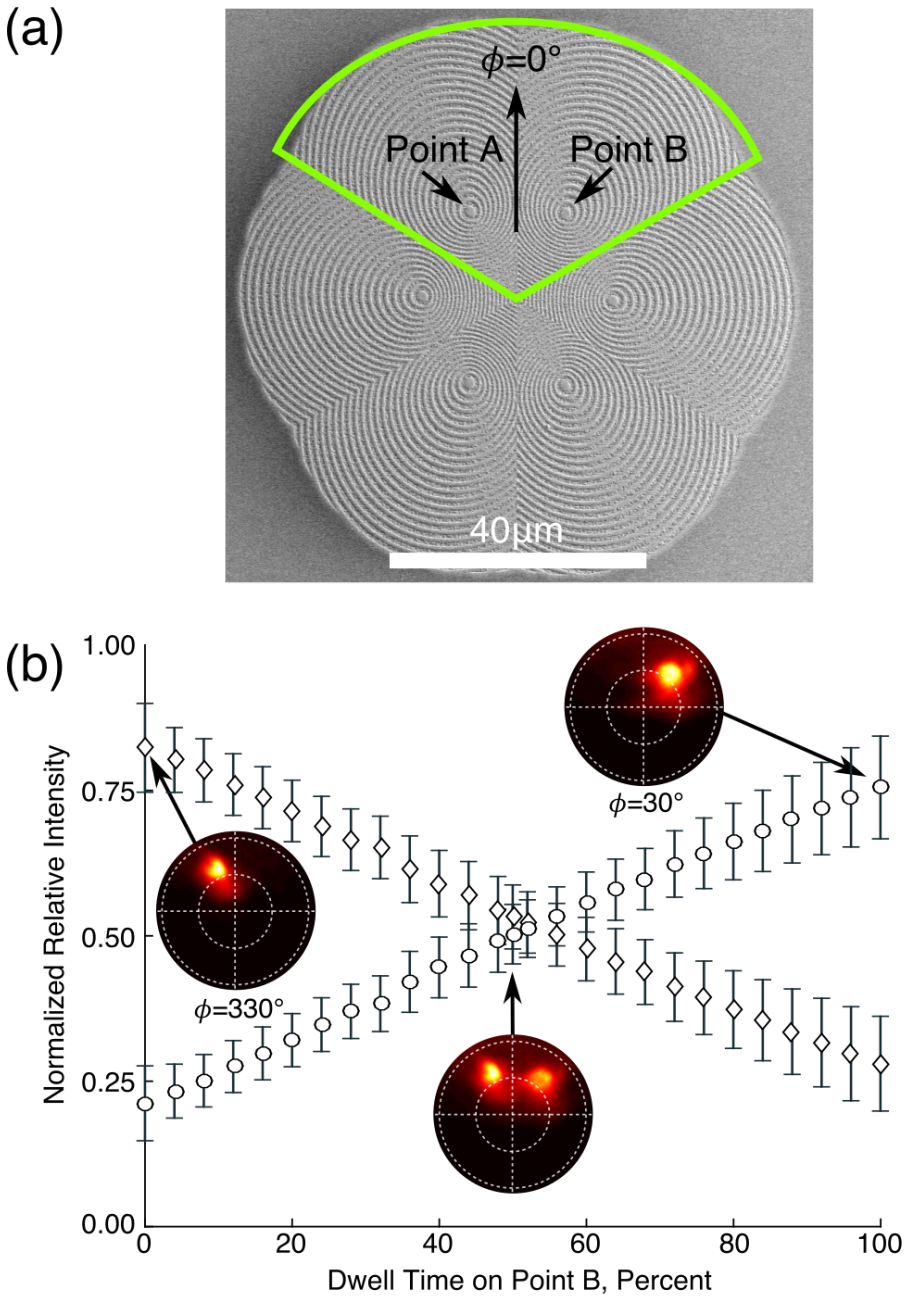

FIGURE 3.11: (a) SEM image of demonstration sample of azimuthally multiplexed hologram emitter, and (b) relative intensity of emission in two as electron beam excitation is switched between two holographic directions elements.

3.3 Conclusion

In summary, we have demonstrated experimentally that holographic free-electron-driven light sources can be assembled in close-packed multiplexed arrays, with minimal crosstalk between adjacent elements. These can be programmably addressed, taking advantage of the highly-localized and positionally-agile nature of a focused electron-beam pump, to generate arbitrary patterns of light emission.

The demonstration here uses the single electron source of an SEM system to scan amongst multiple sub-elements and generate light, each of which is designed to generate a directional near-infrared plane-wave output beam. This is analogous to a single 'pixel' of a light-generating display, but with each sub-element designed to generate a directional near-infrared plane-wave output beam.

But neither of these aspects represents a constraint on application: indeed, it has been shown in Chapter 2 that holographic surface-relief structures can be engineered to produce complex wavefronts such as high-order vortex beams; and in the context of flat-panel field-emission and surface-conduction electron-emitter display (FED, SED) technologies, large addressable arrays of microscopic ballistic electron sources operating at acceleration voltages greater than 10 keV are well-known [107]. The possibility of creating optical vortices generated in a randomly-addressable fashion could be useful in light-matter interactions such as optical tweezers and high-throughput chirality detection. One may thus envisage a chip-scale, dynamically programmable array of holographic light sources, designed to emit a range of wavelengths and wavefront profiles in a range of polar and azimuthal directions, each pumped by a dedicated electron source.

The fastest switching time presented here (5 ms) is much slower than what may be ultimately achievable, indeed advances in ultrafast electron-beam sources [108] provide an intriguing compliment to such a directional-selective device. Moreover, on the basis that the output beam direction for individual holographic light sources varies continuously with electron pump beam position on the central disk, such structures may be engaged as sensors of electron (or more generally, charged particle) beam pointing stability, with nanometric injection point displacements manifested as output light beam displacements on a positon-sensitive photodetector. Such an application is of great interest to the particle physics community as a means of non-invasive analysis for the fine positioning of charged-particle beams [109].

Chapter 4

All-Dielectric Free-Electron-Driven Holographic Light Sources

4.1 Introduction

I have shown in previous chapters that the excitation created by a ballistic electron beam impacting a plasmonic material can be controlled with holographically designed surface-relief structures to generate on-demand light output. Recent publications concerning photonic metasurfaces have shown that the range of materials available to create these structures includes dielectrics and semiconductors [40, 110, 111], as well as conventional plasmonic platforms, expanding the applications that can be tailored to. Here, I apply the concept of holographic control to manipulation of the spatial distribution of transition radiation emission of a given wavelength from high-refractive index dielectric and semiconductor target materials. I will show accordingly that incoherent luminescent emission at the prescribed wavelength is unperturbed by holographic surface-relief structures and thereby derive a means of discriminating between the emission components and providing wavefront control over electron-beam generated transition radiation.

4.2 Holographic Control of EIRE From Semiconductors and Dielectrics

As shown in section 1.3, imaging and spectroscopic analysis of cathodoluminescent emission - the light generated by the impact of free electrons on a material, are long-established techniques in electron microscopy, where they form part of the analytical toolkit for identifying dopants in semiconductors [112, 113], geological features such as fractures and stress regions [114], or crystal interfaces [115–117]. The availability of these characterization techniques and parallel advances in nanofabrication technologies have led to growing interest in frequency-tuneable free-electron-driven nanoscale light sources such as plasmonic nanoantennas [26, 37] and metasurfaces [38]. As discussed in Chapter 1, electron excitations have facilitated the probing of these structures [7, 8], and a range of hyperspectral electron-induced radiation emission (EIRE) imaging techniques have been developed for the study of surface plasmon polariton propagation [12, 81], the mapping of optical density of states [17, 69], and the identification of structural phase states [118, 119]. As shown in Chapter 2, holographic surface-relief plasmonic sources can provide control, by design, over the wavelength and wavefront of light emission resulting from the point-injection of medium-energy electrons into a gold surface.

The use of cathodoluminescence (CL), the light generated from a medium energy electron beam impacting a material, as an analysis tool in scanning electron microscopes (SEM), dates to some of the very first applications of the device [120, 121]. This type of excitation is particularly useful because it can be broad-band and generated from a very small surface area or volume. The analysis of CL emission can be quite complex as there are several material-dependent mechanisms by which light may be generated as the result of electrons impacting a surface, and may be in varying proportions depending on electron beam parameters. In general, the emission processes are separated into coherent and incoherent categories. Coherent processes, such as surface plasmon polariton (SPP) excitation, and Cherenkov and transition radiation (TR), occur nearly instantaneously, from an interaction volume of sub-wavelength dimensions (effectively within the near field of the electron). Incoherent processes, such as direct and indirect carrier recombination, occur over time, often decaying gradually as the electron scatters within a relatively large interaction volume within the material.

As discussed in Chapter 1, an electron crossing the boundary between two different materials releases energy proportional to the Lorentz factor of the particle in the form of TR [6] with spectral and spatial distributions and an intensity determined by the difference between the relative permittivities (c.f. refractive indices) of the two materials.

As the electron reaches the interface, this can be thought of simplistically as two counter-propagating charges, the electron and an induced charge in the material, reducing to a dipole-like oscillation when considering a single frequency only. While this emission pattern can be calculated analytically, it is straightforward to derive the amplitude and phase in a discreet three-dimensional spatial region where the light from this process can be simply but accurately modelled by considering an emitting dipole very close to the material surface. This model takes into account only the near-instantaneous processes at the interface, and the far-field calculation will therefore exclude any radiation that would arise in a material from Cherenkov, incoherent, or, in the absence of nearfield-scattering structure, SPPs. The characteristic cross-sectional polar emission shape of TR is shown in figure 4.1(b), being very similar to recorded patterns.

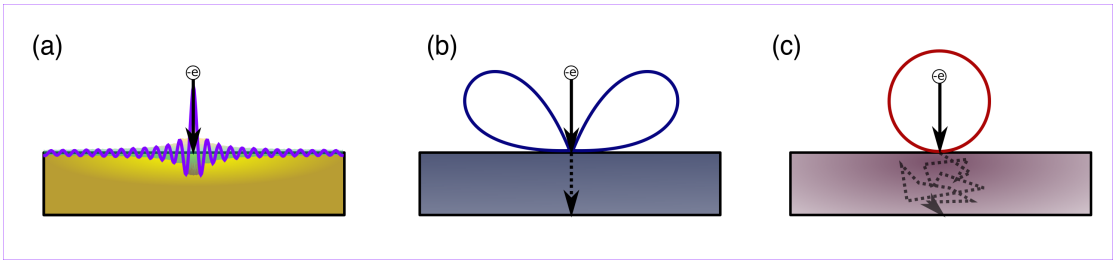

FIGURE 4.1: Schematic representations of surface excitation modes in CL; (a) Non-emitting SPP propagation in metals. (b) Dipole-like polar emission cross-section of TR. (c) Lambertian-like emission from the interaction volume of an inelastically scattering electron.

Incoherent processes such as direct and indirect carrier recombination dominate the emission of many semiconductors and dielectrics. These occur over time, often decaying gradually as electrons scatter many times within a relatively large interaction volume beneath the surface of a material, and can be spectrally sensitive to factors including temperature, strain, dopants/impurities, lattice defects, a quantum/structural resonances [112, 116, 122–124]. This large interaction volume results in distributed illumination and a Lambertian-like polar emission profile shown in figure 4.1(c) as distinct from the dipole-like emission of TR. These coherent and incoherent EIRE mechanisms rarely manifest in isolation though and their contributions are not readily disentangled in measurements of electron-induced light emission [81].

For example, in the case of the gold holographic light sources described in Chapter 2, the 30 keV electron excitation is coupled to a combination of SPPs (approximately 64% of energy) and TR (approximately 36% of energy) with an expected photons-per-electron efficiency ratio [73] of approximately 3:2 at the experimental wavelength of 800 nm. It is seen that holographic metasurface structures can very effectively convert these divergent emissions emanating from the electron impact point into light beams with selected wavefronts, specifically directional plane waves and high-order optical vortex

beams. However, the holographic design process does not distinguish between the TR and SPP components of the excitation (both are part of the same singular reference electric field distribution) and measurements do not discern the relative efficiency with which the two components of emission are coupled to the desired output beam.

Methods of separating each light emission process for analysis is a field of ongoing, current research with valuable applications in instrumentation and materials engineering [29, 74]. Although determining which light generating processes are prevalent in any particular material is far from a trivial task, doing so provides a wealth of analysis information. CL analysis can reveal information about varying material properties tens of microns beneath the surface, about carrier behavior at structural interfaces, and about phase transitions [113]. Time-resolved CL also provides a powerful tool for analyzing carrier lifetime in a wide array of materials [125].

4.2.1 Semiconductor and Dielectric Structured Light Sources

While plasmonic metals are ideal for generating coherent excitations from ballistic electron beams, there are many applications for which the use of a metallic device presents a number of problems. The generation of plasmonic excitations in metals, whether by electron beam or optically, creates ohmic losses that dissipate largely into heat. Particularly in the case of electron-beam excitation, this heat can be highly localised and easily cause structural damage in metal layers or layer interfaces, as seen in section 2.2. In addition, plasmonic metals are generally not compatible with current CMOS fabrication facilities in which the presence of metal dopants must be strictly controlled.

Hence, there has recently been increased interest in developing metamaterials, metasurfaces, and flat optics that rely on dielectrics and semiconductors, some of which are illustrated in figure 4.2. In general, these structures have functionality based on charge displacement resonances rather than conductor current modes, as plasmonic structures do [40, 42, 126]. Traditionally, such a function can be applied to a beam of light as it propagates, as in a bulk lens or polarizer. However, dielectric metasurfaces rely on abrupt refractive phase shifts spread across a large 2D area to apply the same function. To determine the phase shifts necessary to replicate an optical device, the mathematics of transformation optics is usually applied [127, 128]. For example, a dielectric metasurface 'carpet cloak' has been demonstrated that uses a transformed coordinate space to give the same function as a flat mirror to surface bump, thus masking it over the wavelength range of 1.4-1.8 μm [57]. Dielectric flat optics based on metasurfaces also have, as do their plasmonic counterparts, the advantage of being able to combine several optical functions into a single device. Hence, example applications have been demonstrated

with combined polarizer-beamsplitters [129] and polarizer-focusers [130] implemented in dielectric media. Additional applications have included optical vortex generation [110], including with relatively low refractive index materials. [131]

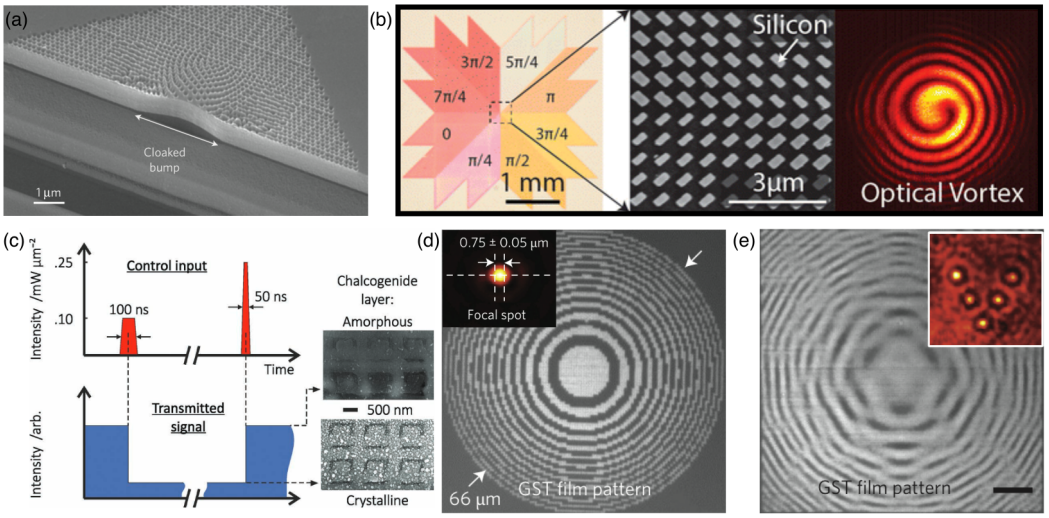

FIGURE 4.2: (a) Scanning electron microscope image of a carpet cloak fabricated on silicon-on-insulator wafer for transforming a mirror with a bump into a virtually flat mirror. From [57]. (b) Metasurface silicon reflect array showing abrupt phase-shift imparted in each region of a radial design and SEM image detail of central region as fabricated, and interference pattern resulting optical vortex beam with counter-propagating gaussian beam. From [110]. (c) All-optical, non-volatile, chalcogenide glass metamaterial switch: metamaterial unit cells in chalcogenide layer which is homogenously switched between amorphous and crystalline states (insets: SEM images of metamaterial units in the phase states). From [59]. (d-e) On-demand binary and greyscale devices optically written in phase-change film. (d) Fresnel zone-plate pattern imaged at $\lambda = 633$ nm Inset: microscope image of the optical hotspot as focused by the Fresnel zone-plate at $\lambda = 730$ nm. (e) Image of eight-level greyscale hologram designed to generate a V-shaped five-spot pattern. Scale bar: 5 μm. Inset: microscope image of the generated five-spot pattern in transmission mode. From [132].

In the optical domain, specifically silicon and chalcogenide glasses have emerged as well-established materials for developing all-dielectric metasurfaces. The chalcogenides compounds containing at least one of the chalcogen (periodic table group 16) elements sulphur, selenium or tellurium are a unique material family, offering composition-dependent high-index dielectric, IR-transparent, optically nonlinear, plasmonic, and topological insulator properties. They are perhaps best known as phase-change media: alloys such as Ge:Sb:Te (GST) can be switched in non-volatile fashion by external (optical or electronic) stimuli between solid amorphous and crystalline states having markedly different refractive indices and conductivities, upon which basis they are the foundation of rewritable optical data storage technologies (i.e. CD, DVD and Blu-ray discs). The properties of nonlinearity, photosensitivity, low phonon energy also make chalcogenides ideal rare-earth dopant hosts. This, combined with high refractive index, has enabled a number of applications such pulse-shaping [133, 134], modulating [59], and reconfigurable [132] optical elements, including use of photo-induced dichroism and birefringence [135].

Here we consider silicon and GST as high-refractive-index, and silica and sapphire as low-refractive-index compounds and experimentally study holographic control of EIRE from a variety of dielectric and semiconductor (i.e. non-plasmonic) target materials [59, 136, 137]. A comparison among these materials (and prior studies on gold) shows that while surface-relief nanostructuring exerts strong control (as one would expect) over the coupling of SPPs to propagating free space light modes, it can also offer some level of control over TR, but has no discernible effect on the spatial distribution of incoherent luminescent emission.

4.2.2 Design and Fabrication

To inform the selection of holographic source design wavelengths I first recorded EIRE spectra for the unstructured target media shown in figure 4.3(a), with the SEM (operating in fixed-spot mode with energy of 30 keV) and associated apparatus described in Chapter 1. Sources were designed for wavelengths of 800 nm (as per the original study of gold holographic emitters of Chapter 2) a low-emission wavelength for silica and sapphire but near-maximum-emission wavelength for silicon and GST; 1000 nm the wavelength of peak emission from silica and sapphire; and 550 nm a low-emission wavelength for all four dielectric/semiconductor media.

The surface-relief nanostructural patterns required to generate a given output beam are obtained (as described in Chapter 2) as the interference pattern between a reference electromagnetic field generated by the impact of incident electrons and that of the desired object beam. Holographic sources were designed in all cases to generate plane-wave output beams propagating at a polar angle $\theta = 30°$ to the surface normal. The cylindrically symmetric toroidal distribution of TR can be calculated analytically [138] but for holographic source design purposes is preferably obtained numerically via a 3D finite-element model comprising an oscillating dipole aligned with the surface normal and positioned a short distance $h = 50$ nm ($<< \lambda$, where λ is the wavelength of light) above the surface [73, 75, 76]. While still inevitably excluding incoherent luminescent emission generated beneath the target surface, this model accurately reproduces the full electromagnetic near field on both sides of the surface plane, which is excited by impinging electrons, including SPPs where relevant.

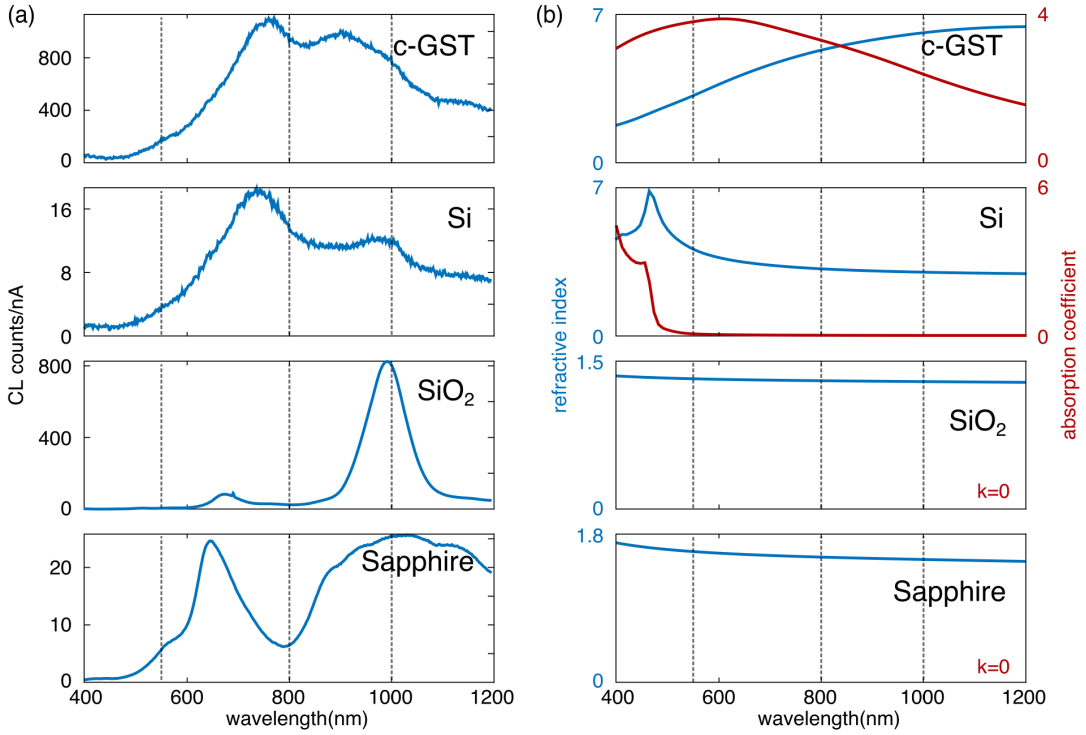

FIGURE 4.3: (a) Electron-induced light emission intensity (in counts per nA of 30 keV electron beam current) spectra for polycrystalline GST, silicon, silica, and sapphire [as labelled]. (b) Corresponding VIS-NIR refractive index and absorption coefficient used in modelling the hologram designs for said materials. Dashed lines denote wavelengths selected for holographic emitter design.

For each combination of emission wavelength and target medium the patterns obtained by interference of the computed surface-plane (reference) and desired output (object) fields were converted to binary masks [77, 78] for ease of fabrication by focused ion beam (FIB) milling. The central portions of the 800 nm design patterns, comprising patterns of offset concentric oval rings around the electron beam injection point with radial dimensions determined by the emission wavelength and refractive index of the target medium, are shown compared to the gold reference design in figure 4.4. Compared to Silicon and GST, Gold, in which a large proportion of the surface field is due to SPP oscillations that have a reduced wavelength compared to free-space light, has a smaller pattern of rings, and a larger number of rings than in either of the dielectric cases.

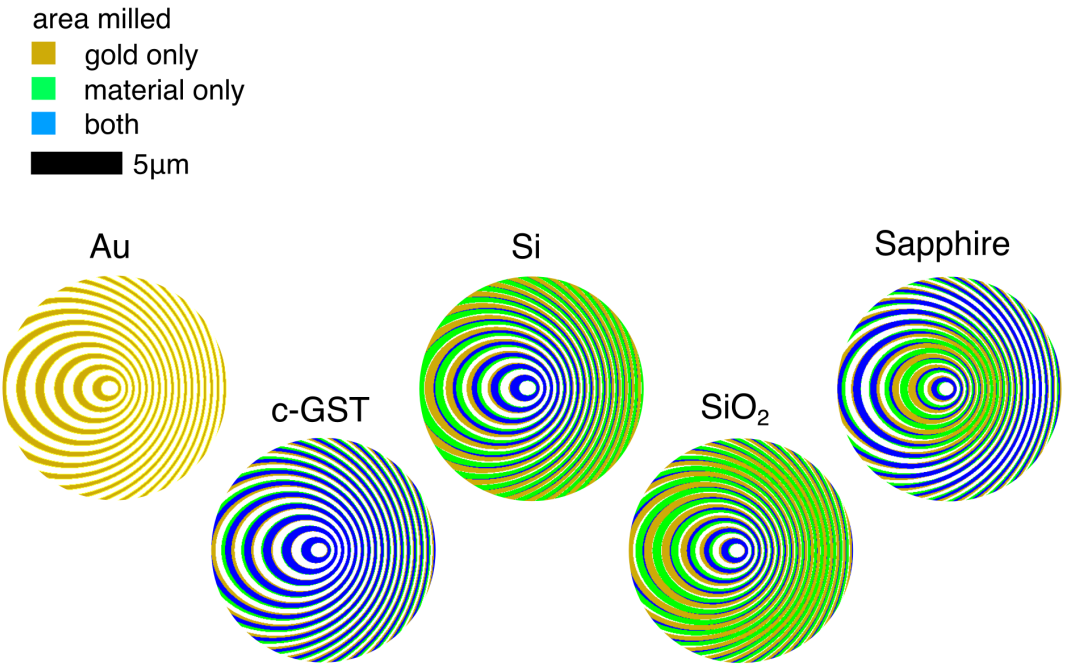

FIGURE 4.4: Holographic milling patterns for dielectric and semiconductor materials compared to reference Au design. The central detail of each 20 μm radial design is shown for each material used in the study.

Designs were milled to a depth of 60 nm over 20 μm radius circular domains in all cases, the full set of samples used is shown in figure 4.5. They were milled directly into the silicon and GST samples (respectively, a piece of ∼500 μm thick double-polished wafer, and a 500 nm thick sputtered and thermally annealed film of $Ge_2Sb_2Te_5$ on a 200 μm polycrystalline Si substrate). The sapphire and silica samples (respectively ∼250 μm thick and ∼500 μm double-polished wafers) were first coated with a 10 nm layer of platinum (selectively over the target area, via electron beam-induced deposition from a gaseous precursor within the FIB milling system) to prevent the local build-up of charge under the ion beam with patterns milled into the underlying dielectric through this conductive layer, which was subsequently removed.

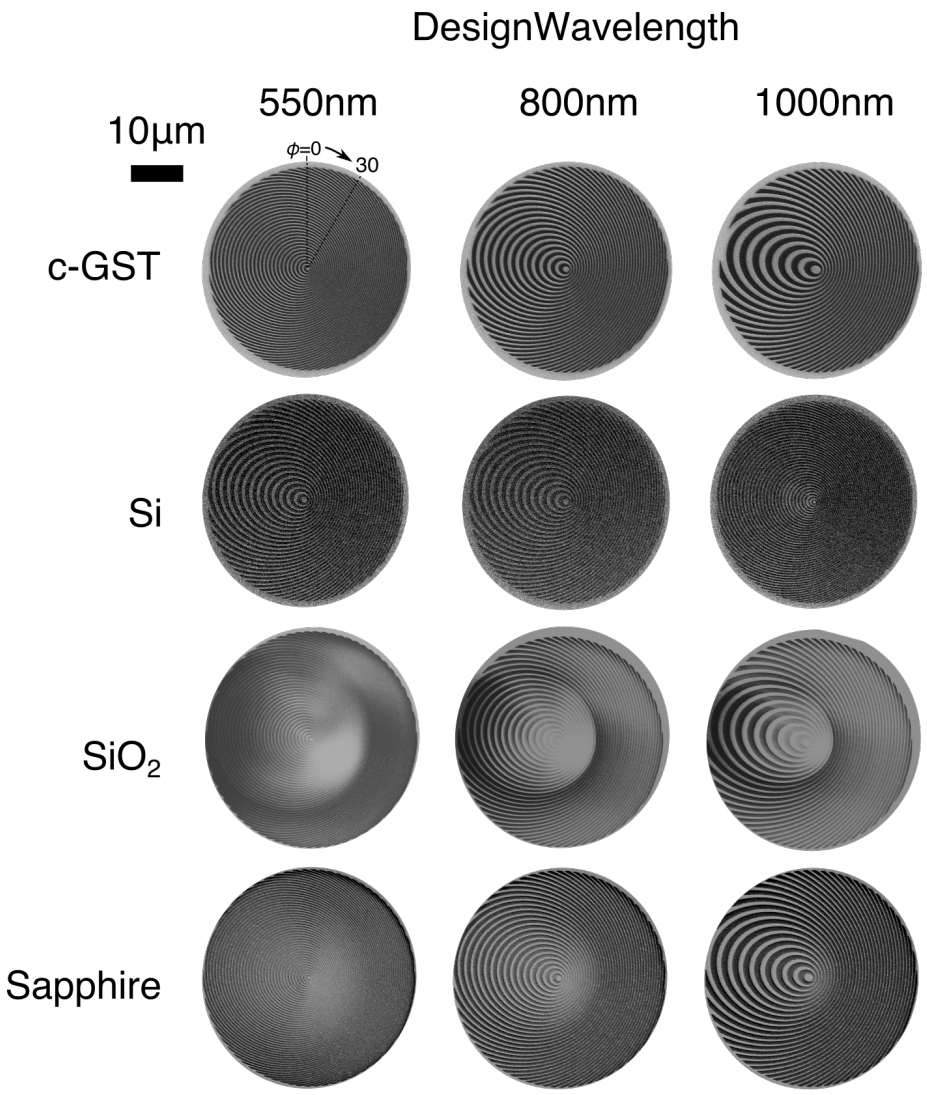

FIGURE 4.5: SEM images of hologram samples for all materials and design wavelengths. Each sample is shown rotated azimuthally to correspond to the emission polar maps shown in figure 4.7. Some distortion is evident in the imaging process of SiO_2 due to surface-charging of the sample in the SEM.

4.2.3 Semiconductor and Dielectric Holographic Source Characterization

The angular distribution of light emission at each of the design wavelengths (± 20 nm) is recorded for each material in figure 4.7, with an electron energy of 30 keV and beam diameter of ∼50 nm. Beam current varied with the resistivity of each material and was further adjusted to allow for a stable image of each structure with minimal charging. The current used for GST was ∼7.5 nA, silicon, ∼8.5 nA, silica, ∼6.5 nA, and sapphire, ∼1.5 nA. For GST and silicon an integration time of 60 s was used. For silica and sapphire, materials with high levels of luminescence, an integration time of 8 s was used to avoid saturating the detector. Directly after taking a measurement of each holographic sample output, the corresponding emission distributions were also recorded at each wavelength for unstructured regions of each target material for reference. A figure of merit (FOM) for the proportion of light directed by the holographic structure into the intended directional output beam is evaluated as the difference between the fraction of the total counts (integrated over the entire emission map) falling within the beam spot, which is taken to comprise the brightest pixel within ± 20° in θ or ϕ of the expected output beam direction and the surrounding pixels with greater than half of that brightness level and the same fraction evaluated over the same pixels for the reference (unstructured material) emission map. That is, an ideal device that focuses all light into a direction in which no light is emitted from an unstructured surface of the same material would have a FOM of 1. Figure 4.6 recaps the results with a comparable Au sample from Chapter 2 for comparison, with a corresponding FOM value of 0.1502.

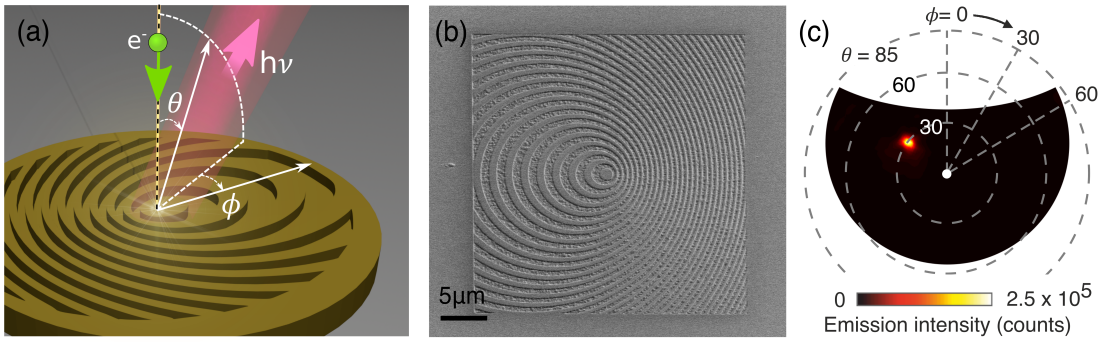

FIGURE 4.6: (a) Schematic representation, (b) SEM image of sample and (c) result of Au metasurface sample for comparison with dielectrics. The sample shown achieves a FOM of 0.1502 as described in the text.)

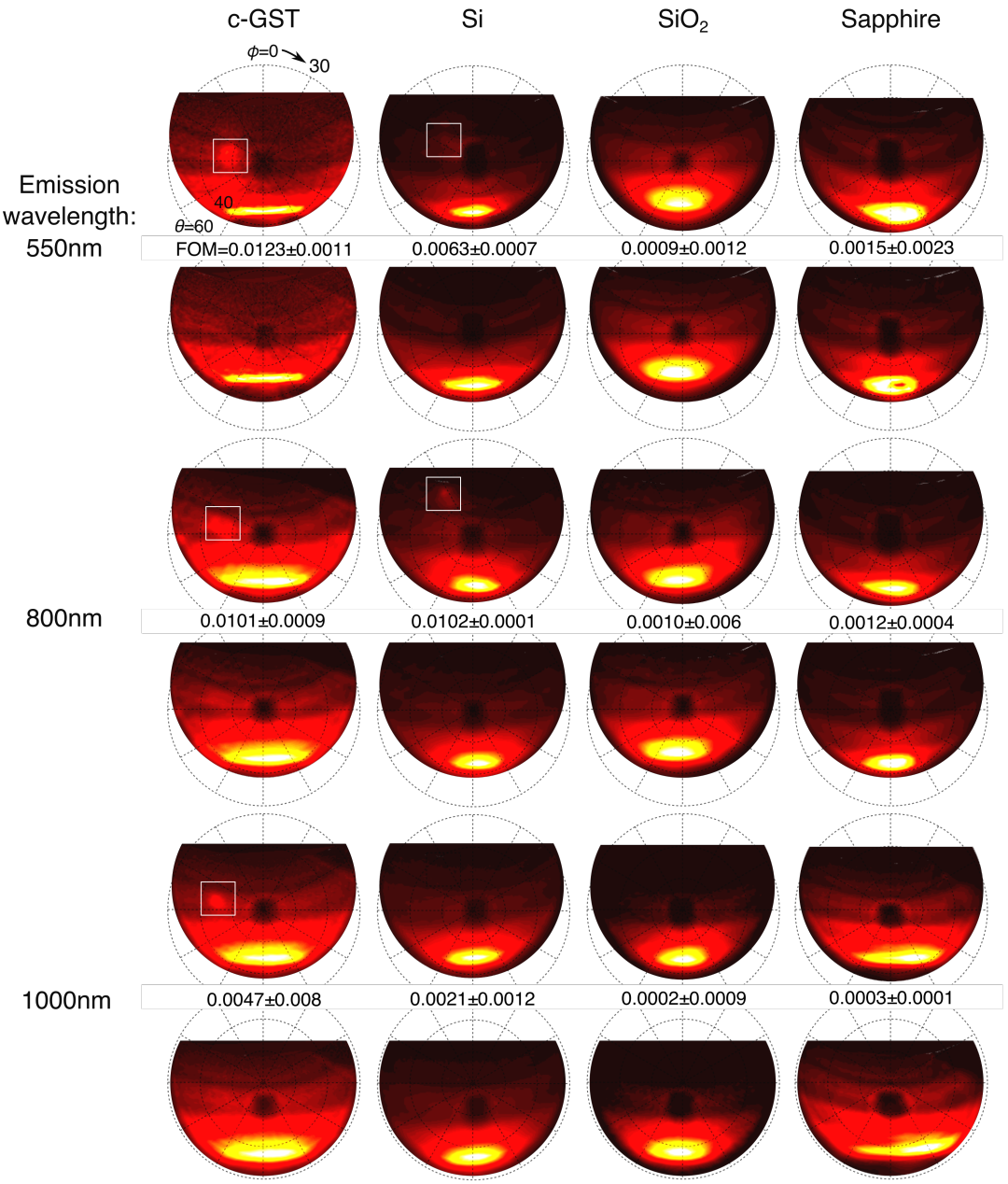

FIGURE 4.7: Angular distribution of electron-beam-induced light emission at 550, 800, and 1000 ± 20 nm (rows as labelled) from holographic surface-relief structures designed for said wavelengths (each row, top) and CL response of unstructured material (each row, bottom) for polycrystalline GST, silicon, silica and sapphire (columns as labelled), with corresponding figures of merit for the proportion of light emitted in the intended $\theta = 30°$ direction. The azimuthal emission angle ϕ is determined simply by the in-plane orientation of the samples mirror symmetry axes, and was set to 300° in all cases. (The bright feature at the bottom edge of each emission map is an artefact of mirror geometry/alignment and may be disregarded.)

In the case of the low-index dielectrics silica and sapphire, the distribution of emitted light for structured and unstructured surfaces is practically unchanged. For these materials, in all design wavelength cases, the FOM is below or close to the error for the measurement, defined as the FOM given when measured from the direction opposite that of the focused spot. The spectral dispersion of these materials' electric permittivities is essentially flat over the VIS-NIR range, implying that the same is true of their TR emission. In the spectra of figure 4.3 the TR contribution may thus be taken as the low (short-wavelength) baseline emission level, i.e. as almost negligible against the strength of the intrinsic incoherent luminescence component of emission. This is particularly bright (in terms of photons per electron), as compared to any material regardless of emission mechanism for silica at 1000 nm. It then follows that the holographic structures exert no influence over the angular distribution of luminescent emission.

For GST a directional output beam is clearly visible at all three design wavelengths, and for silicon a beam can be discerned at 550 and 800 nm, though in all cases the FOM is at least an order or magnitude lower that of the gold holographic source described in Chapter 2. Both materials have rather higher refractive indices than silica and sapphire (though losses are also much higher), and in the case of GST index increases strongly with wavelength. In the knowledge that the holographic structures exert no control over the angular distribution of incoherent luminescent emission and that silicon, as well as crystalline GST above a wavelength of 620 nm, does not support SPP propagation, we conclude that the directional beams are derived from transition radiation.

4.3 Conclusion

It is clear from the prior study of holographic sources on gold (and of course expected) that the surface-relief structures are highly effective in coupling SPPs, i.e. electromagnetic waves coupled to the metal surface the dominant component of EIRE in that case, to a specified free-space output beam.

The ability of the holographic structures to exert an observable level of control over TR emission may be understood to result from its coherent nature and its characteristic distorted dipolar spatial distribution, whereby some fraction of light is emitted at grazing angles (θ approaching 90°) such that it may scatter from the holographic grating elements. In contrast, incoherent luminescence has a characteristically Lambertian spatial distribution, whereby a negligibly small fraction of photons are emitted at grazing angles.

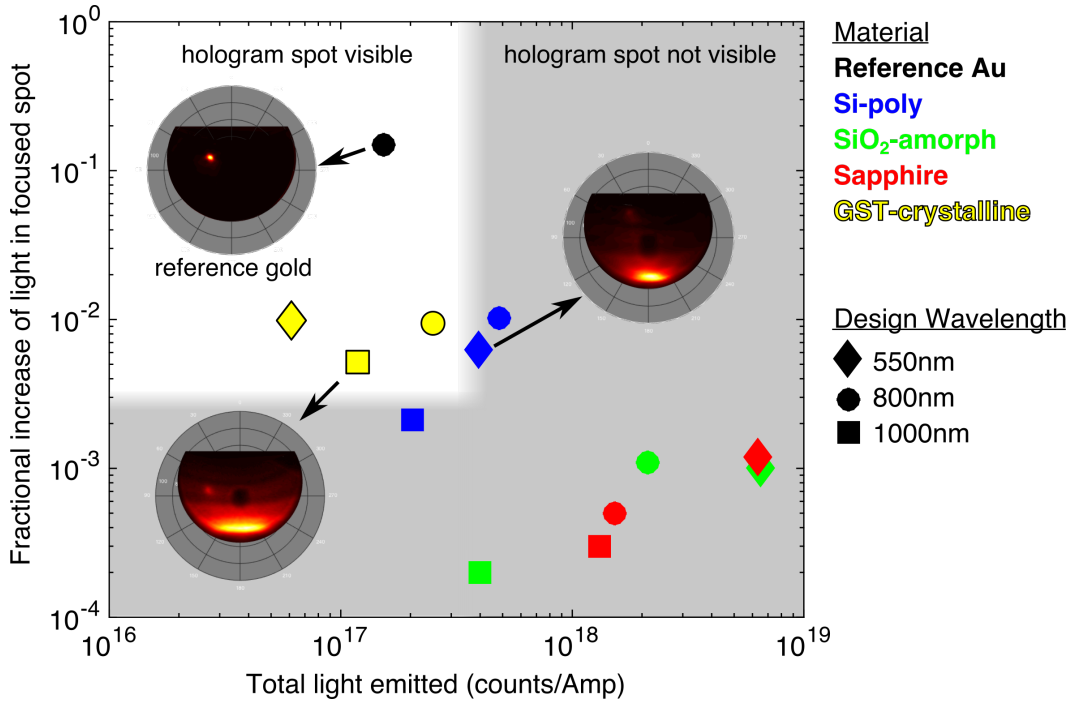

FIGURE 4.8: Total light emitted by hologram sample vs. relative brightness of spot for each fabrication material and design wavelength. An order of magnitude separates the light directivity of gold from that of the high-index dielectrics. Very little relative light was directed into the design area for the low-index dielectrics.

Figure 4.8 shows total light emitted vs. proportion of light focused by the hologram design for each, including for the reference Au sample. While the degree of light focusing achieved by the Si and GST samples is an order of magnitude less than that of gold, the focused TR is clearly visible in these two materials.

In summary, we have demonstrated that holographically nanostructured surfaces can be engaged to manipulate the spatial distribution of transition radiation (TR) generated by electron beam impact on dielectric/semiconductor surfaces. Surface-relief patterns can be engineered to produce directional output beams at chosen wavelengths, and is most effective (and/or most clearly resolved) for high-refractive-index media in the absence of strong incoherent luminescent emission (which is unperturbed by the holographic structure) and strong plasmonic emission (which can overwhelm the TR signal for metallic target media). The concept offers a means of discriminating between TR and luminescent components of electron-induced light emission in materials analysis and of controlling the output of TR-based electron-beam-driven coherent light sources, such as have been reported in the terahertz and x-ray domains [139, 140].

Chapter 5

Smith-Purcell Radiation from Compound Blazed Gratings

5.1 Introduction

While impact interactions between nanostructured materials and medium-energy free electrons have been harnessed to remarkable effect recently in various forms of electron-induced radiation emission (EIRE) imaging, detailed in previous chapters [36, 38, 88], proximity interactions between electrons and surfaces provide many techniques for probing, spatially mapping, and generating light or electron-beam modifying effects from nanostructures [141–144]. The recent addition of short-pulse (usually femtosecond laser-driven) electron sources add the dimension of temporal resolution [145, 146].

The interaction of free electrons and photons within nanostructured materials has also been engaged for the realization of microscopic electron-beam-driven, optical frequency light sources. A variety of periodic structures from simple planar gratings to cylindrical metal/dielectric undulators, photonic crystals, metamaterial and nanoantenna arrays, and 2D holographic gratings have been engineered to couple electron energy to free-space and guided light modes of prescribed, if not tunable, wavelength, direction, divergence and topological charge [37, 38, 88].

When the conversion of light from the evanescent field of a ballistic electron involves a surrounding or nearby isotropic medium, in which the particle travels faster than the local velocity of light, the resulting illumination is termed Cherenkov radiation. The evanescent electric field can also be coupled by scattering over a regular pattern such as a grating, resulting in light that is termed Smith-Purcell (SP) radiation. SP emission characteristics of simple gratings are a well-understood phenomenon and have a wide

array of technology applications such as lasing [147–149], particle beam analytics [150], and radiation sources for a wide range of wavelengths [151, 152]. In addition, several methods of enhancing SP emission have been developed in recent years, extending the reach of this technology. Here, I show that for a compound grating made up of several closely-spaced slits repeated for each period, the characteristic angular dispersion of SP radiation can be selectively attenuated or enhanced. We analyze, in particular, the change in intensity as slit elements are added to the structure for two sizes and how this affects emission enhancement.

5.2 Electron Near-Field Emission Coupling

The exponentially decaying evanescent field of a travelling electron, spanning a wide spectral range at medium-to-relativistic velocities [73, 153–155], remains evanescent unless the speed of light in the surrounding medium is less than the electron velocity, in which case Cherenkov radiation will be generated [156], or unless additional momentum is provided via scattering at an optical inhomogeneity as electrons pass close to (within a few tens of nanometers of) a material structure, as in Smith-Purcell (SP) radition [86, 150]. The SP mechanism, though well-understood, remains an avenue of much research because of its utility as both a flexible radiation source and particle beam diagnostic tool.

5.2.1 Electron Relativity and Emissions

When charged particles travel near or in a medium for which the phase velocity of light is less than that of the particle, Cherenkov radiation will be emitted and the particle will lose energy, slowing it. The spectrum of the radiation is described by the Franck-Tamm formula with the intensity inversely proportional to the wavelength. When the radiation is emitted in the visible spectrum, its high-frequency content will always be stronger than low-frequency content, giving it the characteristic blue-tinged glow commonly seen in water-cooled nuclear reactors.

The effect is the optical analogue of other shock wavefronts such as a sonic boom. Hence, one feature of Cherenkov radiation, its angle of emission, can be explored geometrically. For an ideal, dispersionless medium of refractive index n, the phase velocity is c/n, while a particle travels with velocity v_p. The angle of emission is then:

$$\cos\theta = \frac{c}{nv_p} \tag{5.1}$$

Figure 5.1(a) shows the angular dependance of Cherenkov emission on the particle velocity and local refractive index. With $c/n > v_p$, Cherenkov radiation does not occur (figure 5.1(b)), while for $c/n < v_p$ Cherenkov radiation can be interpreted as expanding wave fronts as the particle moves further in a given time t than the light emissions themselves (figure 5.1(c)).

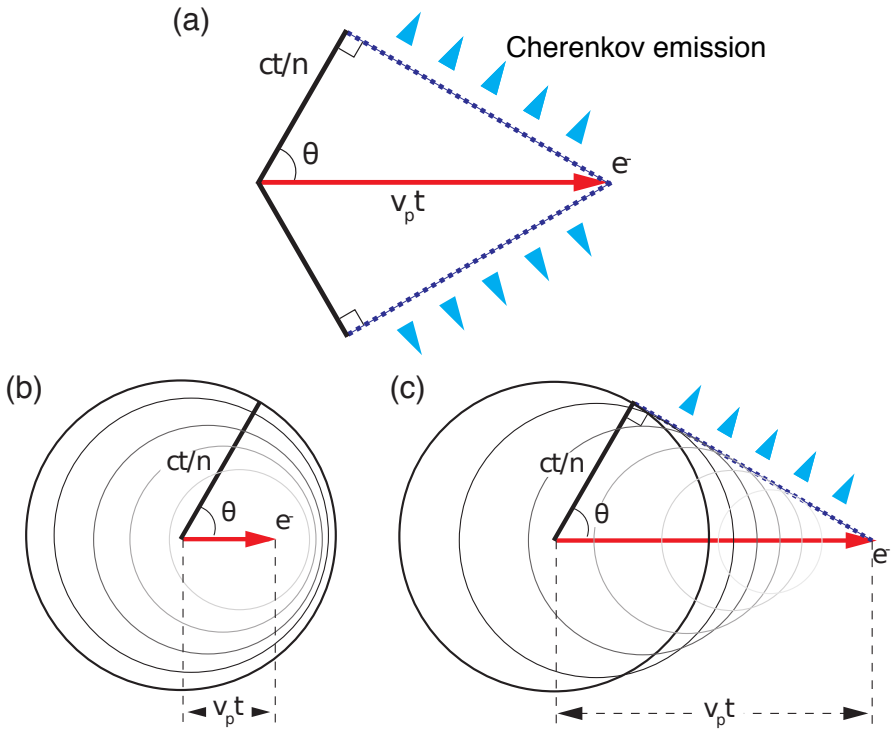

FIGURE 5.1: (a) Geometric interpretation of equation 5.1 for time t. (b) Particle propagation with $\frac{c}{n} > v_p$. (c) Shock front interpretation with $\frac{c}{n} < v_p$.

In any real dispersive medium, n is a function of the frequency of light ω, and therefore the spectrum of Cherenkov radiation will have an angular distribution. This phenomenon is thus widely used in studying high-energy particles, as their velocity can be precisely determined by interrogating the wavelength and angle of emissions.

In a normally dispersive medium, refractive index tends to increase with decreasing wavelength. However, in the case of sub-ultraviolet wavelength emission - X-rays and gamma rays - refractive index decreases to just below unity due to inelastic forward scattering in the material. Another way of considering this drop in refractive index is thorough the plasma frequency of the material. At a frequency well above that of any electronic resonances of the structure, the dielectric permittivity reduces to [157]:

$$\varepsilon(\omega) \approx \varepsilon_0 \left(1 - \frac{\omega_p^2}{\omega^2}\right) \tag{5.2}$$

Where the plasma frequency $\omega_p^2 = \frac{Ne^2}{m_{eff}}$ is much smaller than ω.

Hence the refractive index above a certain wavelength will remain slightly less than 1, and equation 5.1 no longer holds and Cherenkov radiation is not emitted. At sufficient energies, the Cherenkov radiation of a particle tends to peak in the UV range, drop off quickly as the wavelength approaches sub-nanometer dimensions, and decrease more slowly, depending on the energy of the particle, into the visible and infrared ranges. This dispersive effect results in an emission spectrum that varies with both electron energy and angle relative to the propagation of the beam, features shared with SP radiation derived from a grating structure.

5.2.2 The Smith-Purcell Effect and Enhancement

The term 'Cherenkov radiation' typically applies only to homogenous media. In the case of inhomogeneous media with an effective electric permittivity and index of refraction, the effect is usually known as Smith-Purcell radiation, after the first observation of Cherenkov-style radiation from a metal grating in 1953 [86].

A simple grating of period d provides additional parallel momentum in integer multiples n of its reciprocal lattice vector, $2\pi/d$, to incoming electromagnetic waves, leading to familiar optical diffraction phenomena for light propagating in free space. The same applies in the SP emission process to free electron evanescent fields, enabling a part of the electromagnetic energy to be decoupled into propagating waves when the parallel momentum is smaller than that of light in free space.

A description of Smith-Purcell radiation for an electron packet travelling above a grating requires a modification of the standard Cherenkov description in two ways. First, the particles are travelling above, rather than within, the particle-retarding structure or media. Second, the emission angle and spectrum of the media depends not on its intrinsic properties, but instead on the effective properties imposed by its geometry [153, 158]. Figure 5.2 shows the Smith-Purcell emission configuration, as well as the geometric parameters defined in this section.

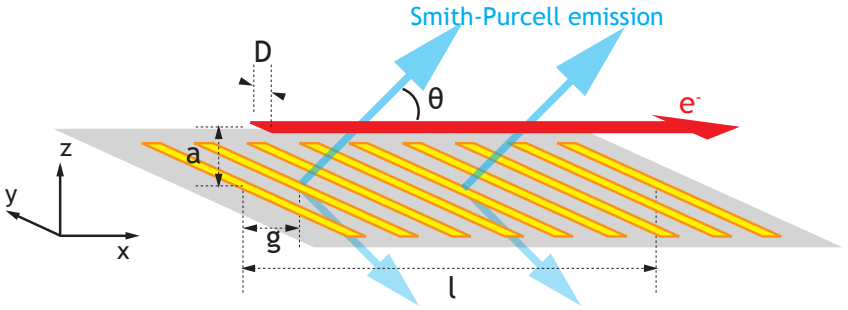

FIGURE 5.2: Smith-Purcell emission arrangement and geometric parameters governing emission from the grating.

The Smith-Purcell emission can be analyzed as a composition of m diffracted waves, with the angle of propagation dependent on grating period g:

$$\lambda = \frac{g}{m}\left(\frac{c}{v_p} - \cos\theta\right) \tag{5.3}$$

Analysis of the diffracted waves in [153] yields an order-of-magnitude approximation for the energy per unit area, per wavelength emitted into the far-field at distance above the grating z:

$$U = \frac{e^2 k}{2\pi z}\delta_m^2 \sin\theta \exp\left[-\frac{2cka}{v_p\gamma}\right]dk \tag{5.4}$$

Where e is the fundamental electron charge, k is the wave number, a is the distance between the grating and the electron path of travel, and δ_m is a correction factor that is 1 under ideal circumstances, and takes into account irregularities in the grating itself.

Taking the ideal case of $a = 0$ and $\delta_m = 1$, brightness per solid angle can be expressed by defining a surface area of emission. If the width of the electron beam is expressed as D, at a distance z from the grating, the area of emission per solid angle θ will be $\frac{Dz}{\sin\theta}d\theta$. Taking the surface current density for a single hypothetical electron as $I = e/D$, brightness (energy flux per unit solid angle per unit frequency) can be expressed as [153]:

$$B = \frac{Ie}{2\pi}k\left|\frac{dk}{d\theta}\right| \tag{5.5}$$

Where k can be defined as a function of θ from 5.3:

$$k = \frac{2\pi m}{g\left(\frac{c}{v_p} - \cos\theta\right)} \tag{5.6}$$

Brightness then becomes [153]:

$$B = \frac{2\pi I e m^2}{g^2} \frac{(\frac{v_p}{c})^3 \sin\theta}{(1 - \frac{v_p}{c}\cos\theta)^3} \tag{5.7}$$

Maximising this equation for θ, the angle of maximum emission from the grating, for a given electron velocity can be found by [153]:

$$\theta_{max} = \arccos\left[\frac{\sqrt{1 + 24(\frac{v_p}{c})^2} - 1}{4\frac{v_p}{c}}\right] \tag{5.8}$$

Figure 5.3 shows the angle at which maximum brightness is observed θ_{max} from equation 5.8 for a given particle velocity. Scaled brightness (equation 5.7) is shown by the color map, with a maximum at 0°, $v_p = c$.

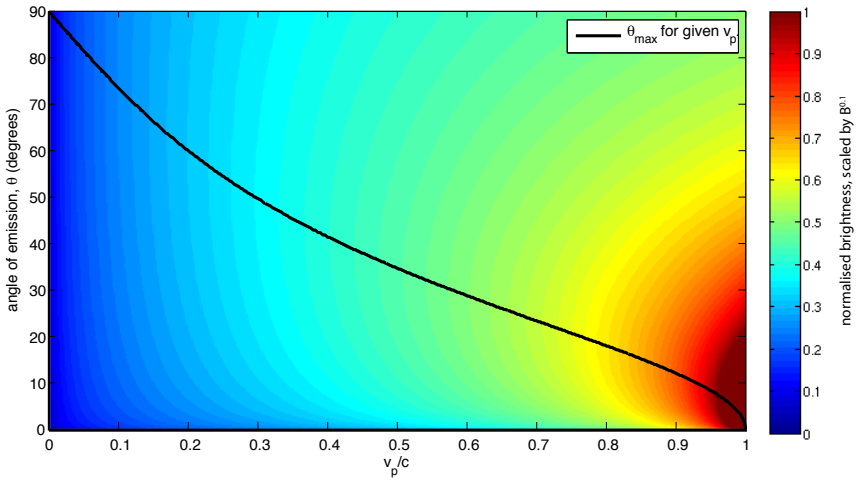

FIGURE 5.3: Angle of maximum emission and scaled brightness for equations 5.8 and 5.7.

The above equations allow a grating to be designed to emit at a desired angle and wavelength or, give the maximum possible emission for an electron at a given velocity [73]. In any real case, a and δ_m will be non-ideal and will reduce the emission by 1-2 orders of magnitude [153]. However, provided a is significantly smaller than the grating size, the wavelength-angle relationships that can be expected remain valid.

Much as for Cherenkov radiation, the electron-energy-dependent nature of the emissions is useful for measuring and manipulating charged particle beams. In addition, structured planar materials have shown many uses in manipulating Cherenkov radiation via the Smith-Purcell effect. In addition to the traditional Smith-Purcell description, the

validity of the usual 'effective parameter' description in the case of metamaterials has been shown for Cherenkov radiation [159]. This has enabled a well-defined dispersion modelling process for exploring the interactions of Smith-Purcell gratings with other materials to emerge [160].

SP-type gratings are useful in a variety of broadband radiation sources and amplifiers, including in free-electron laser (FEL) systems. The conversion from optical to particle kinetic energy has proven to be an effective means of generating a wide range of wavelengths from microwave to X-ray frequencies, with potentially very high power [152]. The properties required of regular SP type gratings in an FEL are well understood [161], meta-structuring of the grating could potentially improve FEL performance further. In addition, regular SP gratings can be useful for beam dynamics, and it has been shown that the properties of sub-picosecond electron bunches can be derived from their emissions [162].

In addition to the applications of SP emission from regular gratings, a number of modified SP structures have emerged to offer enhanced light emission and other functionalities. In an analog to negative-refractive index metamaterials, double-negative metamaterials have been shown to emit 'reverse' Smith-Purcell radiation that travels at an angle in the opposite direction from the electron [163]. Variations in the thickness of layers have been shown to enable the efficient outcoupling of light in directions other than those normal to the surface above which the electron travels [164]. Studies of short-range disorder in such structures have shown that SP radiation can be useful in mapping many surface properties [165].

In the THz domain, it has been proposed that improvements in monochromaticity and directivity may be achieved by modifying the fill factor of simple, singly periodic SP gratings [143, 166], by graduating their depth [151], or by making them aperiodic [142]. Efficient microwave Smith-Purcell radiation has also been shown in the case of negative effective epsilon metamaterials [159].

The group at the Southampton Optoelectronics Research Centre has previously studied tuneable 'nano-wells,' in which an electron can emit Smith-Purcell radiation from all sides, rather than simply travelling over a planar substrate [71, 167]. Both the spectral frequency and bandwidth of the emissions can be tuned by varying the number of metal-dielectric layers and their thicknesses. This nano-well design, and applications of SP radiation are shown in figure 5.4.

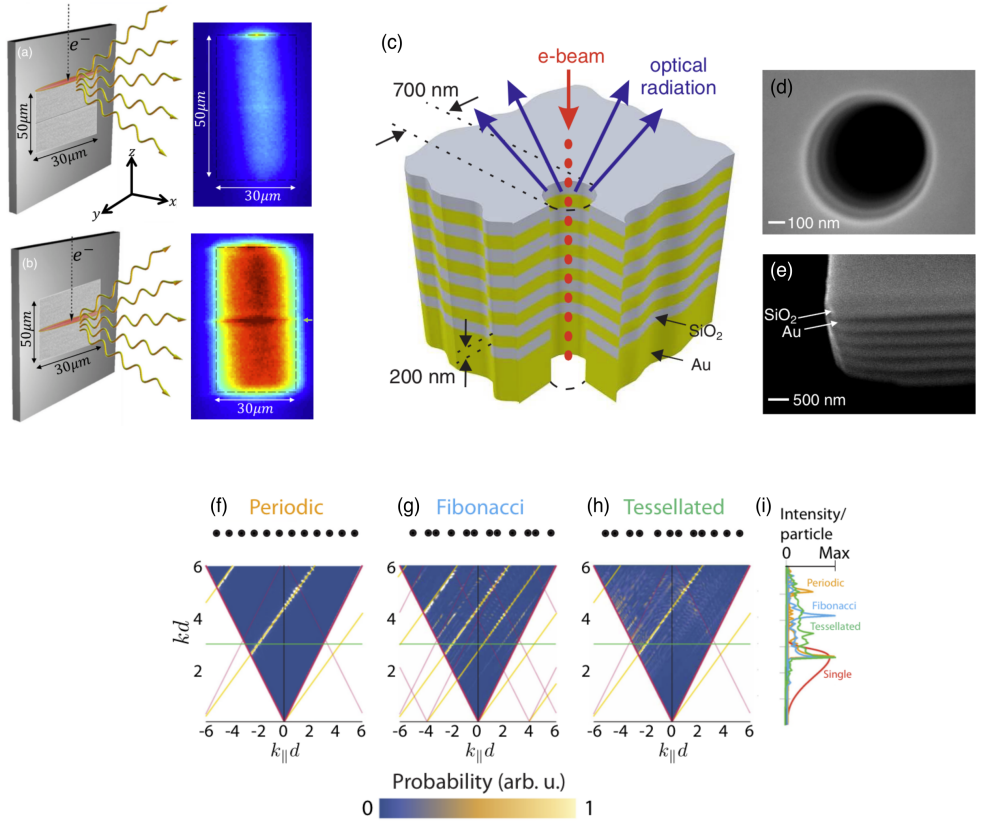

FIGURE 5.4: Direct imaging of enhanced and inhibited emission from line defect. (a,b) Illustration of the electron beam interacting with SP-type gratings with line defects fabricated in the samples. Adjacent are false color optical images of the light emission from the corresponding samples showing a clear enhancement of the emission from the line defect. From [165]. (c-e) Free electron beam nanohole light source. (c) Schematic cut-away section. (d) Scanning electron microscope image of a light well fabricated in a gold- silica multilayer. (e) The alternating metal-dielectric layer structure as seen at an exposed corner of the sample. From [71]. (f-i) Calculation of emission from aperiodic SP-type arrays. (f-h) SP emission probability as a function of photon wave vector k and parallel wave vector k for the three different arrays as shown by representative dots. (i) Angle-integrated emission probability for the three types of arrays, as compared with the emission from a single particle. From [142].

5.3 Compound Smith-Purcell Enhancement Gratings

It is well-established in diffractive optics that blazed and complex, compound gratings can provide for manipulation by design of the spectral and spatial distribution of reflected, transmitted and guided light modes by adding new degrees of freedom for control of the phase distribution of electromagnetic field. While an electron beam passing over a surface is not equivalent to incident optical excitation, the general principle of using sub-period structures to modify the resonant modes available applies. The -2 reflected order for a compound optical grating is shown in figure 5.5 to illustrate the complexity

in modelling the response of such a surface in the optical realm. These types of optical gratings find application in such areas as metrology [168], beam shaping [169, 170], spectral filtering [171], spectroscopy and sensing [172].

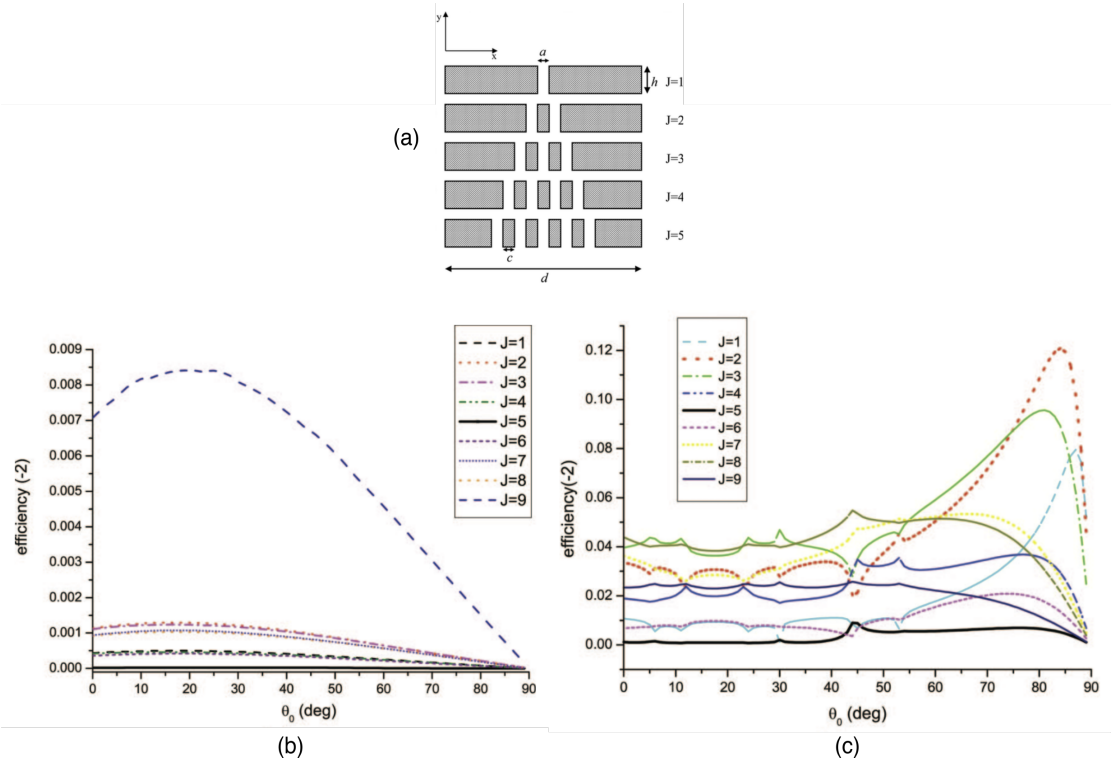

FIGURE 5.5: Optical compound grating response as an example of reflection-mode compound grating function. A number of resonance peaks are manipulated in the grating p-polarized higher-order reflection response (c). (a) Grating profiles. (b, c) Efficiency of the -2 reflected order of the grating profiles as a function of incidence angle for gratings with $a/d = c/d = 0.05$, $h/d = 1$, and wavelength $\lambda/d = 0.3$ with varying number of slits, J. (b) s-polarization, and (c) p-polarization. From [173].

Gradient metasurfaces provide for similarly refined control of reflection/transmission phase distributions in the domain of sub-wavelength periodicity, enabling for example polarization-independent reflection [174], achromatic flat optical elements [175], and nonlinear optical repsonses [52, 176]. Similar principles may be applied to tailor the electron-induced light emission from SP grating structures. Here I computationally analyze optical frequency light emission from compound gratings excited by the passage of medium-energy free electrons travelling parallel to the grating plane. It is found that by varying the effective fill factor of a multi-slit Smith-Purcell grating, the emission efficiency of the grating at both the fundamental and higher-order wavelengths can be modified, and even enhanced over a simple rectangular grating.

5.3.1 Structure and Modelling

In the present case, I have analysed SP emission at optical frequencies from a family of compound grating structures using the particle-in-cell finite-difference time-domain (PIC-FDTD) computational method in CST Particle Studio. This solver models the mutual coupling between charged particles and dynamic electromagnetic fields. Thus, particle movement is linked to the electromagnetic response of the surface. A constant magnetic field is used across the simulated space to model a collimated electron beam, but electron velocity changes as energy is coupled into the grating.

I considered 2D geometries in the xz-plane as illustrated in figure 5.6: gratings are modelled as 50 nm thick layers of perfect electrical conductor in vacuum, perforated with patterns of vertical slits. Each comprises 12 periods of length d, within which there are g slits of width $a/2$ and (sub-)periodic spacing a. The grating fill factor is defined as $f = ga/d$. The transient electrodynamic simulation space is bounded by perfectly matched layers in the z directions at $z = \pm$ 500 nm and in the x direction at the grating ends. The field is then propagated 100 μm radially to calculate the far field result at each angle θ. Electrons propagate in the $+x$ direction with a beam width of 4 nm (corresponding to a minimum of 2 meshing cells in the vacuum region). The reference structure is a simple rectangular grating for which $f = 0.5$ (i.e. $g = 1$; $a = d$). I initially identified a combination of period $d = 275$ nm, electron energy $E = 32.5$ keV, and impact parameter (distance between grating surface and electron beam axis) $h = 7$ nm that optimizes light emission at $\lambda = 800$ nm in the surface-normal ($\theta = 90°$) direction for the reference grating. These values are maintained for all subsequent iterations as the sub-periodic structure is varied.

For this grating geometry, the 'effective fill factor' of the compound-grating model was increased as shown in figure 5.6(b), by increasing the number of slits, g, from 1 to 6, the maximum possible for a period of $d = 275$ nm and a silt distance of $a = 40$ nm.

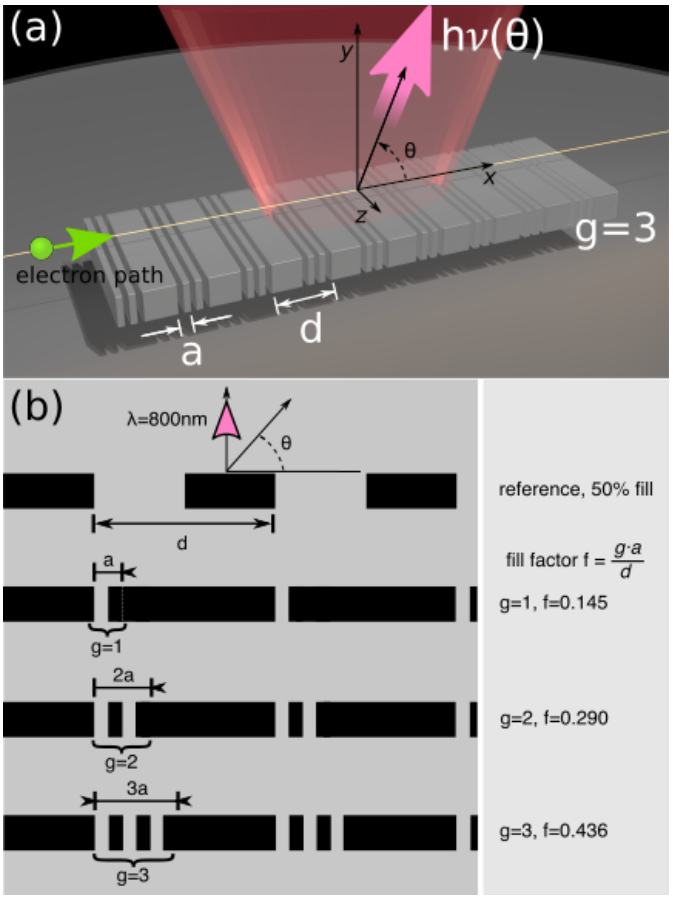

FIGURE 5.6: Compound grating Smith Purcell light sources: (a) Artistic impression of electron-beam-induced optical frequency radiation emission from a grating comprised of g [= 3 as shown] slots of width a within each fundamental period of length d. (b) Dimensional schematic of numerically simulated compound grating geometries [illustrated for values of g up to 3], and the simple rectangular reference grating.

5.3.2 Results

With the same fundamental period d, compound gratings maintain the same relationship between emission wavelength λ and emission angle θ as the reference grating for emission orders $n = 1$ and $n = 2$, as shown in figure 5.8. The relative magnitudes of emission (c.f. diffraction efficiencies) though are functions of the sub-periodic parameters a and g. For a fixed slit width of 20 nm ($a = 40$ nm):

Surface-normal emission at 800 nm is maximized when $g = 3$, reaching an intensity 85% of that of the simple reference grating. This maximum is attained when the fill factor is closest to 0.5, i.e. closest to that of the reference structure, though for smaller slot widths the optimum fill factor is found to decrease as shown in figure 5.7.

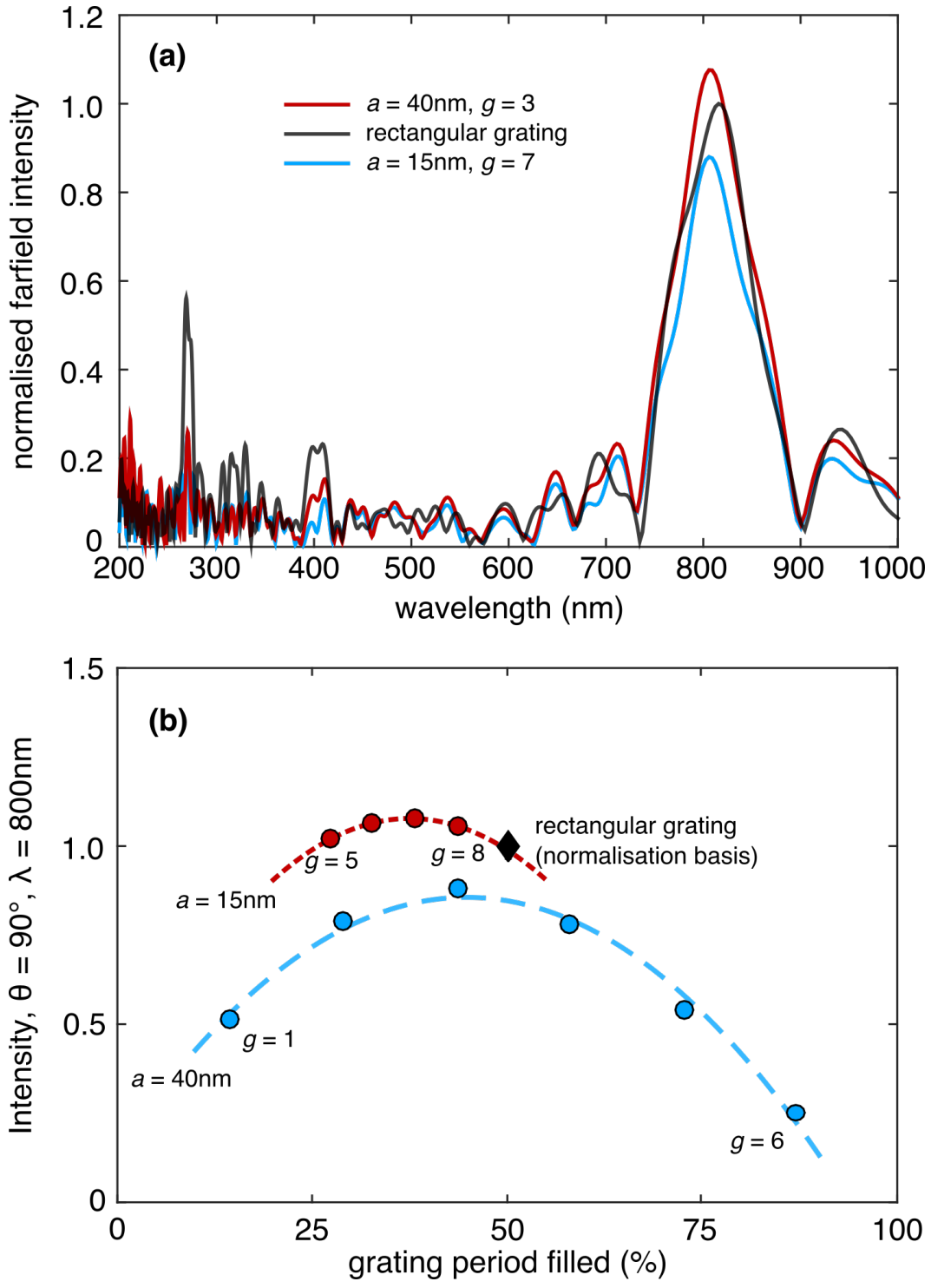

FIGURE 5.7: Compound Smith-Purcell grating efficiency: (a) Spectrum of surface-normal [$\theta = 90°$] far-field intensity for the most efficient compound SP gratings at each slit dimension used: slit widths $a = 40$ nm, $g = 3$, (blue line) and $a = 15$ nm, $g = 7$, (red line) as given by sections indicated in figure 5.8. Shown normalized to the peak 800 nm intensity for a rectangular reference grating (black line). (b) Dependences of 800 nm, normal direction far-field intensity on effective fill factor, i.e. the number of sub-periodic slots g, for slot widths $a = 15$ nm (red dashed line) and 40 nm (blue dashed line). The single filled diamond marker represents the reference grating. In all cases, the fundamental period $d = 275$ nm and electron energy $e = 32.5$ keV

The complete set of frequency-emission angle plots for the set of gratings modelled is shown in figure 5.8. Stronger second-order emission ($n = 2$; $\lambda = 400$ nm) at $\theta = 90°$ is observed from the compound gratings than from the simple rectangular reference grating, when $g = 5$. Second-order emission intensity is maximized at this grating number and angle, an enhancement of 34% over the rectangular grating. Increased levels of second order emission over the rectangular grating model are also observed at shallower angles relative to the electron trajectory for other grating numbers. For example, for $g = 2$, $\theta = 70°$, an enhancement of 24% is seen. This can be seen as analogous to the behavior of compound optical diffraction gratings at varying angles. As the incident angle is swept for a given wavelength, the reflection efficiency generally increases, but with several null points dependent on the geometry. At many particular angles, the reflection efficiency can be greater than that of a standard rectangular grating [73]. The general proportion of emission from the 800 nm and 400 nm modes follows that of a single slit. Figure 5.9 shows this comparison.

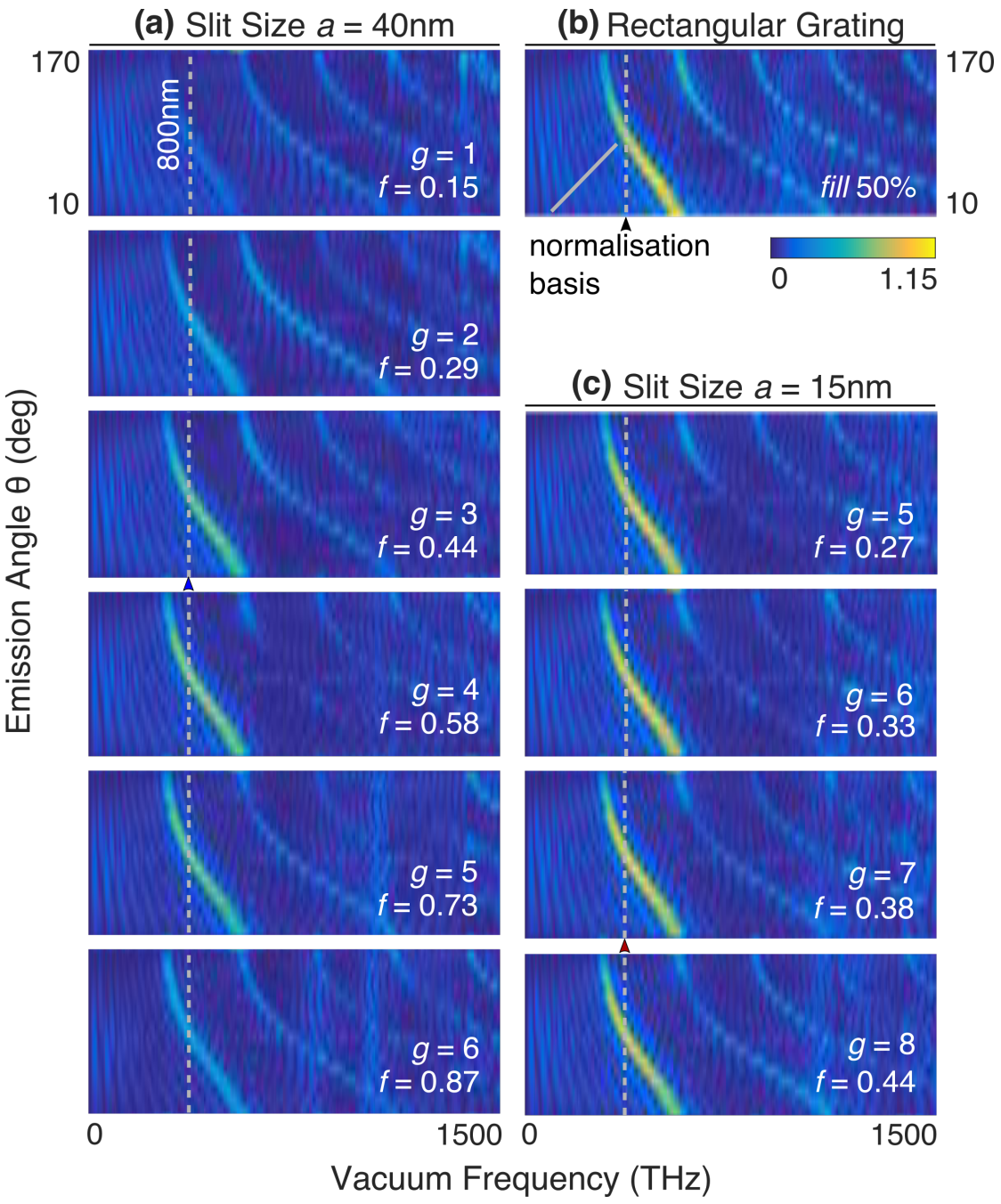

FIGURE 5.8: Smith-Purcell emission from compound gratings: Angular dispersion of first and second order [$n = 1, 2$] SP emission wavelength for gratings [simple or compound] of period $d = 275$ nm at an electron energy $E = 32.5$ keV for: (a) compound gratings of slit element size $a = 40$ nm, up to $g = 6$ slits. (b) Rectangular grating of 50% fill used as normalization basis. (c) compound gratings of slit element size $a = 15$ nm, up to $g = 8$ slits, showing enhancement of 7% over the normalization basis for $\theta = 90°$, $\lambda = 800$ nm. Arrows show sections used for corresponding colors of specta included in figure 5.7(a).

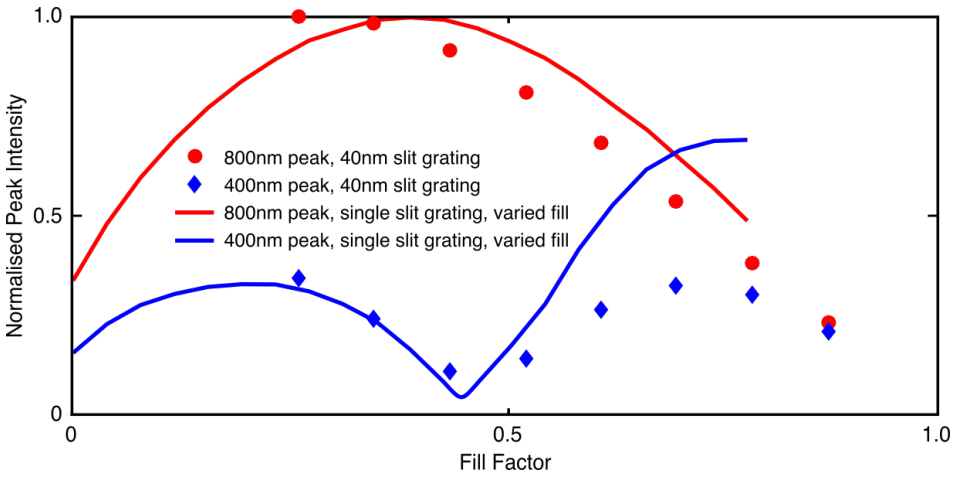

FIGURE 5.9: Emission at 800 and 400nm wavelengths for single grating of varied fill compared with compound gratings with slit size $a = 40$nm of varying effective fill factor as given in figure 5.6. Normalised to greatest 800nm peak for compound grating and single slit grating.

Following the increase in surface-normal emission as the effective fill factor approached $f = 0.5$ in the $a = 40$ nm gratings, a series of gratings with reduced slit size was tested to see whether emission could be enhanced above that of a standard Smith-Purcell effect rectangular grating of 50% fill. For each element size, different numbers of sub-element slits were used to find the most efficient grating possible for 800 nm emission normal to the surface. While computational limits provide a lower bound on the size of the grating studied, a modest enhancement of 7% over the standard rectangular grating was observed for a slit distance of $a = 15$ nm, with 7 gratings, as seen in figure 5.7. For this slit size, with $g = 5$ to 8, the spectrum is also shown in figure 5.8. These gratings all show decrease in intensity of the higher-order ($n = 2$) mode.

5.4 Conclusion

In conclusion, I have demonstrated a compound Smith-Purcell grating with enhanced emission in the normal direction when compared to a standard rectangular grating. Furthermore, the principles of compound and multi-element diffraction gratings can be used as a tool in understanding Smith-Purcell radiation from repeating structures, and in shaping these emissions to suit a variety of purposes. Indeed, subsequent to the publication of these results, an analytic treatment describing them has been published as [177]. A better understanding of these structures can yield applications in free-electron lasing [155], narrow-band radiation sources [176], and efficient terahertz emitters [153].

Chapter 6

Conclusions

6.1 Summary

This work addresses the applicability of nanostructured elements to shaping light derived from electron-beam excitations. As seen in the experimental demonstrations herein, this output from holographically-designed, electron-beam injected structures can be tailored for low angular divergence and designer phase profile at a selected wavelength. In addition, such light sources have been shown to be amenable for use in an angular-output switching design, making a potentially important contribution to selective-output metasurfaces.

Key achievements of this work include:

- Design and demonstration of holographic patterns for a highly-collimated light emitting metasurface of a few tens of square microns in size, radiating a given wavelength in prescribed direction under electron-beam injection.
- Experimental demonstration of continuous angular output beam steering in polar and azimuthal directions via nanoscale positional tuning of the electron injection for a holographically-designed metasurface.
- Design and experimental confirmation of optical-vortex generating electron-beam injection metasurface capable of high topological-charge output, up to 30.
- Demonstration of direction-division multiplexed holographic free-electron-driven light source, with light emission switched among different output angles by micron-scale repositioning of the electron injection point among domains. Demonstration that cross-talk between adjacent and overlapping domains can be as low as -3 dB

at a only 2 μm separation between injection points, thereby allowing for small arrays (typically $\sim$40 μm across) and rapid switching of the emission direction.

- A computational study of free-electron driven Smith-Purcell emission from nanostructured gratings containing multiple slits per grating period, showing that the relative efficiency of resonant modes can be attenuated or enhanced with the addition and removal of narrow slits.

The principles of nanostructured, metasurface couplers of electron beam energy, whether generating radiation from Smith-Purcell type gratings or charged-particle impact driven devices are powerful tools in shaping emissions to suit such applications as lasing, and electromagnetic sources in a broad range of wavelengths.

The control of energy transfer and conversion, in particular the generation of light, in nanoscale systems is a technological challenge of great importance. With micron-scale dimensions, the freedom to fully control radiation parameters, and the ability to switch parameters at will via localised source positioning offer novel applications in areas such as nano-spectroscopy, chemistry, and sensing. One may thus envisage a chip-scale, dynamically programmable array of holographic light sources, designed to emit various wavelengths and/or wave-front profiles in various, application-dependent directions and orientations for use in such technologies as optical tweezing and spectroscopy of complex nanoscale samples.

6.2 Outlook

The proof-of-concept experiments reported herein leave significant room for further investigation into both the applications and underpinning physics of electron beam driven nanostructures. Specific areas of further productive investigation include quantum phenomena revealed by charged-particle driven nanostructures, time-resolved electron-beam physics, and commercial development of the structurally-derived light properties described in this thesis.

Electron beams have already proven useful for exploring the excitation energy levels in quantum-confined structures such as quantum dots [178, 179], and diamond nitrogen vacancies [180, 181]. The ability to control the electromagnetic excitations from electron beams represents a refinement of this process. In addition, the full energy parameters of the electrons themselves and their relationship to nanoscale structures have yet to be explored. For example, it has been shown that the spin and orbital angular momentum of charged particles are coupled into the polarisation and angular deflection of generated

Cherenkov radiation [182]. A metasurface structure exploiting these effects has yet to be realised.

The growing prevalence of pulsed-laser electron beam sources has enabled a large amount of research using femtosecond-length electron bunches [183, 184]. This enables the time-resolved properties of plasmonic and non-plasmonic electron-beam interactions with nanoscale structures to be imaged, and control over light emitted from these interactions to be better understood. This offers potentially orders of magnitude greater spatial resolution compared to optical methods of such time-resolved imaging [185].

Finally, the use of EIRE material analysis techniques in semiconductor, manufacturing, and geological industries is prevalent. Companies such as Attolight and Delmic continue to apply new discoveries in cathodoluminescent analysis to attaining greater understanding of the new materials and structures that underlie modern nanoscale electronics and optics.

Appendix A

Publications

Journal Publications

1. B. P. Clarke, B. Gholipour, K. F. MacDonald, and N. I. Zheludev. All-dielectric free-electron-driven holographic sources. Appl. Phys. Lett., in press.

2. B. P. Clarke, K. F. MacDonald, and N. I. Zheludev. Direction-division multiplexed holographic free-electron-driven light sources. Appl. Phys. Lett., 112, 021109 (2018). Featured Article.

3. B. P. Clarke, J. K. So, K. F. MacDonald, and N. I. Zheludev. Smith-Purcell radiation from compound blazed gratings. arXiv:1711.09018 (2017).

4. G. Li, B. P. Clarke, J. K. So, K. F. MacDonald, and N. I. Zheludev. Holographic free-electron light source. Nat. Commun. 7, 13705 (2016).

Conference Contributions

Presenting author underlined.

1. Metasurface holographic light sources driven by electron beam. B. P. Clarke, G. Li, J. K. So, K. F. MacDonald, and N. I. Zheludev. CLEO 2016, San Jose, CA, USA, 5 - 10 June 2016

2. (poster) Playing a metamaterial guitar with light: Optically addressable nanomechanical metamaterial. J. Y. Ou, E. Plum, B. P. Clarke, and N. I. Zheludev. CLEO 2016, San Jose, CA, USA, 5 - 10 June 2016

3. (poster) Electron-beam-driven Metasurface Holographic Light Sources. B. P. Clarke, G. Li, J. K. So, K. F. MacDonald, and N. I. Zheludev. New Horizons in Nanophotonics, Chicheley, UK, 23 - 24 May 2016

4. Controlling the direction, topological charge, and spectrum of transition radiation with holographic metasurfaces. G. Li, B. P. Clarke, J. So, K. F. MacDonald, X. Chen, W. Lu, and N. I. Zheludev. Metamaterials 2015, Oxford, UK, 7 - 12 Sep 2015

5. Holographic control of free-electron light emission. G. Li, B. P. Clarke, J. So, K. F. MacDonald, X. Chen, W. Lu, and N. I. Zheludev. CLEO/Europe-EQEC 2015, Munich, Germany 21 - 25 Jun 2015

6. (poster) Directional emission of electron-beam-driven plasmonic nanostructures. G. Li, B. P. Clarke, J. K. So, K. F. MacDonald, X. Chen, W. Lu, and N. I. Zheludev. 7th International Conference on Surface Plasmon Photonics (SPP7), Jerusalem, Israel 31 May - 5 June 2015

7. (invited) Control of free-electron light emission via metasurfaces and plasmonic nanostructures. J. K. So, G. Li, B. P. Clarke, K.F. MacDonald, X. Chen, W. Lu, and N. I. Zheludev. 6th International THz-Bio Workshop 2015, Seoul, Korea, 8-10 Apr 2015

8. Control of free-electron light emission with holographic nanostructures. G. Li, B. P. Clarke, J. K. So, K. F. MacDonald, X. Chen, W. Lu, and N. I. Zheludev. Nanometa 2015, Seefeld, Austria, 5 - 8 Jan 2015

Bibliography

[1] D. R. Smith, J. B. Pendry, and M. C. K. Wiltshire. Metamaterials and negative refractive index. *Science*, 305(5685):788–792, 2004. doi: 10.1126/science.1096796.

[2] Kosmas L. Tsakmakidis, Allan D. Boardman, and Ortwin Hess. 'trapped rainbow' storage of light in metamaterials. *Nature*, 450:397, 2007. doi: 10.1038/nature06285.

[3] Chihhui Wu, Alexander B. Khanikaev, and Gennady Shvets. Broadband slow light metamaterial based on a double-continuum Fano resonance. *Phys. Rev. Lett.*, 106: 107403, 2011. doi: 10.1103/PhysRevLett.106.107403.

[4] Nicholas Fang and Xiang Zhang. Imaging properties of a metamaterial superlens. *Appl. Phys. Lett.*, 82(2):161–163, 2003. doi: 10.1063/1.1536712.

[5] Nikolay I. Zheludev and Eric Plum. Reconfigurable nanomechanical photonic metamaterials. *Nat. Nanotechnol.*, 11:16, 2016. doi: 10.1038/nnano.2015.302.

[6] V. L. Ginzburg and I. M. Frank. On the transition radiation theory. *Sov. Phys. JETP*, 16(15):15, 1946.

[7] M. V. Bashevoy, F. Jonsson, A. V. Krasavin, N. I. Zheludev, Y. Chen, and M. I. Stockman. Generation of traveling surface plasmon waves by free-electron impact. *Nano Lett.*, 6(6):1113–1115, 2006. doi: 10.1021/nl060941v.

[8] J. T. van Wijngaarden, E. Verhagen, A. Polman, C. E. Ross, H. J. Lezec, and H. A. Atwater. Direct imaging of propagation and damping of near-resonance surface plasmon polaritons using cathodoluminescence spectroscopy. *Appl. Phys. Lett.*, 88(22):221111, 2006. doi: 10.1063/1.2208556.

[9] Carrie E. Hofmann, Ernst Jan R. Vesseur, Luke A. Sweatlock, Henri J. Lezec, F. Javier García de Abajo, Albert Polman, and Harry A. Atwater. Plasmonic modes of annular nanoresonators imaged by spectrally resolved cathodoluminescence. *Nano Lett.*, 7(12):3612–3617, 2007. doi: 10.1021/nl071789f.

[10] Y. Inoue and J. Peñuelas. An AOTF-based hyperspectral imaging system for field use in ecophysiological and agricultural applications. *Int. J. Remote Sens.*, 22(18): 3883–3888, 2001. doi: 10.1080/01431160110069863.

[11] Karel J. Zuzak, Michael D. Schaeberle, E. Neil Lewis, and Ira W. Levin. Visible reflectance hyperspectral imaging: characterization of a noninvasive, in vivo system for determining tissue perfusion. *Anal. Chem.*, 74(9):2021–2028, 2002. doi: 10.1021/ac011275f.

[12] M. V. Bashevoy, F. Jonsson, K. F. MacDonald, Y. Chen, and N. I. Zheludev. Hyperspectral imaging of plasmonic nanostructures with nanoscale resolution. *Opt. Express*, 15(18):11313–11320, 2007. doi: 10.1364/OE.15.011313.

[13] R F Egerton. Electron energy-loss spectroscopy in the TEM. *Rep. Prog. Phys.*, 72(1):016502, 2008. doi: 10.1088/0034-4885/72/1/016502.

[14] F. J. García de Abajo and M. Kociak. Probing the photonic local density of states with electron energy loss spectroscopy. *Phys. Rev. Lett.*, 100:106804, 2008. doi: 10.1103/PhysRevLett.100.106804.

[15] Quentin M. Ramasse, Che R. Seabourne, Despoina-Maria Kepaptsoglou, Recep Zan, Ursel Bangert, and Andrew J. Scott. Probing the bonding and electronic structure of single atom dopants in graphene with electron energy loss spectroscopy. *Nano Lett.*, 13(10):4989–4995, 2013. doi: 10.1021/nl304187e.

[16] Feng Wang, Ray Egerton, and Marek Malac. Fourier-ratio deconvolution techniques for electron energy-loss spectroscopy (eels). *Ultramicroscopy*, 109(10):1245–1249, 2009. doi: 10.1016/j.ultramic.2009.05.011.

[17] Viktor Myroshnychenko, Jaysen Nelayah, Giorgio Adamo, Nicolas Geuquet, Jessica Rodríguez-Fernández, Isabel Pastoriza-Santos, Kevin F. MacDonald, Luc Henrard, Luis M. Liz-Marzán, Nikolay I. Zheludev, Mathieu Kociak, and F. Javier García de Abajo. Plasmon spectroscopy and imaging of individual gold nanodecahedra: A combined optical microscopy, cathodoluminescence, and electron energy-loss spectroscopy study. *Nano Lett.*, 12(8):4172–4180, 2012. doi: 10.1021/nl301742h.

[18] Olivia Nicoletti, Francisco de la Peña, Rowan K. Leary, Daniel J. Holland, Caterina Ducati, and Paul A. Midgley. Three-dimensional imaging of localized surface plasmon resonances of metal nanoparticles. *Nature*, 502:80, 2013. doi: 10.1038/nature12469.

[19] H. Cohen, T. Maniv, R. Tenne, Y. Rosenfeld Hacohen, O. Stephan, and C. Colliex. Near-field electron energy loss spectroscopy of nanoparticles. *Phys. Rev. Lett.*, 80: 782–785, 1998. doi: 10.1103/PhysRevLett.80.782.

[20] Steven J. Barrow, David Rossouw, Alison M. Funston, Gianluigi A. Botton, and Paul Mulvaney. Mapping bright and dark modes in gold nanoparticle chains using electron energy loss spectroscopy. *Nano Lett.*, 14(7):3799–3808, 2014. doi: 10.1021/nl5009053.

[21] Ai Leen Koh, Antonio I. Fernández-Domínguez, David W. McComb, Stefan A. Maier, and Joel K. W. Yang. High-resolution mapping of electron-beam-excited plasmon modes in lithographically defined gold nanostructures. *Nano Lett.*, 11(3): 1323–1330, 2011. doi: 10.1021/nl104410t.

[22] Nicholas W. Bigelow, Alex Vaschillo, Jon P. Camden, and David J. Masiello. Signatures of fano interferences in the electron energy loss spectroscopy and cathodoluminescence of symmetry-broken nanorod dimers. *ACS Nano*, 7(5):4511–4519, 2013. doi: 10.1021/nn401161n.

[23] Khanikaev Alexander B., Wu Chihhui, and Shvets Gennady. Fano-resonant metamaterials and their applications. *Nanophotonics*, 2:247, 2013. doi: 10.1515/nanoph-2013-0009.

[24] Judy J. Cha, Kristie J. Koski, Kevin C. Y. Huang, Ken Xingze Wang, Weidong Luo, Desheng Kong, Zongfu Yu, Shanhui Fan, Mark L. Brongersma, and Yi Cui. Two-dimensional chalcogenide nanoplates as tunable metamaterials via chemical intercalation. *Nano Lett.*, 13(12):5913–5918, 2013. doi: 10.1021/nl402937g.

[25] Toon Coenen and Albert Polman. Optical properties of single plasmonic holes probed with local electron beam excitation. *ACS Nano*, 8(7):7350–7358, 2014. doi: 10.1021/nn502469r.

[26] Toon Coenen, Ernst Jan R. Vesseur, Albert Polman, and A. Femius Koenderink. Directional emission from plasmonic Yagi–Uda antennas probed by angle-resolved cathodoluminescence spectroscopy. *Nano Lett.*, 11(9):3779–3784, 2011. doi: 10.1021/nl201839g.

[27] Alberto G. Curto, Giorgio Volpe, Tim H. Taminiau, Mark P. Kreuzer, Romain Quidant, and Niek F. van Hulst. Unidirectional emission of a quantum dot coupled to a nanoantenna. *Science*, 329(5994):930–933, 2010. doi: 10.1126/science.1191922.

[28] Jeremy A. Bossard and Douglas H. Werner. Metamaterials with angle selective emissivity in the near-infrared. *Opt. Express*, 21(5):5215–5225, 2013. doi: 10.1364/OE.21.005215.

[29] Clara I. Osorio, Toon Coenen, Benjamin J. M. Brenny, Albert Polman, and A. Femius Koenderink. Angle-resolved cathodoluminescence imaging polarimetry. *ACS Photonics*, 3(1):147–154, 2016. doi: 10.1021/acsphotonics.5b00596.

[30] Anton Hörl, Andreas Trügler, and Ulrich Hohenester. Tomography of particle plasmon fields from electron energy loss spectroscopy. *Phys. Rev. Lett.*, 111:076801, 2013. doi: 10.1103/PhysRevLett.111.076801.

[31] J. Verbeeck, H. Tian, and P. Schattschneider. Production and application of electron vortex beams. *Nature*, 467(7313):301–304, 2010. doi: 10.1038/nature09366.

[32] Wei Cai, Rebecca Sainidou, Jingjun Xu, A Polman, and F Javier García de Abajo. Efficient generation of propagating plasmons by electron beams. *Nano Lett.*, 9(3):1176–1181, 2009. doi: 10.1021/nl803825n.

[33] F. Javier García de Abajo. Multiple excitation of confined graphene plasmons by single free electrons. *ACS Nano*, 7(12):11409–11419, 2013. doi: 10.1021/nn405367e.

[34] F. Javier García de Abajo. Graphene plasmonics: Challenges and opportunities. *ACS Photonics*, 1(3):135–152, 2014. doi: 10.1021/ph400147y.

[35] Lukas Novotny and Niek van Hulst. Antennas for light. *Nat. Photonics*, 5(2):83–90, 2011. doi: 10.1038/nphoton.2010.237.

[36] Toon Coenen, Felipe Bernal Arango, A. Femius Koenderink, and Albert Polman. Directional emission from a single plasmonic scatterer. *Nat. Commun.*, 5:3250, 2014. doi: 10.1038/ncomms4250.

[37] A. I. Denisyuk, Giorgio Adamo, K. F. MacDonald, J. Edgar, M. D. Arnold, Viktor Myroshnychenko, M. J. Ford, F. Javier García de Abajo, and N. I. Zheludev. Transmitting Hertzian optical nanoantenna with free-electron feed. *Nano Lett.*, 10(9):3250–3252, 2010. doi: 10.1021/nl1002813.

[38] G. Adamo, J. Y. Ou, J. K. So, S. D. Jenkins, F. De Angelis, K. F. MacDonald, E. Di Fabrizio, J. Ruostekoski, and N. I. Zheludev. Electron-beam-driven collective-mode metamaterial light source. *Phys. Rev. Lett.*, 109:217401, 2012. doi: 10.1103/PhysRevLett.109.217401.

[39] A. Papakostas, A. Potts, D. M. Bagnall, S. L. Prosvirnin, H. J. Coles, and N. I. Zheludev. Optical manifestations of planar chirality. *Phys. Rev. Lett.*, 90:107404, 2003. doi: 10.1103/PhysRevLett.90.107404.

[40] Dianmin Lin, Pengyu Fan, Erez Hasman, and Mark L. Brongersma. Dielectric gradient metasurface optical elements. *Science*, 345(6194):298–302, 2014. doi: 10.1126/science.1253213.

[41] Uriel Levy, Chia-Ho Tsai, Lin Pang, and Yeshaiahu Fainman. Engineering space-variant inhomogeneous media for polarization control. *Opt. Lett.*, 29(15):1718–1720, 2004. doi: 10.1364/OL.29.001718.

[42] N. Yu, P. Genevet, F. Aieta, M. A. Kats, R. Blanchard, G. Aoust, J. P. Tetienne, Z. Gaburro, and F. Capasso. Flat optics: Controlling wavefronts with optical antenna metasurfaces. *IEEE J. Sel. Top. Quantum Electron.*, 19(3):4700423, 2013. doi: 10.1109/JSTQE.2013.2241399.

[43] Shulin Sun, Qiong He, Shiyi Xiao, Qin Xu, Xin Li, and Lei Zhou. Gradient-index meta-surfaces as a bridge linking propagating waves and surface waves. *Nat. Mater.*, 11:426, 2012. doi: 10.1038/nmat3292.

[44] Nanfang Yu, Patrice Genevet, Mikhail A. Kats, Francesco Aieta, Jean-Philippe Tetienne, Federico Capasso, and Zeno Gaburro. Light propagation with phase discontinuities: generalized laws of reflection and refraction. *Science*, 334(6054):333–337, 2011. doi: 10.1126/science.1210713.

[45] Nanfang Yu, Francesco Aieta, Patrice Genevet, Mikhail A. Kats, Zeno Gaburro, and Federico Capasso. A broadband, background-free quarter-wave plate based on plasmonic metasurfaces. *Nano Lett.*, 12(12):6328–6333, 2012. doi: 10.1021/nl303445u.

[46] Benny Walther, Christian Helgert, Carsten Rockstuhl, Frank Setzpfandt, Falk Eilenberger, Ernst-Bernhard Kley, Falk Lederer, Andreas Tünnermann, and Thomas Pertsch. Spatial and spectral light shaping with metamaterials. *Adv. Mater.*, 24(47):6300–6304, 2012. doi: 10.1002/adma.201202540.

[47] B. H. Fong, J. S. Colburn, J. J. Ottusch, J. L. Visher, and D. F. Sievenpiper. Scalar and tensor holographic artificial impedance surfaces. *IEEE Trans. Antennas Propag.*, 58(10):3212–3221, 2010. doi: 10.1109/TAP.2010.2055812.

[48] Patrice Genevet, Jiao Lin, Mikhail A. Kats, and Federico Capasso. Holographic detection of the orbital angular momentum of light with plasmonic photodiodes. *Nat. Commun.*, 3:1278, 2012. doi: 10.1038/ncomms2293.

[49] J-P Tetienne, R Blanchard, N Yu, P Genevet, M A Kats, J A Fan, T Edamura, S Furuta, M Yamanishi, and F Capasso. Dipolar modeling and experimental demonstration of multi-beam plasmonic collimators. *New J. Phys.*, 13(5):053057, 2011. doi: 10.1088/1367-2630/13/5/053057.

[50] Lingling Huang, Xianzhong Chen, Holger Mühlenbernd, Hao Zhang, Shumei Chen, Benfeng Bai, Qiaofeng Tan, Guofan Jin, Kok-Wai Cheah, Cheng-Wei Qiu, Jensen Li, Thomas Zentgraf, and Shuang Zhang. Three-dimensional optical holography using a plasmonic metasurface. *Nat. Commun.*, 4:2808, 2013. doi: 10.1038/ncomms3808.

[51] Sergei A. Kuznetsov, Mikhail A. Astafev, Miguel Beruete, and Miguel Navarro-Cía. Planar holographic metasurfaces for terahertz focusing. *Sci. Rep.*, 5:7738, 2015. doi: 10.1038/srep07738.

[52] Cuicui Lu, Xiaoyong Hu, Kebin Shi, Qin Hu, Rui Zhu, Hong Yang, and Qihuang Gong. An actively ultrafast tunable giant slow-light effect in ultrathin nonlinear metasurfaces. *Light Sci. Appl.*, 4(6):9, 2015. doi: 10.1038/lsa.2015.75.

[53] Nikolay I. Zheludev and Yuri S. Kivshar. From metamaterials to metadevices. *Nat. Mater.*, 11(11):917–924, 2012. doi: 10.1038/nmat3431.

[54] Matthias Kraft, Yu Luo, S. A. Maier, and J. B. Pendry. Designing plasmonic gratings with transformation optics. *Phys. Rev. X*, 5:031029, 2015. doi: 10.1103/PhysRevX.5.031029.

[55] Nanfang Yu and Federico Capasso. Flat optics with designer metasurfaces. *Nat. Mater.*, 13(2):139–150, 2014. doi: 10.1038/nmat3839.

[56] Arseniy I. Kuznetsov, Andrey E. Miroshnichenko, Mark L. Brongersma, Yuri S. Kivshar, and Boris Luk'yanchuk. Optically resonant dielectric nanostructures. *Science*, 354(6314):846, 2016. doi: 10.1126/science.aag2472.

[57] Jason Valentine, Jensen Li, Thomas Zentgraf, Guy Bartal, and Xiang Zhang. An optical cloak made of dielectrics. *Nat. Mater.*, 8:568, 2009. doi: 10.1038/nmat2461.

[58] Andrey Igorevich Denisyuk. *Cathodoluminescence and phase-change functionality of metallic nanoparticles*. PhD thesis, University of Southampton, 2009.

[59] Behrad Gholipour, Jianfa Zhang, Kevin F. MacDonald, Daniel W. Hewak, and Nikolay I. Zheludev. An all-optical, non-volatile, bidirectional, phase-change meta-switch. *Adv. Mater.*, 25(22):3050–3054, 2013. doi: 10.1002/adma.201300588.

[60] H.-J. Fitting, T. Ziems, Roushdey Salh, M.V. Zamoryanskaya, K.V. Kolesnikova, B. Schmidt, and A. von Czarnowski. Cathodoluminescence of wet, dry, and hydrogen-implanted silica films. *J. Non-Cryst. Solids*, 351(27):2251–2262, 2005. doi: 10.1016/j.jnoncrysol.2005.06.017.

[61] T. Suzuki and N. Yamamoto. Cathodoluminescent spectroscopic imaging of surface plasmon polaritons in a 1-dimensional plasmonic crystal. *Opt. Express*, 17(26): 23664–23671, 2009. doi: 10.1364/OE.17.023664.

[62] Brett Barwick, David J. Flannigan, and Ahmed H. Zewail. Photon-induced near-field electron microscopy. *Nature*, 462(7275):902–906, 2009. doi: 10.1038/nature08662.

[63] P. Kramper, M. Agio, C. M. Soukoulis, A. Birner, F. Müller, R. B. Wehrspohn, U. Gösele, and V. Sandoghdar. Highly directional emission from photonic crystal waveguides of subwavelength width. *Phys. Rev. Lett.*, 92:113903, 2004. doi: 10.1103/PhysRevLett.92.113903.

[64] H. J. Lezec, A. Degiron, E. Devaux, R. A. Linke, L. Martin-Moreno, F. J. Garcia-Vidal, and T. W. Ebbesen. Beaming light from a subwavelength aperture. *Science*, 297(5582):820–822, 2002. doi: 10.1126/science.1071895.

[65] Jean-Jacques Greffet, Remi Carminati, Karl Joulain, Jean-Philippe Mulet, Stephane Mainguy, and Yong Chen. Coherent emission of light by thermal sources. *Nature*, 416(6876):61–64, 2002. doi: 10.1038/416061a.

[66] Nanfang Yu, Jonathan Fan, Qi Jie Wang, Christian Pflugl, Laurent Diehl, Tadataka Edamura, Masamichi Yamanishi, Hirofumi Kan, and Federico Capasso. Small-divergence semiconductor lasers by plasmonic collimation. *Nat. Photonics*, 2(9):564–570, 2008. doi: 10.1038/nphoton.2008.152.

[67] K. G. Lee, X. W. Chen, H. Eghlidi, P. Kukura, R. Lettow, A. Renn, V. Sandoghdar, and S. Gotzinger. A planar dielectric antenna for directional single-photon emission and near-unity collection efficiency. *Nat. Photonics*, 5(3):166–169, 2011. doi: 10.1038/nphoton.2010.312.

[68] K. V. Sreekanth, T. Biaglow, and G. Strangi. Directional spontaneous emission enhancement in hyperbolic metamaterials. *J. Appl. Phys.*, 114(13):134306, 2013. doi: 10.1063/1.4824287.

[69] Michel Bosman, Vicki J Keast, Masashi Watanabe, Abbas I Maaroof, and Michael B Cortie. Mapping surface plasmons at the nanometre scale with an electron beam. *Nanotechnology*, 18(16):165505, 2007. doi: 10.1088/0957-4484/18/16/165505.

[70] R. Sapienza, T. Coenen, J. Renger, M. Kuttge, N. F. van Hulst, and A. Polman. Deep-subwavelength imaging of the modal dispersion of light. *Nat. Mater.*, 11(9): 781–787, 2012. doi: 10.1038/nmat3402.

[71] G. Adamo, K. F. MacDonald, Y. H. Fu, C-M. Wang, D. P. Tsai, F. J. García de Abajo, and N. I. Zheludev. Light well: A tunable free-electron light source on a chip. *Phys. Rev. Lett.*, 103(11):113901, 2009. doi: 10.1103/physrevlett.103.113901.

[72] Dennis Gabor. A new microscopic principle. *Nature*, 161:777–778, 1948. doi: 10.1038/161777a0.

[73] F. J. García de Abajo. Optical excitations in electron microscopy. *Rev. Mod. Phys.*, 82(1):209–275, 2010. doi: 10.1103/revmodphys.82.209.

[74] B. J. M. Brenny, T. Coenen, and A. Polman. Quantifying coherent and incoherent cathodoluminescence in semiconductors and metals. *J. Appl. Phys.*, 115(24): 244307, 2014. doi: 10.1063/1.4885426.

[75] W. Lukosz and R. E. Kunz. Light emission by magnetic and electric dipoles close to a plane interface: I. total radiated power. *J. Opt. Soc. Am.*, 67(12):1607–1615, 1977. doi: 10.1364/JOSA.67.001607.

[76] Peder Meyer Hansen. *The radiation efficiency of a dipole antenna located above an imperfectly conducting ground*. PhD thesis, University of Michigan, 1970.

[77] B. R. Brown and A. W. Lohmann. Computer-generated binary holograms. *IBM J. Res. Dev.*, 13(2):160–168, 1969. doi: 10.1147/rd.132.0160.

[78] Wai-Hon Lee. Binary synthetic holograms. *Appl. Opt.*, 13(7):1677–1682, 1974. doi: 10.1364/AO.13.001677.

[79] Nikolay I. Zheludev A. V. Krasavin, Kevin F. MacDonald. *Nanophotonics with Surface Plasmons Advances in Nano-Optics and Nano-Photonics*, pages 109–139. Elsevier, 2007.

[80] Stephan T. Koev, Amit Agrawal, Henri J. Lezec, and Vladimir A. Aksyuk. An efficient large-area grating coupler for surface plasmon polaritons. *Plasmonics*, 7 (2):269–277, 2012. doi: 10.1007/s11468-011-9303-7.

[81] M. Kuttge, E. J. R. Vesseur, J. Verhoeven, H. J. Lezec, H. A. Atwater, and A. Polman. Loss mechanisms of surface plasmon polaritons on gold probed by cathodoluminescence imaging spectroscopy. *Appl. Phys. Lett.*, 93(11):113110, 2008. doi: 10.1063/1.2987458.

[82] J. F. Nye and M. V. Berry. Dislocations in wave trains. *Proc. Royal Soc. Lond.*, 336(1605):165–190, 1974. doi: 10.1098/rspa.1974.0012.

[83] H. He, M. E. J. Friese, N. R. Heckenberg, and H. Rubinsztein-Dunlop. Direct observation of transfer of angular momentum to absorptive particles from a laser beam with a phase singularity. *Phys. Rev. Lett.*, 75:826–829, 1995. doi: 10.1103/PhysRevLett.75.826.

[84] David G. Grier. A revolution in optical manipulation. *Nature*, 424(6950):810–816, 2003. doi: 10.1038/nature01935.

[85] Victor V. Kotlyar, Henna Elfstrom, Jari Turunen, Anton A. Almazov, Svetlana N. Khonina, and Victor A. Soifer. Generation of phase singularity through diffracting a plane or gaussian beam by a spiral phase plate. *J. Opt. Soc. Am. A*, 22(5):849–861, 2005. doi: 10.1364/JOSAA.22.000849.

[86] S. J. Smith and E. M. Purcell. Visible light from localized surface charges moving across a grating. *Phys. Rev.*, 92:1069, 1953. doi: 10.1103/PhysRev.92.1069.

[87] Gordon Schmidt, Christoph Berger, Peter Veit, Sebastian Metzner, Frank Bertram, Jürgen Bläsing, Armin Dadgar, André Strittmatter, Jürgen Christen, Gordon Callsen, Stefan Kalinowski, and Axel Hoffmann. Direct evidence of single quantum dot emission from GaN islands formed at threading dislocations using nanoscale cathodoluminescence: A source of single photons in the ultraviolet. *Appl. Phys. Lett.*, 106(25):252101, 2015. doi: 10.1063/1.4922919.

[88] Guanhai Li, Brendan P. Clarke, Jin-Kyu So, Kevin F. MacDonald, and Nikolay I. Zheludev. Holographic free-electron light source. *Nat. Commun.*, 7:13705, 2016. doi: 10.1038/ncomms13705.

[89] Dana Dudley, Walter M. Duncan, and John Slaughter. Emerging digital micromirror device (DMD) applications. *Proc. SPIE*, 4985:14–25, 2003. doi: 10.1117/12.480761.

[90] Cuiling Gong and Tim Hogan. CMOS compatible fabrication processes for the digital micromirror device. *IEEE Trans. Electron Devices*, 2(3):27–32, 2014. doi: 10.1109/JEDS.2014.2309129.

[91] C. Sun, N. Fang, D.M. Wu, and X. Zhang. Projection micro-stereolithography using digital micro-mirror dynamic mask. *Sens. Actuators A Phys.*, 121(1):113–120, 2005. doi: 10.1016/j.sna.2004.12.011.

[92] M. Hacker, G. Stobrawa, R. Sauerbrey, T. Buckup, M. Motzkus, M. Wildenhain, and A. Gehner. Micromirror SLM for femtosecond pulse shaping in the ultraviolet. *Appl. Phys. B*, 76(6):711–714, 2003. doi: 10.1007/s00340-003-1180-0.

[93] Seok-Whan Chung and Yong-Kweon Kim. Design and fabrication of 10×10 micro-spatial light modulator array for phase and amplitude modulation. *Sens. Actuators A Phys.*, 78(1):63–70, 1999. doi: 10.1016/S0924-4247(99)00205-8.

[94] William E. Ross, Demetri Psaltis, and Robert H. Anderson. Two-dimensional magneto-optic spatial light modulator for signal processing. *Opt. Eng.*, 22(4): 224485, 1983. doi: 10.1117/12.7973148.

[95] Pablo Cencillo-Abad, Jun-Yu Ou, Eric Plum, João Valente, and Nikolay I Zheludev. Random access actuation of nanowire grid metamaterial. *Nanotechnology*, 27(48):485206, 2016. doi: 10.1088/0957-4484/27/48/485206.

[96] Mikhail Lapine, Ilya V. Shadrivov, David A. Powell, and Yuri S. Kivshar. Magnetoelastic metamaterials. *Nat. Mater.*, 11:30, 2011. doi: 10.1038/nmat3168.

[97] J. Y. Ou, E. Plum, L. Jiang, and N. I. Zheludev. Reconfigurable photonic metamaterials. *Nano Lett.*, 11(5):2142–2144, 2011. doi: 10.1021/nl200791r.

[98] João Valente, Jun-Yu Ou, Eric Plum, Ian J. Youngs, and Nikolay I. Zheludev. A magneto-electro-optical effect in a plasmonic nanowire material. *Nat. Commun.*, 6:7021, 2015. doi: 10.1038/ncomms8021.

[99] Jun-Yu Ou, Eric Plum, Jianfa Zhang, and Nikolay I. Zheludev. An electromechanically reconfigurable plasmonic metamaterial operating in the near-infrared. *Nat. Nanotechnol.*, 8:252, 2013. doi: 10.1038/nnano.2013.25.

[100] Salvatore Savo, David Shrekenhamer, and Willie J. Padilla. Liquid crystal metamaterial absorber spatial light modulator for THz applications. *Adv. Opt. Mater.*, 2(3):275–279, 2014. doi: 10.1002/adom.201300384.

[101] Hua-Kuang Liu, Jeffrey A. Davis, and Roger A. Lilly. Optical-data-processing properties of a liquid-crystal television spatial light modulator. *Opt. Lett.*, 10(12): 635–637, 1985. doi: 10.1364/OL.10.000635.

[102] Arnaud Peigné, Umberto Bortolozzo, Stefania Residori, Stéphanie Molin, Pascale Nouchi, Daniel Dolfi, and Jean-Pierre Huignard. Adaptive holographic interferometer at 1.55μm based on optically addressed spatial light modulator. *Opt. Lett.*, 40(23):5482–5485, 2015. doi: 10.1364/OL.40.005482.

[103] Oleksandr Buchnev, Nina Podoliak, Malgosia Kaczmarek, Nikolay I. Zheludev, and Vassili A. Fedotov. Electrically controlled nanostructured metasurface loaded with liquid crystal: Toward multifunctional photonic switch. *Adv. Opt. Mater.*, 3 (5):674–679, 2015. doi: 10.1002/adom.201400494.

[104] Yoshio Hayasaki, Takashi Sugimoto, Akihiro Takita, and Nobuo Nishida. Variable holographic femtosecond laser processing by use of a spatial light modulator. *Appl. Phys. Lett.*, 87(3):031101, 2005. doi: 10.1063/1.1992668.

[105] Gordon D. Love. Wave-front correction and production of Zernike modes with a liquid-crystal spatial light modulator. *Appl. Opt.*, 36(7):1517–1524, 1997. doi: 10.1364/AO.36.001517.

[106] T. Y. Hsu, Uzi Efron, W. Y. Wu, J. N. Schulman, and I. J. D'Haenens. Multiple quantum well spatial light modulators for optical processing applications. *Opt. Eng.*, 27(5):275372, 1988. doi: 10.1117/12.7976686.

[107] S. Bauerdick, C. Burkhardt, D. P. Kern, and W. Nisch. Addressable field emitter array: A tool for designing field emitters and a multibeam electron source. *J. Vac. Sci. Technol. B*, 22(6):3539–3542, 2004. doi: 10.1116/1.1824050.

[108] Armin Feist, Katharina E. Echternkamp, Jakob Schauss, Sergey V. Yalunin, Sascha Schafer, and Claus Ropers. Quantum coherent optical phase modulation in an ultrafast transmission electron microscope. *Nature*, 521(7551):200–203, 2015. doi: 10.1038/nature14463.

[109] Vasilis Tzoganis and Carsten P. Welsch. A non-invasive beam profile monitor for charged particle beams. *Appl. Phys. Lett.*, 104(20):204104, 2014. doi: 10.1063/1.4879285.

[110] Yuanmu Yang, Wenyi Wang, Parikshit Moitra, Ivan I. Kravchenko, Dayrl P. Briggs, and Jason Valentine. Dielectric meta-reflectarray for broadband linear polarization conversion and optical vortex generation. *Nano Lett.*, 14(3):1394–1399, 2014. doi: 10.1021/nl4044482.

[111] Chihhui Wu, Nihal Arju, Glen Kelp, Jonathan A. Fan, Jason Dominguez, Edward Gonzales, Emanuel Tutuc, Igal Brener, and Gennady Shvets. Spectrally selective chiral silicon metasurfaces based on infrared Fano resonances. *Nat. Commun.*, 5:3892, 2014. doi: 10.1038/ncomms4892.

[112] H. J. Lozykowski, W. M. Jadwisienczak, and I. Brown. Visible cathodoluminescence of GaN doped with Dy, Er, and Tm. *Appl. Phys. Lett.*, 74(8):1129–1131, 1999. doi: 10.1063/1.123465.

[113] X. L. Sun, S. H. Goss, L. J. Brillson, D. C. Look, and R. J. Molnar. Depth-dependent investigation of defects and impurity doping in GaN/sapphire using scanning electron microscopy and cathodoluminescence spectroscopy. *J. Appl. Phys.*, 91(10):6729–6738, 2002. doi: 10.1063/1.1454187.

[114] Maurice Pagel, Vincent Barbin, Philippe Blanc, and Daniel Ohnenstetter. *Cathodoluminescence in Geosciences*. Springer, 2000.

[115] K Thonke, I Tischer, M Hocker, M Schirra, K Fujan, M Wiedenmann, R Schneider, M Frey, and M Feneberg. Nanoscale characterisation of semiconductors by cathodoluminescence. *IOP Conf. Ser.: Mater. Sci. Eng.*, 55(1):012018, 2014. doi: 10.1088/1757-899X/55/1/012018.

[116] Paul R Edwards and Robert W Martin. Cathodoluminescence nanocharacterization of semiconductors. *Semicond. Sci. Technol.*, 26(6):064005, 2011. doi: 10.1088/0268-1242/26/6/064005.

[117] Giuseppe Pezzotti and Andrea Leto. Contribution of spatially and spectrally resolved cathodoluminescence to study crack-tip phenomena in silica glass. *Phys. Rev. Lett.*, 103:175501, 2009. doi: 10.1103/PhysRevLett.103.175501.

[118] Andrey I. Denisyuk, Kevin F. MacDonald, and Nikolay I. Zheludev. Cathodoluminescence readout of high-density nanoparticle phase change memory. In *2008 Conference on Lasers and Electro-Optics and 2008 Conference on Quantum Electronics and Laser Science*, page QThD1. Optical Society of America, 2008. doi: 10.1109/QELS.2008.4553099.

[119] Chuanxiao Xiao, Zhen Li, Harvey Guthrey, John Moseley, Ye Yang, Sarah Wozny, Helio Moutinho, Bobby To, Joseph J. Berry, Brian Gorman, Yanfa Yan, Kai Zhu, and Mowafak Al-Jassim. Mechanisms of electron-beam-induced damage in perovskite thin films revealed by cathodoluminescence spectroscopy. *J. Phys. Chem. C*, 119(48):26904–26911, 2015. doi: 10.1021/acs.jpcc.5b09698.

[120] PM Williams and AD Yoffe. Monochromatic cathodoluminescence image in the scanning electron microscope. *Nature*, 221(5184):952–953, 1969. doi: 10.1038/221952a0.

[121] M de Mets and A Lagasse. An investigation of some organic chemicals as cathodoluminescent dyes using the scanning electron microscope. *J. Microsc.*, 94(2):151–156, 1971. doi: 10.1111/j.1365-2818.1971.tb03698.x.

[122] C. H. Qiu, M. W. Leksono, J. I. Pankove, J. T. Torvik, R. J. Feuerstein, and F. Namavar. Cathodoluminescence study of erbium and oxygen coimplanted gallium nitride thin films on sapphire substrates. *Appl. Phys. Lett.*, 66(5):562–564, 1995. doi: 10.1063/1.114013.

[123] E. Silveira, J. A. Freitas, O. J. Glembocki, G. A. Slack, and L. J. Schowalter. Excitonic structure of bulk AlN from optical reflectivity and cathodoluminescence measurements. *Phys. Rev. B*, 71:041201, 2005. doi: 10.1103/PhysRevB.71.041201.

[124] Zackaria Mahfoud, Arjen T. Dijksman, Clémentine Javaux, Pierre Bassoul, Anne-Laure Baudrion, Jérôme Plain, Benoît Dubertret, and Mathieu Kociak. Cathodoluminescence in a scanning transmission electron microscope: a nanometer-scale counterpart of photoluminescence for the study of II-VI quantum dots. *J. Phys. Chem. Lett.*, 4(23):4090–4094, 2013. doi: 10.1021/jz402233x.

[125] M. Boulou and D. Bois. Cathodoluminescence measurements of the minority–carrier lifetime in semiconductors. *J. Appl. Phys.*, 48(11):4713–4721, 1977. doi: 10.1063/1.323537.

[126] Saman Jahani and Zubin Jacob. All-dielectric metamaterials. *Nat. Nanotechnol.*, 11:23, 2016. doi: 10.1038/nnano.2015.304.

[127] Yiqiao Tang and Adam E. Cohen. Optical chirality and its interaction with matter. *Phys. Rev. Lett.*, 104:163901, 2010. doi: 10.1103/PhysRevLett.104.163901.

[128] Rui Yang, Wenxuan Tang, and Yang Hao. A broadband zone plate lens from transformation optics. *Opt. Express*, 19(13):12348–12355, 2011. doi: 10.1364/OE.19.012348.

[129] Amir Arbabi, Yu Horie, Mahmood Bagheri, and Andrei Faraon. Dielectric metasurfaces for complete control of phase and polarization with subwavelength spatial resolution and high transmission. *Nat. Nanotechnol.*, 10:937, 2015. doi: 10.1038/nnano.2015.186.

[130] David Fattal, Jingjing Li, Zhen Peng, Marco Fiorentino, and Raymond G. Beausoleil. Flat dielectric grating reflectors with focusing abilities. *Nat. Photonics*, 4: 466, 2010. doi: 10.1038/nphoton.2010.116.

[131] Alan Zhan, Shane Colburn, Rahul Trivedi, Taylor K. Fryett, Christopher M. Dodson, and Arka Majumdar. Low-contrast dielectric metasurface optics. *ACS Photonics*, 3(2):209–214, 2016. doi: 10.1021/acsphotonics.5b00660.

[132] Qian Wang, Edward TF Rogers, Behrad Gholipour, Chih-Ming Wang, Guanghui Yuan, Jinghua Teng, and Nikolay I Zheludev. Optically reconfigurable metasurfaces and photonic devices based on phase change materials. *Nat. Photonics*, 10 (1):60, 2016. doi: 10.1038/NPHOTON.2015.247.

[133] Benjamin J. Eggleton, Barry Luther-Davies, and Kathleen Richardson. Chalcogenide photonics. *Nat. Photonics*, 5:141, 2011. doi: 10.1038/nphoton.2011.309.

[134] Vahid G. Ta'eed, Neil J. Baker, Libin Fu, Klaus Finsterbusch, Michael R.E. Lamont, David J. Moss, Hong C. Nguyen, Benjamin J. Eggleton, Duk Yong

Choi, Steven Madden, and Barry Luther-Davies. Ultrafast all-optical chalcogenide glass photonic circuits. *Opt. Express*, 15(15):9205–9221, 2007. doi: 10.1364/OE.15.009205.

[135] A Zakery and S.R Elliott. Optical properties and applications of chalcogenide glasses: a review. *J. Non-Cryst. Solids*, 330(1):1–12, 2003. doi: doi.org/10.1016/j.jnoncrysol.2003.08.064.

[136] Simone Raoux, Wojciech Wełnic, and Daniele Ielmini. Phase change materials and their application to nonvolatile memories. *Chem. Rev.*, 110(1):240–267, 2010. doi: 10.1021/cr900040x.

[137] M. Wuttig, H. Bhaskaran, and T. Taubner. Phase-change materials for non-volatile photonic applications. *Nat. Photonics*, 11:465, 2017. doi: 10.1038/nphoton.2017.126.

[138] Yukio Shibata, Toshiharu Takahashi, Toshinobu Kanai, Kimihiro Ishi, Mikihiko Ikezawa, Juzo Ohkuma, Shuichi Okuda, and Toichi Okada. Diagnostics of an electron beam of a linear accelerator using coherent transition radiation. *Phys. Rev. E*, 50:1479–1484, 1994. doi: 10.1103/PhysRevE.50.1479.

[139] Guo-Qian Liao, Yu-Tong Li, Yi-Hang Zhang, Hao Liu, Xu-Lei Ge, Su Yang, Wen-Qing Wei, Xiao-Hui Yuan, Yan-Qing Deng, Bao-Jun Zhu, Zhe Zhang, Wei-Min Wang, Zheng-Ming Sheng, Li-Ming Chen, Xin Lu, Jing-Long Ma, Xuan Wang, and Jie Zhang. Demonstration of coherent terahertz transition radiation from relativistic laser-solid interactions. *Phys. Rev. Lett.*, 116:205003, 2016. doi: 10.1103/PhysRevLett.116.205003.

[140] D. Yu. Sergeeva, A. A. Tishchenko, and M. N. Strikhanov. UV and X-ray diffraction and transition radiation from charged particles bunches. *Nucl. Instrum. Methods Phys. Res. B*, 309:189–193, 2013. doi: 10.1016/j.nimb.2013.01.075.

[141] Jin-Kyu So, F. Javier García de Abajo, Kevin F. MacDonald, and Nikolay I. Zheludev. Amplification of the evanescent field of free electrons. *ACS Photonics*, 2(9):1236–1240, 2015. doi: 10.1021/acsphotonics.5b00130.

[142] J. R. M. Saavedra, D. Castells-Graells, and F. Javier García de Abajo. Smith-Purcell radiation emission in aperiodic arrays. *Phys. Rev. B*, 94:035418, 2016. doi: 10.1103/PhysRevB.94.035418.

[143] Weihao Liu, Weiwei Li, Zhigang He, and Qika Jia. Theory of the special Smith-Purcell radiation from a rectangular grating. *AIP Adv.*, 5(12):127135, 2015. doi: 10.1063/1.4939538.

[144] Zhang Ping, Zhang Ya-Xin, Zhou Jun, Liu Wei-Hao, Zhong Ren-Bin, and Liu Sheng-Gang. Enhancement of Smith-Purcell radiation with surface-plasmon excitation. *Chin. Phys. B*, 21(10):104102, 2012. doi: 10.1088/1674-1056/21/10/104102.

[145] S. E. Korbly, A. S. Kesar, R. J. Temkin, and J. H. Brownell. Measurement of subpicosecond bunch lengths using coherent Smith-Purcell radiation. *Phys. Rev. Spec. Top. Ac.*, 9(2):022802, 2006. doi: 10.1103/physrevstab.9.022802.

[146] Yu Gong, Alan G. Joly, Dehong Hu, Patrick Z. El-Khoury, and Wayne P. Hess. Ultrafast imaging of surface plasmons propagating on a gold surface. *Nano Lett.*, 15(5):3472–3478, 2015. doi: 10.1021/acs.nanolett.5b00803.

[147] D. A. G. Deacon, L. R. Elias, J. M. J. Madey, G. J. Ramian, H. A. Schwettman, and T. I. Smith. First operation of a free-electron laser. *Phys. Rev. Lett.*, 38: 892–894, 1977. doi: 10.1103/PhysRevLett.38.892.

[148] P. J. M. van der Slot, T. Denis, J. H. H. Lee, M. W. van Dijk, and K. J. Boiler. Photonic free-electron lasers. *IEEE Photonics J.*, 4(2):570–573, 2012. doi: 10.1109/jphot.2012.2190724.

[149] J. Gardelle, P. Modin, and J. T. Donohue. Start current and gain measurements for a Smith-Purcell free-electron laser. *Phys. Rev. Lett.*, 105(22):224801, 2010. doi: 10.1103/physrevlett.105.224801.

[150] G. Kube, H. Backe, H. Euteneuer, A. Grendel, F. Hagenbuck, H. Hartmann, K. H. Kaiser, W. Lauth, H. Schöpe, G. Wagner, T. Walcher, and M. Kretzschmaret. Observation of optical Smith-Purcell radiation at an electron beam energy of 855 MeV. *Phys. Rev. E*, 65(5):056501, 2002. doi: 10.1103/physreve.65.056501.

[151] Akiko Okajima and Tatsunosuke Matsui. Electron-beam induced terahertz radiation from graded metallic grating. *Opt. Express*, 22(14):17490–17496, 2014. doi: 10.1364/OE.22.017490.

[152] Tetsuya Ishikawa, Hideki Aoyagi, Takao Asaka, Yoshihiro Asano, Noriyoshi Azumi, Teruhiko Bizen, Hiroyasu Ego, Kenji Fukami, Toru Fukui, Yukito Furukawa, Shunji Goto, Hirofumi Hanaki, Toru Hara, Teruaki Hasegawa, Takaki Hatsui, Atsushi Higashiya, Toko Hirono, Naoyasu Hosoda, Miho Ishii, Takahiro Inagaki, Yuichi Inubushi, Toshiro Itoga, Yasumasa Joti, Masahiro Kago, Takashi Kameshima, Hiroaki Kimura, Yoichi Kirihara, Akio Kiyomichi, Toshiaki Kobayashi, Chikara Kondo, Togo Kudo, Hirokazu Maesaka, Xavier M. Maréchal, Takemasa Masuda, Shinichi Matsubara, Takahiro Matsumoto, Tomohiro Matsushita, Sakuo Matsui, Mitsuru Nagasono, Nobuteru Nariyama, Haruhiko Ohashi,

Toru Ohata, Takashi Ohshima, Shun Ono, Yuji Otake, Choji Saji, Tatsuyuki Sakurai, Takahiro Sato, Kei Sawada, Takamitsu Seike, Katsutoshi Shirasawa, Takashi Sugimoto, Shinsuke Suzuki, Sunao Takahashi, Hideki Takebe, Kunikazu Takeshita, Kenji Tamasaku, Hitoshi Tanaka, Ryotaro Tanaka, Takashi Tanaka, Tadashi Togashi, Kazuaki Togawa, Atsushi Tokuhisa, Hiromitsu Tomizawa, Kensuke Tono, Shukui Wu, Makina Yabashi, Mitsuhiro Yamaga, Akihiro Yamashita, Kenichi Yanagida, Chao Zhang, Tsumoru Shintake, Hideo Kitamura, and Noritaka Kumagai. A compact X-ray free-electron laser emitting in the sub-ångström region. *Nat. Photonics*, 6:540, 2012. doi: 10.1038/nphoton.2012.141;.

[153] G Toraldo Di Francia. On the theory of some Čerenkovian effects. *Il Nuovo Cimento*, 16(1):61–77, 1960. doi: 10.1007/BF02860231.

[154] P. M. van den Berg and T. H. Tan. Smith-Purcell radiation from a line charge moving parallel to a reflection grating with rectangular profile. *J. Opt. Soc. Am.*, 64(3):325–328, 1974. doi: 10.1364/JOSA.64.000325.

[155] T. Muto, S. Araki, R. Hamatsu, H. Hayano, T. Hirose, P. Karataev, G. Naumenko, A. Potylitsyn, and J. Urakawa. Observation of incoherent diffraction radiation from a single-edge target in the visible-light region. *Phys. Rev. Lett.*, 90(10): 104801, 2003. doi: 10.1103/physrevlett.90.104801.

[156] John Vernon Jelley. *Cherenkov radiation and its applications*. Pergamon, London, 1958.

[157] Stefan Alexander Maier. *Plasmonics: Fundamentals and Applications: Fundamentals and Applications*. Springer, 2007.

[158] Giorgio Adamo. *Free-electron-driven nanoscale light sources: from Hertzian antennas to metamaterials*. PhD thesis, University of Southampton, 2011.

[159] David M. French, Don Shiffler, and Keith Cartwright. Electron beam coupling to a metamaterial structure. *Phys. Plasmas*, 20(8):083116, 2013. doi: 10.1063/1.4817021.

[160] Jin-Kyu So, Jong-Hyo Won, M. A. Sattorov, Seung-Ho Bak, Kyu-Ha Jang, Gun-Sik Park, D. S. Kim, and F. J. Garcia-Vidal. Cerenkov radiation in metallic metamaterials. *Appl. Phys. Lett.*, 97(15):151107, 2010. doi: 10.1063/1.3492846.

[161] Dmitry N. Klochkov, Koryun B. Oganesyan, Edik A. Ayryan, and Nikolay Sh. Izmailian. Generation of induced Smith-Purcell radiation: free-electron laser in open system. *J. Mod. Opt.*, 63(7):653–659, 2016. doi: 10.1080/09500340.2015.1088969.

[162] H.L. Andrews, F. Bakkali Taheri, J. Barros, R. Bartolini, V. Bharadwaj, C. Clarke, N. Delerue, G. Doucas, N. Fuster-Martinez, M. Vieille-Grosjean, and et al. Reconstruction of the time profile of 20.35 GeV, subpicosecond long electron bunches by means of coherent Smith-Purcell radiation. *Phys. Rev. Spec. Top. Ac.*, 17(5): 052802, 2014. doi: 10.1103/physrevstab.17.052802.

[163] Zhaoyun Duan, Chen Guo, Xin Guo, and Min Chen. Double negative-metamaterial based terahertz radiation excited by a sheet beam bunch. *Phys. Plasmas*, 20(9):093301, 2013. doi: 10.1063/1.4820956.

[164] Anirban Bera, Ranjan Kumar Barik, Matlabjon Sattorov, Ohjoon Kwon, Sun-Hong Min, In-Keun Baek, Seontae Kim, Jin-Kyu So, and Gun-Sik Park. Surface-coupling of Cerenkov radiation from a modified metallic metamaterial slab via Brillouin-band folding. *Opt. Express*, 22(3):3039–3044, 2014. doi: 10.1364/OE.22.003039.

[165] I. Kaminer, S. E. Kooi, R. Shiloh, B. Zhen, Y. Shen, J. J. López, R. Remez, S. A. Skirlo, Y. Yang, J. D. Joannopoulos, A. Arie, and M. Soljačić. Spectrally and spatially resolved Smith-Purcell radiation in plasmonic crystals with short-range disorder. *Phys. Rev. X*, 7:011003, 2017. doi: 10.1103/PhysRevX.7.011003.

[166] Weihao Liu and Zhengyuan Xu. Special Smith-Purcell radiation from an open resonator array. *New J. Phys.*, 16(7):073006, 2014. doi: 10.1088/1367-2630/16/7/073006.

[167] G Adamo, KF MacDonald, YH Fu, DP Tsai, FJ García de Abajo, and NI Zheludev. Tuneable electron-beam-driven nanoscale light source. *J. Opt.*, 12(2): 024012, 2010. doi: 10.1088/2040-8978/12/2/024012.

[168] J. S. Uppal, P. K. Gupta, and R. G. Harrison. Aperiodic ruling for the measurement of Gaussian laser beam diameters. *Opt. Lett.*, 14(13):683–685, 1989. doi: 10.1364/OL.14.000683.

[169] Jean-François Lepage and Nathalie McCarthy. Analysis of the diffractional properties of dual-period apodizing gratings: theoretical and experimental results. *Appl. Opt.*, 43(17):3504–3512, 2004. doi: 10.1364/AO.43.003504.

[170] Alastair P. Hibbins, J. Roy Sambles, and Chris R. Lawrence. Excitation of remarkably nondispersive surface plasmons on a nondiffracting, dual-pitch metal grating. *Appl. Phys. Lett.*, 80(13):2410–2412, 2002. doi: 10.1063/1.1465518.

[171] Wenxing Liu, Yunhui Li, Haitao Jiang, Zhenquan Lai, and Hong Chen. Controlling the spectral width in compound waveguide grating structures. *Opt. Lett.*, 38(2): 163–165, 2013. doi: 10.1364/OL.38.000163.

[172] Diana C. Skigin and Ricardo A. Depine. Resonances on metallic compound transmission gratings with subwavelength wires and slits. *Opt. Commun.*, 262(2):270–275, 2006. doi: 10.1016/j.optcom.2006.01.006.

[173] Diana C. Skigin and Ricardo A. Depine. Diffraction by dual-period gratings. *Appl. Opt.*, 46(9):1385–1391, 2007. doi: 10.1364/AO.46.001385.

[174] Wei Ma, Delin Jia, Xiaomei Yu, Yun Feng, and Yuejin Zhao. Reflective gradient metasurfaces for polarization-independent light focusing at normal or oblique incidence. *Appl. Phys. Lett.*, 108(7):071111, 2016. doi: 10.1063/1.4942465.

[175] Francesco Aieta, Mikhail A. Kats, Patrice Genevet, and Federico Capasso. Multiwavelength achromatic metasurfaces by dispersive phase compensation. *Science*, 347(6228):1342–1345, 2015. doi: 10.1126/science.aaa2494.

[176] Sheng Liu, Michael B. Sinclair, Sina Saravi, Gordon A. Keeler, Yuanmu Yang, John Reno, Gregory M. Peake, Frank Setzpfandt, Isabelle Staude, Thomas Pertsch, and Igal Brener. Resonantly enhanced second-harmonic generation using III-V semiconductor all-dielectric metasurfaces. *Nano Lett.*, 16(9):5426–5432, 2016. doi: 10.1021/acs.nanolett.6b01816.

[177] Roei Remez, Niv Shapira, Charles Roques-Carmes, Romain Tirole, Yi Yang, Yossi Lereah, Marin Soljačić, Ido Kaminer, and Ady Arie. Spectral and spatial shaping of Smith-Purcell radiation. *Phys. Rev. A*, 96:061801, 2017. doi: 10.1103/PhysRevA.96.061801.

[178] J. Rodriguez-Viejo, K. F. Jensen, H. Mattoussi, J. Michel, B. O. Dabbousi, and M. G. Bawendi. Cathodoluminescence and photoluminescence of highly luminescent CdSe/ZnS quantum dot composites. *Appl. Phys. Lett.*, 70(16):2132–2134, 1997. doi: 10.1063/1.119043.

[179] A. P. Alivisatos. Semiconductor clusters, nanocrystals, and quantum dots. *Science*, 271(5251):933–937, 1996. doi: 10.1126/science.271.5251.933.

[180] L. H. Robins, L. P. Cook, E. N. Farabaugh, and A. Feldman. Cathodoluminescence of defects in diamond films and particles grown by hot-filament chemical-vapor deposition. *Phys. Rev. B*, 39:13367–13377, 1989. doi: 10.1103/PhysRevB.39.13367.

[181] Tse-Luen Wee, Yan-Kai Tzeng, Chau-Chung Han, Huan-Cheng Chang, Wunshain Fann, Jui-Hung Hsu, Kuan-Ming Chen, and Yueh-Chung Yu. Two-photon excited fluorescence of nitrogen-vacancy centers in proton-irradiated type Ib diamond. *J. Phys. Chem. A*, 111(38):9379–9386, 2007. doi: 10.1021/jp073938o.

[182] Ido Kaminer, Maor Mutzafi, Amir Levy, Gal Harari, Hanan Herzig Sheinfux, Scott Skirlo, Jonathan Nemirovsky, John D. Joannopoulos, Mordechai Segev, and Marin Soljačić. Quantum Čerenkov radiation: Spectral cutoffs and the role of spin and orbital angular momentum. *Phys. Rev. X*, 6:011006, 2016. doi: 10.1103/PhysRevX.6.011006.

[183] J. Cao, Z. Hao, H. Park, C. Tao, D. Kau, and L. Blaszczyk. Femtosecond electron diffraction for direct measurement of ultrafast atomic motions. *Appl. Phys. Lett.*, 83(5):1044–1046, 2003. doi: 10.1063/1.1593831.

[184] Christoph T. Hebeisen, Ralph Ernstorfer, Maher Harb, Thibault Dartigalongue, Robert E. Jordan, and R. J. Dwayne Miller. Femtosecond electron pulse characterization using laser ponderomotive scattering. *Opt. Lett.*, 31(23):3517–3519, 2006. doi: 10.1364/OL.31.003517.

[185] Brock Doiron, Yi Li, Andrei P. Mihai, Lesley F. Cohen, Peter K. Petrov, Neil M. Alford, Rupert F. Oulton, and Stefan A. Maier. Comparison of the ultrafast hot electron dynamics of titanium nitride and gold for plasmonic applications. *Proc. SPIE*, 10346:1034604, 2017. doi: 10.1117/12.2273941.